Model-based fault diagnosis in rotor systems with self-sensing piezoelectric actuators

Am Fachbereich Maschinenbau
an der Technischen Universität Darmstadt
zur
Erlangung des Grades eines Doktor-Ingenieurs (Dr.-Ing.)
genehmigte

Dissertation

vorgelegt von
Ramakrishnan Ambur Sankaranarayanan, M.Sc.
aus Tirunelveli, Indien

Berichterstatter:	Prof. Dr.-Ing. Stephan Rinderknecht
Mitberichterstatter:	Prof. Dr.-Ing. Stefan Seelecke
Tag der Einreichung:	25.10.2016
Tag der mündlichen Prüfung:	15.12.2016

Darmstadt 2017

D 17

ஒதுவது ஒழியேல்.
- ஒளவையார்

Never stop learning.
- Auvaiyar

Acknowledgment

I would like to express my gratitude to Prof. Dr.-Ing. S. Rinderknecht for his guidance with which I could complete my doctoral thesis at Institute for Mechatronic Systems in Mechanical Engineering at Technische Universität Darmstadt. I thank Prof. Dr.-Ing. S. Seelecke (Universität des Saarlandes), for accepting to be the second examiner of my thesis and for his suggestions.

The entire research work was financed by the German Research Foundation (DFG) within their Research Training Group “GRK1344”, with support from Rolls-Royce Deutschland Ltd and Co. KG. I earnestly acknowledge and thank them here.

My sincere word of thanks goes also to all the colleagues of IMS for their help throughout my tenure. I thank Mr. Stefan Heindel, Mr. Fabian Becker and Ms. Xiaonan Zhao for their valuable technical inputs. Apart from scientific advices Mr. Philipp Zech and Mr. Daniel Plöger have also helped me to hone my thesis, for which am very grateful. Special thanks to Mr. Raja Vadamalu for his varied technical advises.

I am indebted to my parents for their support, offer *namaskarams* to Gurus and dedicate this work to the *Divine*.

Ramakrishnan Ambur Sankaranarayanan,
18.01.2017.

Abstract

Machines which are developed today are highly automated due to increased use of mechatronic systems. Fault detection and isolation are important features to ensure their reliable operation. This research work aims to achieve an integrated control and fault detection functionality with minimum number of components.

Piezomaterials can be used both as sensors and actuators due to their inherent coupling between electrical and mechanical properties. In this thesis, piezoelectric actuators which are being researched for active vibration control on flexible rotors, are also used as sensors. These self-sensing actuators reconstruct their mechanical deflection from the measured voltage and current signals. The systems under investigation are a numerical aircraft engine model and its scaled representation in a rotor test bench. Since the actuators are mounted in rotor bearings, their displacement represent the bearing deflection directly.

In this research work, the virtual sensor signals are utilised for model-based fault diagnosis in rotor systems, with focus on unbalances in rotors. Unbalance magnitude and phase were estimated in frequency domain using a parameter estimation method by least squares optimisation. The robustness of the estimates against signal outliers is improved by method of M-estimators. Identifying the fault location is also explored using the hypothesis of localization of faults.

In simulation, models of both systems (aircraft engine and test bench) were used to detect unbalance faults. In the former system, the influence of actuator placements in fault detection ability is examined. The fault detection method is also validated at the real test bench, as a first step. The unbalance detected using the measured virtual sensor signals is compared against results using available physical sensors. They are found to be in good agreement which proves sensing capability of the actuators. This sensor-minimal approach could be favoured in systems with space constraints.

As a further step, unbalances are detected with self-sensing piezoelectric actuators in closed loop with an adaptive algorithm for vibration minimisation. This combined control effort and fault detection as a strategy, is suitable to augment level of automation in a machine.

Kurzfassung

Der Automatisierungsgrad von Maschinen nimmt durch den vermehrten Einsatz mechatronischer Systeme weiter zu. Fehlererkennung und -Isolation sind wichtig, um ihren zuverlässigen Betrieb zu gewährleisten. Diese Forschungsarbeit strebt nach einer integrierten Regelungs- und Fehlererkennungsstrategie mit einer minimalen Anzahl an Komponenten.

Piezomaterialien können durch die physikalische Kopplung zwischen elektrischen und mechanischen Eigenschaften sowohl aktorisch als auch sensorisch eingesetzt werden. In dieser Arbeit werden Piezoaktoren, die hauptsächlich zur aktiven Schwingungsreduktion an flexiblen Rotoren zum Einsatz kommen, gleichzeitig auch als Sensoren verwendet. Diese selbstsensierenden piezoelektrischen Aktoren rekonstruieren ihre mechanischen Auslenkungen durch Messung der elektrischen Spannung und des Stroms. Die untersuchten Systeme sind Modelle eines Flugtriebwerkes und deren skalierte Ausführung im realen Prüfstand. Da die Aktoren am Rotorlager montiert sind, stellen die rekonstruierten Signale die Lagerauslenkung dar.

In dieser Forschungsarbeit werden diese Signale für die modellbasierte Diagnose der Rotoren eingesetzt. Amplitude und Phase der Unwucht konnten im Frequenzbereich mit parametrischen Ansätzen durch Verwendung der Methode der kleinsten Quadrate ermittelt werden. Zudem wurde die Robustheit der Verfahren gegen Ausreißer durch sogenannte M-Estimators verbessert. Die Identifikation der Unwuchtlage wurde mit einer Hypothese über die Fehlerlokalisierung untersucht.

In Simulationen wurde die Unwuchterkennung sowohl am Modell des Prüfstandes als auch an dem eines Flugtriebwerks untersucht. In letztem Fall wurde ein Einfluss verschiedener Aktorpositionen auf die Güte der Fehlererkennung nachgewiesen. Die Anwendbarkeit der untersuchten Methoden wurde auch am realen Prüfstand gezeigt. Die detektierten Unwuchten aus den rekonstruierten Signalen und aus realen Messungen wurden abgeglichen. Sie zeigen eine gute Übereinstimmung, welche die Sensierungsfähigkeit der Aktoren nachweist. Darüber hinaus eignet sich der sensor-minimale Ansatz besonders für Systeme mit Bauraumeinschränkungen.

Weiterhin wurden auch die Unwuchten mittels selbstsensierender Piezoaktoren mit adaptiven Algorithmen für Schwingungsreduktion im geschlossenen

Regelkreis errechnet. Diese kombinierte Regelung und Fehlerdiagnose ist ein weiterer Schritt um den Automatisierungsgrad von Maschinen weiter zu erhöhen.

Table of Contents

Abstract v
Kurzfassung vii

List of Figures xii
List of Tables xv
Acronyms xvii
Nomenclature xviii

1 Introduction **1**

1.1 Motivation 1
1.2 Structure of the thesis 4

2 State of the art and objectives **7**

2.1 Fault diagnosis 7
2.2 Vibration control 11
2.3 Self-sensing of Piezoelectric actuators 13
2.4 Objectives and goals of the thesis 15

3 Rotor systems and their modelling **17**

3.1 Fundamentals of rotordynamics 17
  3.1.1 Equations of motion 17
  3.1.2 Unbalance and its response 18
  3.1.3 Gyroscopy and Campbell diagram 20
3.2 Test bench at Institute for Mechatronic Systems (IMS) 22
3.3 Model of rotor test bench 23
  3.3.1 Modelling approaches 23
  3.3.2 Finite Element (FE) model of rotor test bench 26
  3.3.3 Integrated FE model 27
3.4 Model enhancement with measured data 30
  3.4.1 Transfer function estimation from measured data 30
  3.4.2 Model updating 35
  3.4.3 Complete model of the test bench 37
3.5 Aircraft turbofan engine 37
  3.5.1 Whole Engine Model (WEM) 39
  3.5.2 Piezoelectric actuators in aircraft engines 40

4 Self-sensing piezoelectric actuator 43
4.1 Actuators 43
4.2 Piezoelectric actuators 44
4.2.1 Piezomaterials 44
4.2.2 Fundamentals of piezoelectricity 44
4.3 Signal reconstruction using self-sensing 46
4.3.1 Self-sensing 47
4.3.2 Self-sensing in piezoelectric actuators 47
4.3.3 Identification of actuator permittivity 48
4.3.4 Construct mechanical displacement 52
4.3.5 Validation of virtual sensor signals 52
4.4 Closed loop controller with self-sensing piezoelectric actuator 52
4.4.1 Vibration reduction in a narrow frequency band 54
4.4.2 Vibration reduction at a stationary operating point 55

5 Fault detection in rotor systems 59
5.1 Fault detection in time domain 59
5.2 Fault detection in frequency domain 62
5.2.1 Introduction to parameter estimation method 62
5.2.2 Rotor system in frequency domain 64
5.2.3 Fault detection 65
5.2.4 Relative residual 66
5.3 Fault detection in closed loop 67
5.4 Robust fault detection 68
5.4.1 Theory of M-estimators 69
5.4.2 Recursive method 71

6 Results and discussion 73
6.1 Fault detection in time domain 73
6.2 Fault detection in scaled rotor model in frequency domain 75
6.3 Fault detection using measured signals from test bench 78
6.3.1 Analysis at stationary operating points 78
6.3.2 Comparison of unbalance detection with other available sensors 83
6.3.3 Transient measurements 86
6.3.4 Unbalance detection with simultaneous actuation 88
6.4 Fault diagnosis in aircraft engine model 89
6.4.1 Active bearing in aircraft HP rotor 91

6.4.2 Active internal suspension of aircraft engine 95
6.5 Discussion 99
6.5.1 Observations from fault diagnosis in test bench 99
6.5.2 Observations from fault diagnosis in WEM 100
6.5.3 Final remarks 101

7 Conclusion and Outlook 103

7.1 Summary of the thesis 103
7.2 Inference 104
7.3 Future works 105

Appendices 115

A Positive Position Feedback (PPF) controller 116

B Introduction to FxLMS algorithm 118

C Simulation results from WEM unbalance detection 120

List of Figures

1.1 Mechatronic system 2

2.1 Classification of fault diagnosis methods 8

3.1 Jeffcott rotor with coordinate system 19
3.2 Unbalance response of a Jeffcott rotor 20
3.3 Campbell diagram of rotor test bench at IMS 21
3.4 Schematic of the rotor test bench 22
3.5 Active bearing plane in the rotor test bench 23
3.6 CAD Diagram of rotor test bench 24
3.7 First two modal shapes of rotor test bench at IMS 24
3.8 Summary of modelling approaches 25
3.9 CAD and lumped parameter model of active bearing 28
3.10 Model of active bearing 29
3.11 Coherence from chirp voltage to all sensors 32
3.12 Impulse excitation positions in test bench 32
3.13 Impulse hammer excitation 33
3.14 Coherence plots 34
3.16 Twin spool turbofan 39
3.17 Squeeze film damper 39
3.18 Proposed positions of piezoelectric actuators in aircraft engine . 40
3.19 Arrangement of piezoactuators in High Pressure (HP) bearings . 41
3.20 Configuration of Active Internal Suspension 42

4.1 Functional diagram of a general actuator 43
4.2 Piezoelectric actuators 44
4.3 Axes convention in piezo materials 46
4.4 Functional diagram of a general self-sensing actuator 47
4.5 Sensor construction process of the actuator 48
4.6 FRF of actuators in parallel planes (Actuator to Strain gauge) . . 49
4.7 Hysteresis estimated from piezoelectric actuators 51
4.8 Magnitude response of band-pass filter 51
4.9 Compare displacement signals in time domain 53
4.10 Comparison of Frequency Response Function (FRF) between the voltage and displacement signal 53
4.11 Block diagram of self-sensing in a closed loop 54
4.12 Performance of Positive Position Feedback (PPF) Controller . . . 56
4.13 Performance of Filtered x-Least mean squares (FxLMS) algorithm 58

5.1 Modified equivalent load minimisation method for unbalance detection in time domain 61
5.2 Parameter estimation by output-error method 62
5.3 Fault detection in a closed loop system 67

6.1 Unbalance rings 75
6.2 Relative residuals from simulations with test bench model 77
6.3 Relative deviation in magnitude of strain signals 81
6.4 FRF and Coherence of Impulse in Ring 4 to Strain 82
6.5 Relative residual with measurements from stationary points . . . 83
6.6 Relative residual with transient measurements 87
6.7 Relative residual with simultaneous actuation and sensing 89

6.8 Relative residual plot from quasi-static run in active bearings (Piezos and SFD in series) 93

6.9 Relative residual plot from quasi-static run in active bearings (Piezos and SFD in parallel) 94

6.10 Relative residual plot from quasi-static run in active internal suspension when all four actuators are considered 96

6.11 Relative residual - Active Internal suspension special cases 98

A.1 Block diagram of rotorsystem with PPF 117

B.1 Block diagram of a FxLMS algorithm 118

C.1 Relative residual of unbalance detection at all stages - Active bearing (Piezo,SFD series) 122

C.2 Relative residual of unbalance detection at all stages - Active bearing (Piezo,SFD parallel) 125

C.3 Relative residual of unbalance detection at all stages - Active internal suspension 128

List of Tables

3.1 Matrices in equations of motion 17

3.2 Parameters in active bearing model 28

3.3 Parameters estimated by optimisation algorithm 35

4.1 Variables and Parameters in piezoelectric equation 45

6.1 Unbalance detected from time domain FDI 74

6.2 Detected unbalances from Test bench (simulation) 76

6.3 Unbalance test cases 79

6.4 Unbalance identified from stationary operating points 80

6.5 Comparison of unbalance magnitude identified from different sensors 84

6.6 Comparison of unbalance phase identified from different sensors 85

6.7 Unbalance identified from operating points in transient run . . . 87

6.8 Unbalance identified from simultaneous actuation and sensing . 88

6.9 Detected unbalances from WEM (Active bearing - Piezo and SFD in series) 91

6.10 Detected unbalances from WEM (Active bearing - Piezo and SFD in parallel) 95

6.11 Detected unbalances from WEM (Active internal suspension - All four actuators) 97

6.12 Detected unbalances from WEM using robust estimators (Active internal suspension) 98

C.1 Detected unbalances from WEM (Active bearing - Piezo and SFD in series) - without any outlier 120

C.2 Detected unbalances from WEM (Active bearing - Piezo and SFD in series) - with outliers 121

C.3 Detected unbalances from WEM (Active bearing - Piezo and SFD in series) - with robust estimators 121

C.4 Detected unbalances from WEM (Active bearing - Piezo and SFD in parallel) - without any outlier 123

C.5 Detected unbalances from WEM (Active bearing - Piezo and SFD in parallel) - with outliers 123

C.6 Detected unbalances from WEM (Active bearing - Piezo and SFD in parallel) - with robust estimators 124

C.7 Detected unbalances from WEM (Active internal suspension) - without any outlier 126

C.8 Detected unbalances from WEM (Active internal suspension) - with outliers 126

C.9 Detected unbalances from WEM (Active internal suspension) - with robust estimators 127

Acronyms

CAD	Computer Aided Design.
CMS	Component Mode Synthesis.
DOF	Degrees of freedom.
FDI	Fault detection and Isolation.
FE	Finite Element.
FIR	Finite Impulse Response.
FRF	Frequency Response Function.
FTC	Fault tolerant control.
FxLMS	Filtered x-Least mean squares.
GA	Genetic Algorithm.
HP	High Pressure.
IMS	Institute for mechatronic systems
LMS	Least Mean Squares.
LP	Low Pressure.
LPV	Linear Parameter Variant.
LQG	Linear Quadratic Gaussian.
MIMO	Multi Input Multi Output.
PPF	Positive Position Feedback.
RC	Resonant controller.
RLS	Recursive Least Squares.
SFD	Squeeze Film Damper.
SISO	Single Input Single Output.
SVD	Singular Value Decomposition.
WEM	Whole Engine Model.
WLS	Weighted least squares.

Nomenclature

Alphabetical symbols

A	Cross section area
a	Weighing factor
C	Boolean matrix
C_{xy}	Coherence between signal y and x
d_{sfd}	Damping factor of SFD
$\boldsymbol{d}$	Piezoconstant
$\mathbf{D}$	Damping matrix
$\mathbf{D}$	Electrical flux density
$\mathbf{E}$	Electrical field strength
e	Error
F	Force vector
$F_U(s)$	Force due to actuation voltage
G	Transfer function
$\mathbf{G}$	Gyroscopic matrix
g	Gain of PPF controller
H	Estimated transfer function
I_p	Polar moment of inertia
I_t	Transversal moment of inertia
I	Current in Piezoelectric actuator
i	Imaginary number
$\mathbf{K}$	Stiffness matrix
$\mathbf{K}_{dyn}$	Dynamic Stiffness matrix
k	Time discrete sample
k_d	Time delay
k_{act}	Stiffness of piezo-actuator
l	length
$\mathbf{M}$	Mass matrix
n	Number of stacks of piezoceramic
q	Charge in a piezo material
$\boldsymbol{q}$	Generalized displacement vector
$\mathbf{R}$	Reduced inverted dynamic stiffness matrix
$\mathbf{S}$	Mechanical strain

S_{px}	Cross spectral density from signal p to x
s^E	Elasticity module
s	Laplace operator
T	Transformation matrix
t	Time vector
U	Voltage of Piezoelectric actuator
V	Optimisation function
$\mathbf{W}$	Weighing matrix
X_m	Measured vibrations
$\hat{x}$	Real value of x
x	Displacement vector
$\dot{x}$	Velocity vector
$\ddot{x}$	Acceleration vector
y_p	Particular solution of lateral displacement
z	Measured signal with unbalanced rotor
z_0	Measured reference signal
z_p	Particular solution of lateral displacement
$\mathbf{Z}$	Circulatory matrix

Greek and Latin symbols

α	Proportionality constant
β	Integration constant
γ_y	Integration constant
γ	Forgetting factor
Δl	Extension of piezo material
δ	Residual
δ_r	Relative Residual
δ_z	Relative deviation between measured signals
ϵ	Eccentricity
ε^{σ}	Electrical permittivity
ε^{S}	Electrical permittivity
$\hat{\Theta}$	Parameter vector
κ	Weighing factor
μ	Step size of FxLMS algorithm
ξ_f	Damping in PPF controller
ρ	Optimisation function
σ	Mechanical stress

Φ	Eigen vector matrix
ϕ	Phase of unbalance
Ψ	Data vector
Ω	Rotational speed
ω	Eigen frequency
ω_f	Target frequency

1 Introduction

1.1 Motivation

Rotating machinery comprise a huge class of mechanical structures, which can be sighted in almost every walk of human life. They exist in form of electromechanical machines such as electric motors and generators, turbomachines such as pumps and turbines. In all of them vibration is an inevitable and undesired phenomenon. Vibrations could lead to failure of the machine or in precision equipments affect its operation. They also cause discomfort to the users for example the passengers in a vehicle.

The most common sources of vibration in machinery are related to inertia of moving parts in the machine. According to Newtons law, a force is needed to accelerate the mass which in return is transmitted to the frame of the machine. In a stationary operating point these forces in rotating machinery are periodic and hence periodic displacements are observed as vibration. There are many different techniques practised to minimise vibration related issues due to forced excitation [1].

1. Introduce damping in the system
2. Include a vibration dynamic absorber
3. Tune the natural frequency of the system away from operating range
4. Identify and reduce the excitation source
5. Isolate the source and the receiver

At the outset, there is much research being done to damp the vibrations both by passive and active methods. In passive methods, machine elements with fluids are developed which dissipate the vibration energy, a shock absorber in automobiles is classical example. Active methods might require an additional energy input to damp the vibrations in some cases. One of the examples is a

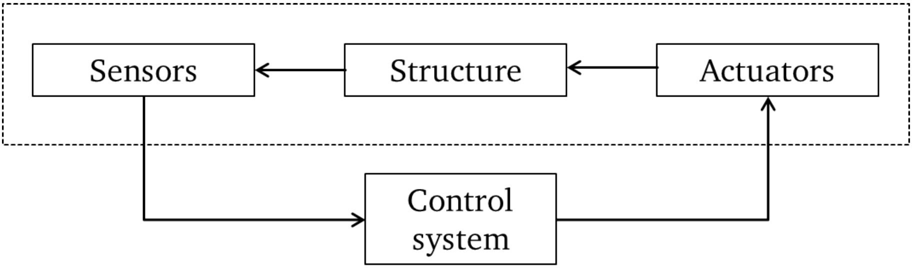

Figure 1.1: Mechatronic system [2]

piezoelectric actuator, which when supplied with an electric voltage reduces the vibrations according to an appropriately designed control algorithm.

Active vibration control methods require a mechatronic system, which is composed of subsystems such as an electronic hardware and a software containing the control algorithm. They are commonly referred together as controllers or a control system. To interact with the real system subjected to vibration, actuators and sensors are needed. Actuators implement a control action as instructed by the controller. Sensors on the other hand supply information about the state of the system to controller. Based on task to be performed, the operating frequency range and physical quantity with which the controller is designed different actuators and sensors are available. This mechatronic system as shown in Fig. 1.1 is a basic block of all automated systems.

Automation of technical processes is going through a progressive increase since many decades. As the design of automated processes gains significance, their supervision becomes unavoidable. System reliability is one of the critical factors when automatic systems are considered. An intuitive automatic supervision is limit or threshold checking of important signals. These simple methods could only raise an alarm quite late. This drove the need towards Fault detection and Isolation (FDI) where with the help of mathematical models, estimation methods sophisticated diagnosis modules could be designed. Fault diagnosis is an essential function for a variety of reasons. A fault not only damages that subsystem, but might also affect other subsystems thereby causing an avalanche-like effect. An early detection of fault saves major breakdown of a machine thereby decreasing the downtime in productivity in commercial applications. Apart from them, fault detection helps to act on the source of vibration, as mentioned in fourth action in the list above. Other indirect benefits are to prevent any degradation of efficiency and to protect users.

As mentioned earlier, sensors inform the controllers regarding the state of the rotor. This means that the information from the sensor is inevitable even to recognise a defective state. To supply information regarding vibrations in a system, either accelerometers, velocity transducers or displacement sensors are included. One among them is selected based on the frequency range of operation and whether they are mounted on bearing block or near shaft. These sensors along with their necessary cabling increase the cost. Also not all locations which are important could be accessible to mount sensors and to lay their cables. This necessitates a sensor minimal system, where the aim is to use as less sensors as possible and to extract sufficient information. A further extension could be to extract information without any dedicated sensors, but with self-sensing.

In this thesis the second approach is attempted using piezoelectric actuators. Because piezo materials have an inherent electro-mechanical coupling, they are used in sensors as well as actuators. This provides an opportunity to use only one component for both actuation and sensing. Hence high voltage piezoelectric actuators which are being developed for vibration control are used also as sensors for fault diagnosis.

The thesis focuses on faults occurring in rotor systems. The main faults which appear in them are

- unbalance,
- misalignment,
- rub or erosion,
- cracks in shafts or blades,
- bearing failures and
- fluid-induced instability

A combination of faults or one leading to another is also possible. Unbalance is the main reason for majority of faults occurring in rotor systems. It occurs in rotors due to manufacturing defects, where additional mass could be present or removed at any particular location along the shaft. During commissioning they have to be compensated by balancing them, by placing counter-balancing masses at pre-decided locations. The rotor is then brought to acceptable vibration limits [3]. Even after balancing, during an operation there could be removal of mass due to erosion of the rotating parts with static parts leading to unbalanced condition. Hence there is a need for condition monitoring at regular intervals.

There are two rotor systems being investigated in this research work for unbalance faults. The first system is an turbofan aircraft engine. In a simulation model of the engine, only the HP rotor is focussed. Piezoelectric actuators are already being investigated for their potential to reduce vibration in them. In the present research work, three actuator positions are analysed for their effectiveness in detecting faults, if sensor signals could be extracted from these actuators.

The second rotor system is a real test bench built in IMS. In this rotor test bench, a shaft downscaled from a Turbopropeller engine rotor is mounted. Piezoelectric actuators were mounted at their bearings with an aim to actively control vibrations [4]. Using self-sensing techniques sensor signals are reconstructed from the actuator signals, thereby using them as self-sensing actuators. The mechanical displacement of actuator reconstructed from its electrical signals represent the bearing deflection. With the help of this deflection unbalance faults are detected. The effectiveness of the fault detection method is examined with model and the real test bench.

1.2 Structure of the thesis

After introduction, the thesis continues with a literature review in Chapter 2. Detailed review regarding the fault diagnosis in rotor systems and different approaches in the past has been presented. A brief summary of active vibration control and effectiveness of piezoelectric actuators in rotor systems is also described. Further, previous attempts of self-sensing in piezoelectric actuators and different approaches are mentioned. Briefly, fault diagnosis in a closed control loop and its basic difference from a fault tolerant control system is explained. Out of the literature survey, the gaps in research are identified and the goals for this thesis are extracted and presented towards the end of the chapter.

In Chapter 3, fundamentals of rotor systems are introduced. The systems which are used for this thesis are presented. The first is a test bench available at the institute. Its mathematical model is also described along with a brief description on grey-box modelling approach using modal testing techniques. The second system is a high pressure rotor system of an aircraft engine. Its finite element model was designed by its manufacturer, in which piezoelectric actuators were included later on at specific locations.

Chapter 4 describes a piezoelectric actuator and introduces self-sensing. The two step procedure of self-sensing for the actuator mounted in the rotor system has been explained. Further the reconstructed virtual signals are compared with real sensor signals. The virtual signals were also used in a closed loop for active vibration control, to prove that the actuator could simultaneously actuate and sense.

Fault detection is first introduced in Chapter 5. Before the process of fault estimation is begun, a mathematical introduction on parameter estimation technique is presented. Further the unbalance detection in time and frequency domain are explained, though only the latter is analysed further in the thesis. Fault location could be possibly determined by a scalar called relative residual. An important take-off from this thesis is the unbalance detection in a closed loop which is explained thereafter. Finally an alternative to the common least squares approach is presented for a robust parameter detection.

The results are presented in Chapter 6. At first the observations from simulations using the aircraft model and test bench model are presented. Later the unbalance detection applied on signals measured from the test bench are shown. The results are then discussed.

Finally Chapter 7 concludes the thesis and presents scope for future work.

2 State of the art and objectives

Literature survey in this chapter is presented in two broad sections. The first section discusses about fault diagnosis in rotor systems. This is then followed by the section on works associated with vibration control, some of them where piezoelectric actuators are used. After that research towards self-sensing in piezoelectric actuators are presented. At the end, challenges faced in this research are derived from them and the objectives of the thesis are presented.

2.1 Fault diagnosis

Fault diagnosis is a combination of three tasks as listed below

1. Fault detection - Determine the occurrence of faults by triggering alarm signals
2. Fault isolation - Classification of faults
3. Fault analysis or identification - Determining the magnitude, type and cause of fault

Faults in engineering systems are diagnosed by a broad spectrum of methods. Their classification has been presented in Fig. 2.1 by [5]. In the first scheme called hardware redundancy, additional identical hardware components are included in the system. Faults are detected if system output differs from the additional hardware's output. Plausibility tests are based on comparison with basic physical laws. The last scheme is to diagnose faults by signal processing methods, which are advantageous only in steady-state processes. They cannot be used for processes which have a wide operating range due to variation of input signals. Because this thesis strives to reduce the components in the system, software redundancy is attempted instead of hardware redundancy. With this scheme, an analytical model of the system is created and compared with the system for any difference in behaviour.

Conventionally model-based fault diagnosis are performed by parity equations or parameter estimation method or their combination. The former is applicable

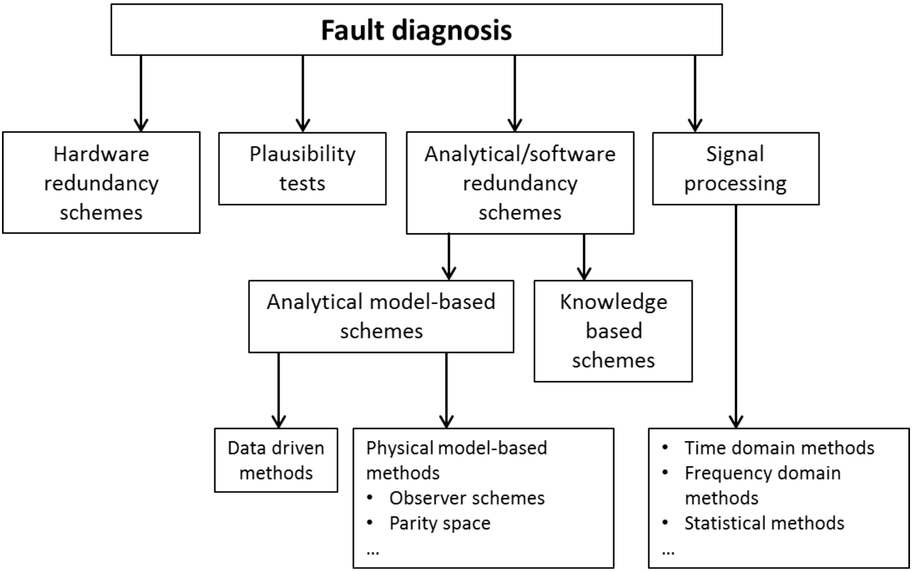

Figure 2.1: Classification of fault diagnosis methods [5]

to additive faults and the latter can also be implemented in case of multiplicative faults. The paper [6] suggests to use the latter method for instationary operation, which is also the case in aircraft engines. To increase robustness against unknown inputs [5] describes the theory of observers. Based on this theory [7] and [8] designed observers to nullify effects of unknown inputs against fault residuals. Fault diagnosis using evolutionary algorithms has been presented in [9].

Fault diagnosis in Rotors

At the outset, fault diagnosis in rotors has been handled in the past by different researchers. Out of all research on condition monitoring, unbalances have been focussed here. A detailed review can be found in [10], in which different faults occuring in rotational systems and techniques used to identify them are presented.

One of the conclusions of the article is that the localisation of faults is still a topic where many researchers have not yet worked. In an experimental approach in [11] optical sensors were used to localise unbalances in induction motors. But it is not practical in large turbines where many rows of blades are mounted. Analytically, Hilbert-Huang transforms were used in [12] to localise faults in a dual disk setup, but still a comprehensive validation for the presented theory is lacking. A data-driven technique has been developed by [13] in which operating deflection shapes have been measured in a machine fault simulator. However it is not suitable for large machines and also due to number of sensors used.

Unbalances in rotor systems are detected by observer based methods in [14] following the work by [15]. Another precursor is use of unknown input observer methods by [16]. In [17], a single transducer was used to balance rotor in different planes.

One of the earlier works to detect unbalance based on a model using least squares approach is by [18] and [19], where the measured signals from the system were compared to a reference model. Here the authors used the modal expansion method, to extrapolate the vibration signals at any other degree of freedom, when sensors could not be positioned at all important locations. This method is one of the first pointers towards a sensor minimal fault detection. However a very accurate model is presumed, and the technique was demonstrated only in a Jeffcott rotor. The theory was extended by [20], where the modal expansion was applied to the signals of the model also, to overcome mathematical problems. Again here the theory was proven only in a single mass rotor where the position of unbalance was known a-priori.

These problems are overcome by the frequency domain parameter estimation method presented by [21] and [22], where multiple faults could be determined. This theory has been used in the present thesis for fault detection. However this method considers faults investigated without any active vibration controller implemented. Hence the theory should be extended to consider actuation forces from piezoelectric actuators.

Modeling efforts for fault detection

In another detailed review paper by [23], a concise list of modeling efforts were given and their use for fault diagnosis is given. It can be seen here that for unbalance fault detection, finite element method for a mathematical model of rotor has been the desired choice by different researchers. To update the speed dependency of models of rotor systems [24] presents a method with which a second parallel model complements the output from a neural network model. Similar procedure was also adopted in [25].

However a complete mathematical model is still not available for condition monitoring in many cases. Hence using different estimation methods, the partially constructed model can be updated. Most of the model updating methods use optimisation routines to minimise the error the between the measured transfer function and model. Here ill-conditioned problems are a challenge, which should be solved by Singular Value Decomposition (SVD) method. An early reference to model updating is given in [26]. One of the conclusion is to match atleast one-third of all the eigen frequencies in the operating range for accurate design purpose. The paper [27] shows a method to calibrate a model in which the rotor is mounted on anisotropic bearings. A recent compilation in [28] describes different direct and iterative methods for finite element model updating.

In all methods for model updating, modal analysis plays an important role. One of earliest references towards it can be found in [29]. More can be understood from [30] where a mathematical background to extract modal model in rotating structures has been presented.

Previous works at IMS

At IMS, there were many research works done on fault diagnosis in rotors. In one of the first works by [31], magnetic bearings were implemented for the model-based fault diagnosis in a centrifugal pump. Here signal- and model-based FDI are performed. The signal based fault detection is based on computing the changes in modal parameters such as eigen frequencies and modal damping when faults occur. In model-based FDI, the transfer function between the model and process are compared to detect faults. The magnetic bearings are used to excite the system with signals of known frequencies to reproduce the transfer function.

In another work by [32], the previous setup of a centrifugal pump with magnetic bearings was investigated further. Here using parameter estimation methods the modal parameters were estimated. However better results were obtained using a transfer function based approach. Using parity equations based approach, two variants to calculate residuals were researched. One uses filters to weigh the residues and another method uses Kalman filters. Different types of errors were diagnosed with the help of a bank of models.

The first implementation of piezoelectric actuators for active bearings was done by [33]. A Jeffcott rotor with a single rotating disc in the centre was mounted between a passive and an active bearing. Sensor and actuator faults were diagnosed with the help of bank of observers. Unbalance as a process fault was diagnosed with the help of force and displacement sensors available at the setup. Another novel method is the implementation of FxLMS algorithm to determine the unbalance parameters using its filter coefficients. In the research work, the idea towards sensor minimality was initiated by implementing an observer instead of force sensors.

The work of [34] describes a method implementing the conventional parity equations as unknown input observers for fault detection. Hereby the gyroscopy, model uncertainties are classified as unknown inputs whose distribution was estimated and their effects nullified during the fault diagnosis procedure.

The different studies mentioned here present the fault diagnosis in rotational systems with active bearings. However the active magnetic bearing or the piezoelectric actuator was used only as an actuating device, but not for simultaneous sensing. Also parameter estimation techniques in frequency domain were not investigated in a rotor with significant gyroscopic terms.

2.2 Vibration control

Out of different measures to reduce vibrations in Section 1.1, isolating the vibration source and the receiver is another important focus of various researchers. This is necessary to interrupt the vibration transmission path, so that other subsystems or the end user remain unaffected. In this section, vibrations arising out of unbalances in rotor systems are focussed and different works to control them are reviewed.

Balancing in aircraft engines

In a turbofan aircraft engine, the fan visible from outside is mounted on the Low Pressure (LP) rotor. So on account of an unbalance after the complete engine assembly, counter-balancing masses can still be screwed to the low-pressure rotor at the nose of the turbo-fan. On the other hand, HP rotor of the engine is not accessible after the complete engine has been built [35]. Hence most part of the balancing should be done during the assembly itself.

The paper [36] describes in detail the vibration health monitoring of the engine both on-board and on-ground. In on-board diagnosis, the analysing software monitors the vibration signals from different transducers and categorises based on the flight maneuver, static or transient conditions and also the ambient atmospheric conditions. The on-ground diagnosis analyses the trend of vibration signals, uses sophisticated methods based on artificial intelligence for diagnosis of vibration events. Out of the different faults which could be diagnosed this way, important are the out-of-balance due to normal deterioration, ice buildup in LP compressor blades, excess out-of-balance due to bird strike or blade loss. Another paper presented by [37], lists the different corrective actions done in an aircraft engine to avoid or mitigate the faults. The unbalance vibrations could be damped by Squeeze Film Damper (SFD), or can be mitigated by adjusting the balancing masses between the compressor and the turbine in the same circumferential position.

However these and the other corrective actions mentioned are to be done either in the design phase or in the test phase, not during the operation of the engine. So either balancing or vibration control measures should be implemented as and when it occurs.

Passive vibration control

In order to damp vibrations, many machine elements were constructed with fluids to dissipate vibrations. One of them is a vibration absorber [38]. Also solid blocks of rubber or fluid mounts or SFD were implemented [39]. The disadvantage of these elements are their limited working range. However later they were extended to semi-active components such as hybrid SFD [40] or adaptive fluid mounts [41].

Their disadvantages are mainly the non-linear behaviour of fluid elements, which poses difficulties in their analysis. Moreover an oil supply is also needed. With a drive towards *More Electric Aircraft* [42], it is desired to replace hydraulic or pneumatic components with electrical components. They ensure an approximately linear and more importantly a predictable functioning.

For a wider operating range and also for better control over system dynamics, active components are researched. One of earliest works include [43] and [44]. Since then active bearings as an effective means for damping rotor vibrations have been exhaustively researched.

The motivation for this research is due to the limitations posed by passive damping elements such as SFD. In a scaled low pressure turbine test setup, [4] investigated the efficacy of a PDT_1 controller and a observer based LQG controller. The latter controller shows a better performance both experimentally and in simulation. [45] extended the work to implement an IFF controller in the test bench taking advantage of the collocated piezoelectric actuator and the force sensors. However the major focus was to implement this controller in model of an aircraft engine considering the dynamics of the engine casing. Another study conducted by [46] on a small rotor system demonstrates and compares feedback controllers such as PDT_1, H_∞ and LQG with a feedforward controller such as FxLMS algorithm. This work has been extended in [47] and [48] to implement a H_∞ algorithm considering a Linear Parameter Variant (LPV) nature of the rotor system.

When it is observed that research in control systems in vibration control of rotating machines covers a wide range starting from simple algorithms, adaptive controllers, observed-based until robust controllers, there is much scope for this field. Recently a novel method was proposed in [49] to eliminate resonances in rotor systems.

2.3 Self-sensing of Piezoelectric actuators

Research in self-sensing of piezoelectric actuators began in 90s when linear reconstruction of capacitance was done. Methods of linear construction were explained by [50] and [51]. In the former a bridge based reconstruction circuit was laid and in the latter Recursive Least Squares (RLS) and Least Mean Squares (LMS) methods were illustrated to calculate electrical capacitance. The linear approximation is valid only until a range of 5% of the maximum operating voltage of the piezo actuator. [52] shows analytically that in case of a high voltage actuator, the linear reconstruction does not suffice, because the error in capacitance identification leads to wrong calculation of location of zeros of the active system under consideration. The linear approach was then extended by different researchers to accommodate hysteresis, creep with the help of non-linear methods, in which operators were constructed to map the effect of one function to another function.

Modelling of piezo materials

In [53], the use of classical Preisach models are suggested and also implemented for a high voltage piezoelectric actuator. The reason being the phenomenological approach of the Preisach method which also enables to calculate the energy loss. The Preisach method was selected out of other methods such as Prandtl-Ishlinskii model, Generalised Maxwell-Slip model, Maxwell-Resistive-Capacitance model. It is also possible to use differential equations, but the computational effort is very high. Two different approaches were given in [54] to analytically model the non-linearities. They are referred as the state variable based and parameter based methods.

In this thesis, instead of analytical models, an experimental method suggested in [55] is implemented.

Fault diagnosis in control loops

An extensive study of fault diagnosis with signal- and model-based methods have been done in [56]. Here residue signals were constructed by model-based methods and characteristic values and boundary checks are suggested for signal-based methods to diagnose faults. It was also suggested to prefer a model-based diagnosis provided the model is accurate enough and simple, because of its ability to distinguish between different fault types and magnitudes. The signal-based methods needs a training phase where different signal characteristics of controlled and manipulated signals should be analysed for different fault types and magnitudes before a diagnosis scheme could be developed. The type of controller plays a lesser role in detecting faults. The developed concepts were validated in two experimental setups. The first one with a pneumatically actuated control valve in a flow control loop. The second experiment on a temperature control loop of a steam-heated heat exchanger.

Difference from FTC

An overview of Fault tolerant control (FTC) was presented in [57]. FTC was motivated by aircraft flight control system designs. The goal was to provide self-repairing capability in order to ensure a safe landing in the event of severe faults in the aircraft [58]. In [59], a detailed review of FTC is given. In [60] a health monitoring system for aero-engine rotor system has been presented.

However there is a need to differentiate the fault diagnosis in control loops from FTC systems. FTC consist of four modules such as fault detection, robust control, a reconfiguration mechanism and supervision, which manages fault decision and selects the control configuration. In case of defect in the system, the fault is not just diagnosed and control action taken, but also the reference model in the software is manipulated accordingly, so that the new configuration is considered as a reference. This enables a further safe operation of the system. Whereas in the case of fault diagnosis in control loops, the reference model is not re-calibrated after detecting and diagnosing the fault. In this thesis also the model will not be changed upon detecting a fault, and therefore is not a work on FTC.

2.4 Objectives and goals of the thesis

There are two rotor systems under investigation. One of them is a rotor test bench available at IMS. The second system is a numerical model of an aircraft engine.

Out of different fault diagnosis approaches, the model-based approach has been selected. As the name suggests, it needs a well-tuned mathematical model of the rotor systems to detect faults. While the aircraft engine model was provided by the manufacturer, the model of rotor test bench needs to be built. Though an existing model developed by [4] was available, it needs to be tuned for inaccuracies.

Some of the unique challenges faced out of the literature presented above are the sensor-minimal diagnosis of faults. Hence self-sensing techniques were researched, to avoid sensors in the system for fault diagnosis. Though self-sensing techniques are implemented for control purposes, their potential towards fault diagnosis has not yet been investigated. An integrated vibration control and fault diagnosis module is a system which has a versatile functionality and more desired in automated systems. Hence apart from extracting sensory signals from an actuator, its ability to detect faults in a closed control loop should also be proven.

The various goals of this thesis can be summarised below and explained in detail in the following chapters.

- Model-based fault diagnosis
    1. Develop fault diagnosis method using parameter estimation method to detect magnitude, phase and location of unbalances.
    2. Extend the method to accommodate actuation input, while considering FDI in closed control loop situation.
- Self-sensing piezoelectric actuators
    1. Reconstruct mechanical displacement from electrical signals of piezoelectric actuators using self-sensing principle.
    2. Implement the mechanism digitally in test bench.
    3. Validate the virtual signals for their sensing ability and simultaneous actuation and sensing capacity.
- Implementation in rotor systems
    1. Examine the potential of different actuator positions in an aircraft engine with respect to fault diagnosis.
    2. Demonstrate and prove the ability of virtual mechanical displacement signals to identify unbalance parameters from measured signals from test bench.

3 Rotor systems and their modelling

Rotordynamics is the study of rotating structures also called as rotors, specially their behaviour in different operating conditions such as resonance. In this work our focus is on fixed rotors, in which a bearing restricts the movement of the rotor to a fixed space. The fixed or non-moving parts in the structure are defined as stators.

3.1 Fundamentals of rotordynamics

3.1.1 Equations of motion

A discretised model of a linear rotor which is axially symmetrical about its spin axis and rotates at a constant angular velocity Ω can be described by the equations of motion as given by Eq. (3.1).

$$\mathbf{M}\ddot{\mathbf{q}}(t)+(\mathbf{D}+\mathbf{G})\,\dot{\mathbf{q}}(t)+(\mathbf{K}+\mathbf{Z})\,\mathbf{q}(t)=\boldsymbol{F}(t) \tag{3.1}$$

The different matrices in Eq. (3.1) are listed in Tab. 3.1. In a generalised spatial coordinate system the vectors $\mathbf{q}, \dot{\mathbf{q}}$ and $\ddot{\mathbf{q}}$ are the displacement, velocity

Table 3.1: Matrices in equations of motion

M	Mass matrix	Symmetric
D	Damping matrix	Symmetric
K	Stiffness matrix	Symmetric
G	Gyroscopic matrix	Skew symmetric
Z	Circulatory matrix	Skew symmetric

and acceleration vectors respectively in time domain. In the generalised system, torsional Degrees of freedom (DOF) and axial displacement (x) can be neglected. So only two dimensional displacement in lateral directions (z,y) and two dimensional rotations (φ_x,φ_y) are considered. The above mentioned vectors has hence four quantities per node. The vector ***F(t)*** is the external force on the system, which in rotordynamics is predominantly the residual unbalance force.

The matrix **Z** is significant in a rotor mounted on hydrodynamic bearings or with seals, where the damping of fluid film surrounding the rotor plays a role. The matrix **G** contains only inertial terms which are associated with gyroscopic moments acting on the rotating parts of a system. If the equation is written in a non-inertial frame, the matrix includes components of Coriolis acceleration. The rotor is not only a point mass, but also has principal moments of inertia.

3.1.2 Unbalance and its response

A simple form of a rotor to understand its basics is a *Jeffcott rotor* depicted in Fig. 3.1. It shows a rotating disc with a massless shaft fixed in rigid bearings on its ends. The axis connecting the centre of rotation is O and the shaft axis is represented by W. The centre of mass of the rotating disc (S) is offset from the point W by a distance (ϵ) called as *eccentricity*. An unbalance is then defined as the product of eccentricity and the offset mass ($m\epsilon$). Phase of the unbalance (ϕ) is denoted by the angular position of the mass with respect to the coordinate frame of reference. When an unbalanced mass at radius equal to the eccentricity rotates at the speed Ω, it causes a centrifugal force $m\epsilon\Omega^2$, which can be represented as given in Eq. (3.2). This centrifugal force at the location of the disc is the same external force ($\mathbf{F}(t)$) in Eq. (3.1). It is assumed at this point that no other external force acts on the rotor system.

$$F(t) = m\epsilon\Omega^2 cos(\Omega t + \phi) \tag{3.2}$$

The natural frequency of the Jeffcott rotor can be given by Eq. (3.3).

$$\omega = \sqrt{\frac{k}{m}} \tag{3.3}$$

The matrix **G** in Eq. (3.1) is significant when polar moment of inertia I_p of a rotating disc is higher than the transversal moment of inertia I_t. The general

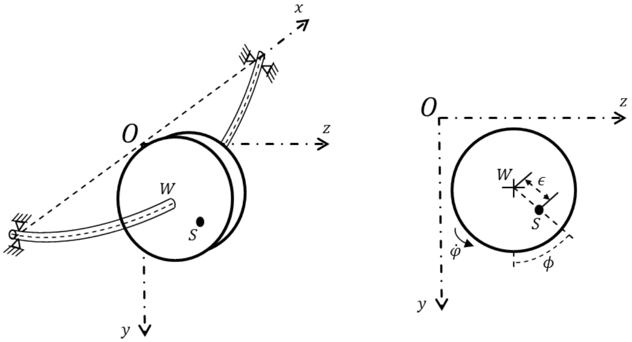

Figure 3.1: Jeffcott rotor with coordinate system

equation of motion (Eq. (3.1)) can be simplified for the Jeffcott rotor into Eq. (3.4), by neglecting matrix **Z** and expanding the other matrices and vectors. The notation $\mathbf{G}_0$ is differentiated from the general notation **G** for gyroscopic matrix, as it does not include the angular velocity information inside it.

$$\mathbf{M}\ddot{q}(t) + (\mathbf{D} + \Omega\mathbf{G}_0)\dot{q}(t) + \mathbf{K}q(t) = \boldsymbol{F}(t) \tag{3.4}$$

At any point in time, the displacement of the rotor at a particular node can be derived by solving the differential equation Eq. (3.4) for the displacement DOF y and z. The solution consists of two parts, the first is called response due to free vibration expressed by homogeneous part. The second part is the response due to forced vibration (ex.unbalance) derived by particular solution. In Eq. (3.5) these two components are expressed. In this equation, γ_y, β are constants of integration, which can be calculated with the help of initial conditions, y_0 and y_p are the amplitudes of the homogeneous and particular solution respectively.

$$y = \underbrace{y_0 cos(\omega t + \gamma_y)}_{\text{Homogeneous solution}} + \underbrace{\epsilon\left(\frac{\omega^2}{\Omega^2 - \omega^2}\right) cos(\Omega t + \beta)}_{\text{Particular solution}} \tag{3.5}$$

$$y_p = \epsilon\left(\frac{\omega^2}{\Omega^2 - \omega^2}\right) \tag{3.6}$$

The response in the other orthogonal direction (z) can also be expressed similarly. It is evident from this equation that the response due to unbalance (particular solution) is a sinusoidal term which depends on the speed of rotation

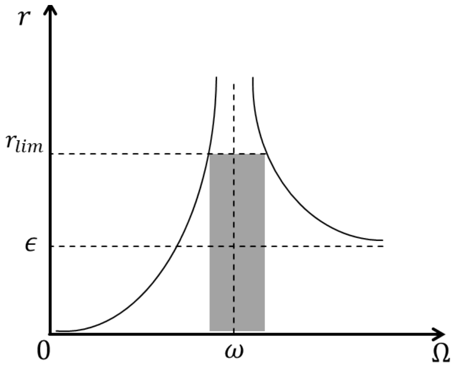

Figure 3.2: Unbalance response of a Jeffcott rotor

and resonance frequency. For further discussions only the magnitude of particular solution caused by unbalances are discussed (Eq. (3.6)). Together with the other lateral displacement (z_p), the radius of the orbit (r) traversed by the point can be expressed by Eq. (3.7).

$$r = \sqrt{{y_p}^2 + {z_p}^2} \tag{3.7}$$

Figure 3.2 shows the magnitude of response to an unbalance force in an operating range. The forces at bearings also follow a similar pattern [61]. The shaded area near the resonance frequency (ω) represents an area where the orbit is large and hence considered as an unstable region. In this discussion of fundamentals, it has been assumed that no damping is present in the system and hence the amplitude near resonance tend to infinity. The acceptable limit to the rotor deflection is defined by the term r_{lim}.

The region to the left of the resonance is called as the *subcritical zone* and its right called as the *supercritical zone*. The entire fault diagnosis in this thesis presented in Chapter 6 was performed in the supercritical zone.

3.1.3 Gyroscopy and Campbell diagram

Due to significance of gyroscopic term which in turn is dependent on rotating speed Ω, the natural frequency of the rotor changes with respect to the speed

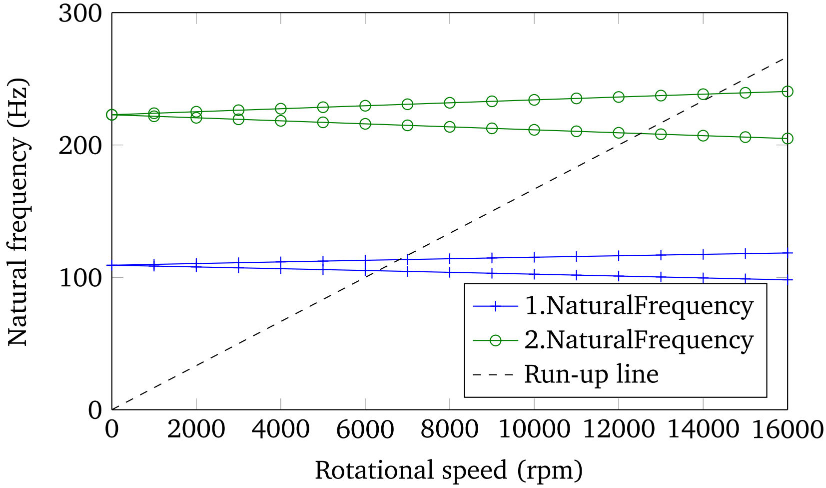

Figure 3.3: Campbell diagram of rotor test bench at IMS

of the rotor. A visual representation of changing natural frequency is shown in a *Campbell diagram*. The Campbell diagram for a test bench at IMS which will be introduced in the next section is plotted in Fig. 3.3. The abscissa denotes the rotational speed and the ordinate represent the natural frequency. A diagonal line in the diagram denotes the speed run-up of the rotor. At standstill ($\Omega = 0$ rpm), the eigen frequencies are 109 Hz and 220 Hz respectively, which are nothing but first two *natural frequencies*. Two lines originate from each of these points, one with a positive and another with a negative slope. The line with a positive slope represent the natural frequencies in forward whirl and the other line represent the backward whirl natural frequencies.
The intersection of these lines to the diagonal line denote the critical speeds of the rotor. If these intersection points are far right to the operating frequency range, the rotor is said to be rigid, otherwise they are called flexible or elastic rotor. From Fig. 3.3 it can be inferred that the rotor to be discussed in the next section is a flexible rotor.

Due to high vibrational amplitudes, the critical speeds of the rotor are avoided in normal operation. This means that the operating point of the rotor should not be in close proximity to the critical speed. In case of an accelerating rotor, this speed should be traversed quickly. Detailed discussions on fundamentals of rotordynamics could be found in [61] and [62].

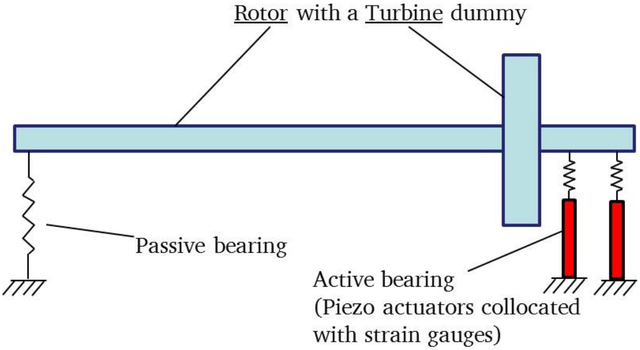

Figure 3.4: Schematic of the rotor test bench

3.2 Test bench at IMS

At IMS, a rotor testbench has been built with active bearings. Its schematic is depicted in Fig. 3.4. The shaft of the rotor is 1.17 m long and 35 mm in diameter. It bears a rotating mass to represent a turbine of a turbo propeller engine. Together with this turbine dummy, the rotor weighs 22.5 kg. At one of the sides a passive ball-bearing has been mounted. The other end of the rotor has an active double bearing assembly containing two parallel planes of ball bearings. There are two piezoelectric actuators mounted perpendicular to each other in each plane at this end. Hence there are four actuators which are named as *2H*, *2V*, *3H* and *3V*. The number represent the plane of bearing and the alphabet if it is horizontally or vertically mounted. The aim of the actuators is to actively control vibrations in the rotor.

The piezoelectric stack actuators have a maximum displacement of 120 μm and a blocking force 14 kN. To avoid any tensile forces the bearing assemblies are prestressed with disc springs. The actuators are operated with an offset voltage of 500 V to ensure that only compressive forces act on them. Hence the actuators always work against a compressive force of 7 kN. In Fig. 3.5, the CAD cross section of the active bearing assembly can be seen.

An asynchronous motor with power 5.1 kW drives the rotor until a maximum rotational speed 17 700 rpm which corresponds to an operating frequency range of almost 0-300 Hz.The rotor is flexible because of two eigen frequencies at 109 Hz and 220 Hz within the operating range.

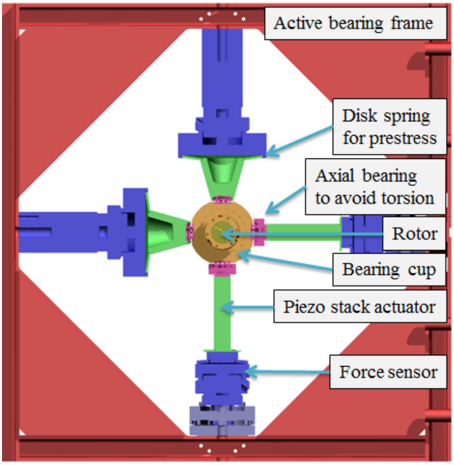

Figure 3.5: Active bearing plane in the rotor test bench

The sensors available in test bench are four eddy current displacement sensors, four load sensors and four strain gauges. The displacement sensors are placed in two planes along the length of the shaft, perpendicular to each other in each plane. These sensors record the displacement in y- and z-directions at these two planes. Four load sensors are collocated to the piezo-actuators at the bearings. The strain gauges are affixed along the length of the piezoelectric actuators, to measure the strain of the actuator and indirectly the displacement of the bearings.

For data acquisition and signal generation a dspace $DS1103$ real time system is used. A CAD diagram of the complete test bench is presented in Fig. 3.6. Figure 3.7 show the mode shapes of the rotor system corresponding to the first two natural frequencies.

3.3 Model of rotor test bench

3.3.1 Modelling approaches

A real system can be modelled with three different approaches which are white-box, black-box and grey-box methods. The grey-box approach has been refined

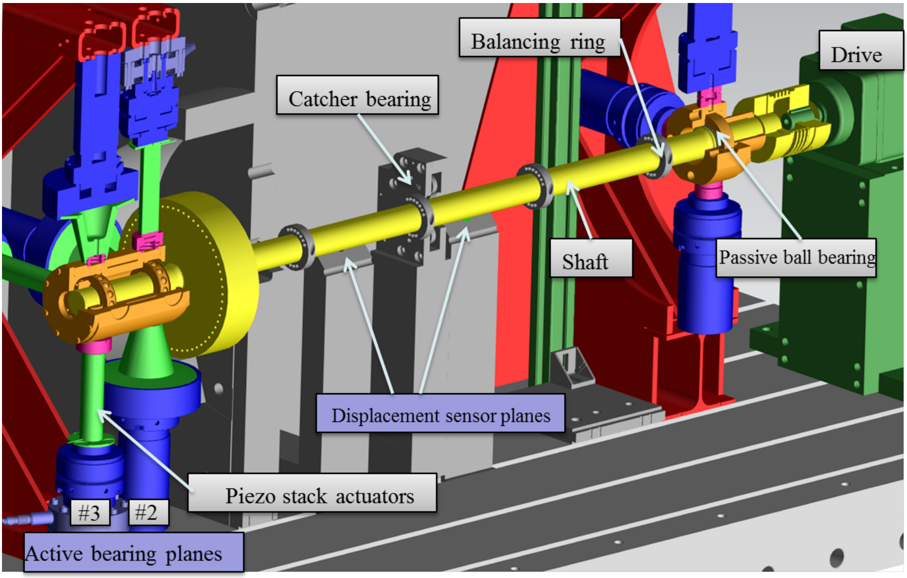

Figure 3.6: CAD Diagram of rotor test bench

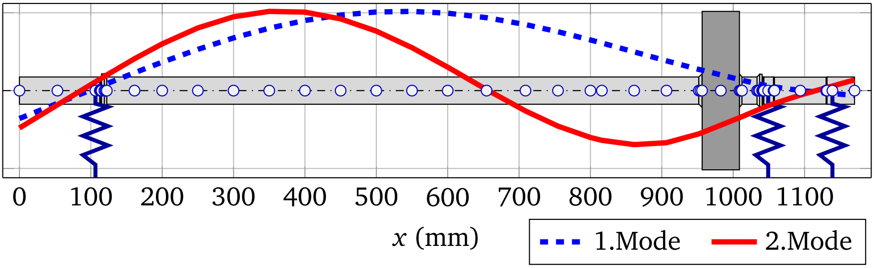

Figure 3.7: First two modal shapes of rotor test bench at IMS

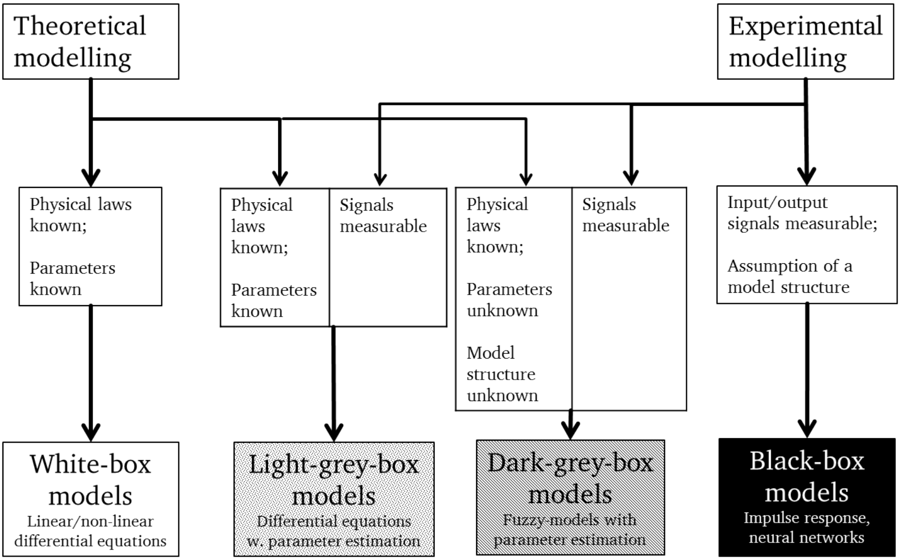

Figure 3.8: Summary of modelling approaches [63]

into light- and dark-grey box in [63]. A summary of these approaches are presented in Fig. 3.8. The individual approaches are explained in following paragraphs.

White-box modelling approach

A White-box modelling refers to an approach in which a mathematical model is created which describes the physics of the real system with sufficient detail. Using the first principles approach, the linear and non-linear phenomena are described by basic laws such as Newton's laws. This modelling approach is always desired because entire model is based on physical understanding. The disadvantage of the method is its complexity. Often real systems consists of complex phenomena such as friction, hysteresis which require complex modelling approaches. Also, there are always certain unknown discrepancies of the model from reality which are difficult to comprehend. If these models should be further exported to an electronic hardware for any control application, the demand on the memory of hardware and the processor speed is huge.

Black-box modelling approach

Another commonly used modelling approach is the black-box method. In this method, a model is constructed without the system knowledge but based on measured data from a real system. The commonly used methods are neural networks, Hammerstein-Wiener models to build a black-box model. The disadvantage of this method is the necessity of large amount of data covering the entire operating range of the machine (e.g. complete frequency range) and also considering all the influencing parameters (e.g. Temperature of the environment).

Inorder to generate a black-box model for the rotor system, it needs to be run at different stationary rotational frequencies with different unbalances, and also by applying a chirp signal at each operating point. Also an intuition to understand the fundamentals of the real rotor system would be lost. This approach is not used to generate a model because of its dependency on huge data.

Grey-box modelling approach

As illustrated in Fig. 3.8, a grey-box approach is a combination of the above two approaches. Here a basic model would be created by physical principles. The real system will be subjected to certain test input signals and output measured. If there are deficiencies in the model with respect to the measured data from the real system, they will be completed by means of methods such as parameter estimation with the help of an optimisation routine. Based on the extent of physical knowledge available, they can be differentiated into a light- or dark-grey-box models. In the present work, a light-grey-box approach is being used. The physical model is explained in Section 3.3.2 and the transfer function estimation from test bench in Section 3.4.1. The grey-box approach and the final transfer functions of the test bench are presented subsequently.

3.3.2 FE model of rotor test bench

In IMS, a toolbox called *rotorbuild* had been developed and implemented in *MATLAB*. This toolbox constructs FE model of rotor systems based on Timoshenko beam theory. The first mathematical model of the test bench has been constructed in [4] from this toolbox. In this work, the rotor shaft and the active bearings are modelled separately and then integrated.

Modelling the rotor

The rotating parts in test bench are a shaft and the turbine dummy. The shaft was discretised into smaller beam elements and their individual mass, stiffness and moment of inertia are calculated based on their material and geometric properties. Similarly the properties of rotating turbine dummy were also calculated. The turbine mass is fitted to shaft by shrink fit. In order to model the fit, an elasticity constant was initially assumed and later estimated by comparing it with modal data.

Active bearing model

As presented in Section 3.2, in the test bench an active double bearing is mounted on one of the sides. The ball bearing in each plane is supported by piezoelectric actuators in perpendicular directions. To avoid any tensile forces in the actuators they are pre-stressed by disc springs. In Fig. 3.9, a vertical cross section of the assembly shows one of the actuator and its prestressed setup, and their respective parameters, which are listed in Tab. 3.2. Fig. 3.10 shows the model of double bearing setup, where the cross section in one of the directions shows both bearing planes. The initial parameters according to [4] were improved by [64] using modal updating methods. Six DOF are depicted in this figure. Considering the other perpendicular place, totally there are 12 DOF in the active bearing model. This model has been used further in this research work.

3.3.3 Integrated FE model

The complete model including the rotor and bearings consist of 57 finite element nodes. With four DOF per node, there are totally 228 degrees of freedom. The mass and stiffness of most of the nodes are calculated from their material properties and geometric data. A proportional damping has been assumed in this model as given in Eq. (3.8). The proportional factors are identified by

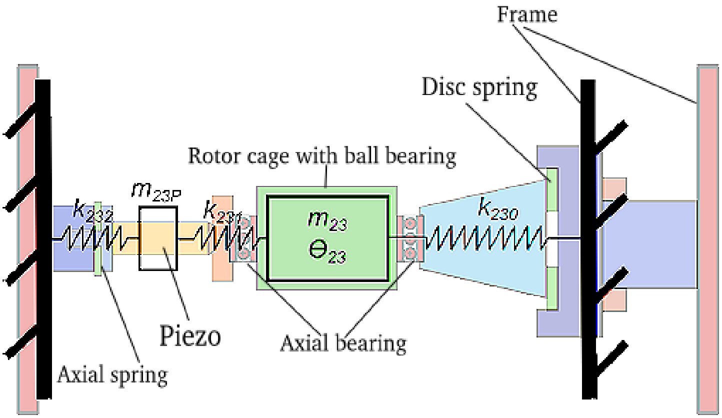

Figure 3.9: CAD and lumped parameter model of active bearing [64]

Table 3.2: Parameters in active bearing model

k_L	Stiffness of ball bearing
k_{230}	Stiffness of disc spring
k_{231}	Stiffness of piezo actuator
k_{232}	Stiffness of axial bearing
m_{23P}	Mass of piezo actuator
m_{23}	Mass of bearing cage
Θ_{23P}	Moment of inertia of bearing cage
q_{23P1}	Displacement of piezo actuator
q_{23}	Displacement of bearing cage
φ_{23}	Rot.displacement of bearing cage
q_{R2}	Displacement of ball bearing

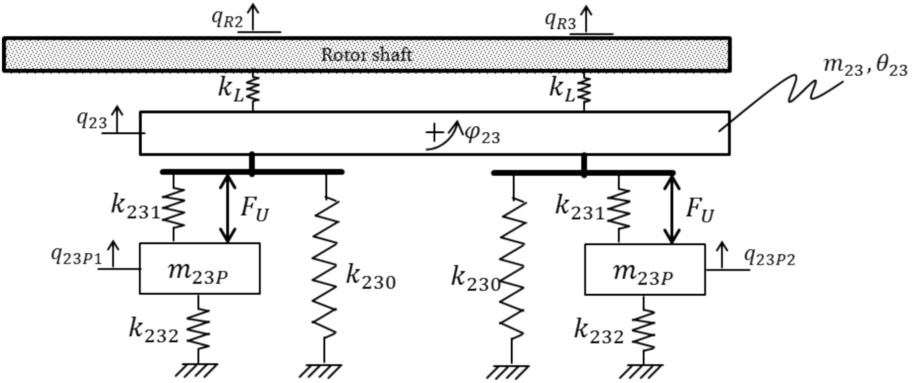

Figure 3.10: Model of active bearing

modal testing. Gyroscopic matrices are assembled with the help of the moments of inertia of the individual finite element nodes.

$$\mathbf{D} = \alpha \mathbf{M} + \beta \mathbf{K} \tag{3.8}$$

The external force to the system is contributed by two sources. One is the excitation by the piezoelectric actuators based on the voltage applied to them. The force due to a stack piezoactuator for an applied voltage U can be defined as given in Eq. (3.9). Here the force F_U, is assumed to be linearly dependent on the voltage, though it is valid only within 40% of the operating voltage range.

$$F_U = nk_{act}d_{33}U \tag{3.9}$$

The second external force is due to unbalances in the system, assuming to be the only fault acting on the system. Their definition and equations are explained in Sections 3.1 and 5.2.3. The complete equation of motion of the rotor bench model has been depicted in Eq. (3.10).

$$\mathbf{M}\ddot{q}(t) + (\mathbf{D} + \Omega \mathbf{G}_0)\dot{q}(t) + \mathbf{K}q(t) = F(t) + F_U(t) \tag{3.10}$$

Equation (3.11) shows how the individual matrices of the rotor model and the bearing model are combined together to form Eq. (3.10). In this equation, the suffixes R and B refer to the matrices of rotor and bearing models respectively.

Matrix K_c refers to the matrix containing stiffness values at the DOF where the rotor and bearing are coupled.

$$\begin{bmatrix} M_R & \mathbf{0} \\ \mathbf{0} & M_B \end{bmatrix}\ddot{q}(t)+\left[D+\Omega\begin{pmatrix} G_R & \mathbf{0} \\ \mathbf{0} & \mathbf{0} \end{pmatrix}\right]\dot{q}(t)+\begin{bmatrix} K_R & K_c \\ K_c^T & K_B \end{bmatrix}q(t)=F(t)+F_U(t) \tag{3.11}$$

This model can be expressed in a state space representation as given in Eq. (3.12).

$$\begin{bmatrix} \dot{q} \\ \ddot{q} \end{bmatrix}=\begin{bmatrix} 0 & I \\ -\mathbf{M}^{-1}\mathbf{K} & -\mathbf{M}^{-1}(\mathbf{D}+\Omega\mathbf{G}_0) \end{bmatrix}\begin{bmatrix} q \\ \dot{q} \end{bmatrix}+\begin{bmatrix} 0 \\ \mathbf{M}^{-1} \end{bmatrix}F+\begin{bmatrix} 0 \\ \mathbf{M}^{-1} \end{bmatrix}F_U$$

$$q=[I\ 0]\begin{bmatrix} q \\ \dot{q} \end{bmatrix} \tag{3.12}$$

3.4 Model enhancement with measured data

The basic structure of the rotor system which was created in [4], needs to be corrected for its accuracy at different frequency positions and also for correct natural frequencies. The model has then been constantly improved for better accuracy in different works such as [65], [66] and in [64]. The transfer functions from measured data are compared to those generated from mathematical model. The differences between them was minimised by different grey-box modelling approaches.

In Section 3.4.1, method to estimate transfer function from measured signals is explained along with the description about the measurements done in the test bench. The model enhancement procedure is explained subsequently in Section 3.4.2. Finally the complete model is presented in Section 3.4.3.

3.4.1 Transfer function estimation from measured data

Estimation

The procedure to estimate the transfer function between any two measured signals according to [67] has been described below in Eq. (3.13)-(3.17). Here the vector S_{xx} refer to the spectral power density of signal x. The spectral density between the signals p and x are referred as cross-spectral density S_{px}.

$$H_4(\Omega) = [1 - \kappa(\Omega)] H_1(\Omega) + \kappa(\Omega) H_2(\Omega) \tag{3.13}$$

$$\kappa(\Omega) = \frac{H_3(\Omega)}{max_{\Omega} \{|H_3(\Omega)|\}} \tag{3.14}$$

$$H_1(\Omega) = \frac{S_{px}(\Omega)}{S_{pp}(\Omega)} \tag{3.15}$$

$$H_2(\Omega) = \frac{S_{xx}(\Omega)}{S_{xp}(\Omega)} \tag{3.16}$$

$$H_3(\Omega) = \frac{1}{2} (H_1(\Omega) + H_2(\Omega)) \tag{3.17}$$

With the help of the variable C_{xy} in Eq. (3.18), the coherence between the signals x and y can be measured.

$$C_{xy}(\Omega) = \frac{\left|S_{xy}(\Omega)\right|^2}{S_{xx}(\Omega) S_{yy}(\Omega)} \tag{3.18}$$

The coherence is a vector of values in range $[0,\ 1]$ and indicate the usefulness of the measurement. The coherence between the two signals at a frequency is maximum (1) if the frequency component of output and input signals are very well seen. A poor coherence (0) indicates that the amplitude of that particular frequency component comes from a different source other than the considered input signal. In our analysis, the impulse excitation measurements which have a poor coherence are discarded.

Measurements

In [65] and [66], the test bench was excited with a chirp voltage signal from the piezoelectric actuator. The signal with a amplitude of 100 V was applied within a timeframe 20 s where the frequency was linearly increased from 0.1-600 Hz. The responses were measured at different sensors and the corresponding transfer functions were constructed. The coherence plots are shown in Fig. 3.11 which shows the good quality of measurements, and hence can be used for model updating. The model updating was performed using Genetic Algorithm (GA).

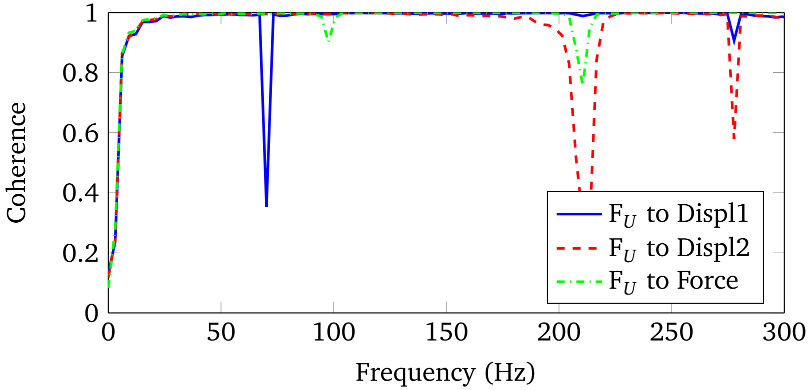

Figure 3.11: Coherence from chirp voltage to all sensors

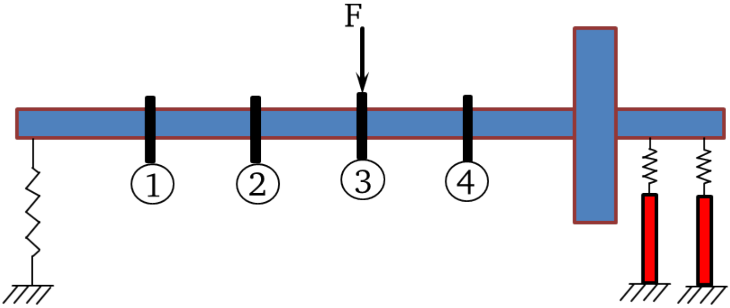

Figure 3.12: Impulse excitation positions in test bench

However the chirp measurement does not represent the actual vibration transmission path from unbalances in rotor to different sensors. So this work was then extended in [64] where instead of chirp excitation, impulse excitation using a modal hammer was applied. The selected positions are the unbalance rings on rotor shaft so that they represent the force transmission due to unbalance masses. The responses were measured at all available sensors, namely the displacement proximity sensors, force sensors and strain gauges. The schematic in Fig. 3.12 shows all the unbalance rings and one of the impulse excitation position as an example.

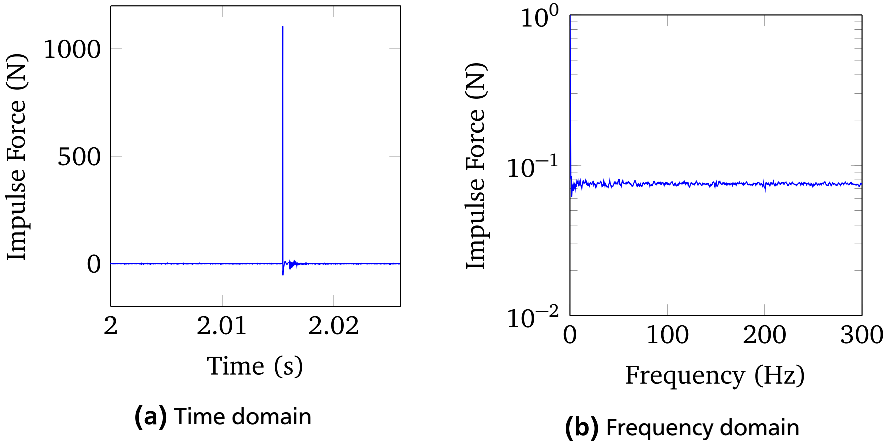

(a) Time domain

(b) Frequency domain

Figure 3.13: Impulse hammer excitation

The plot of the impulse excitation in time and frequency domain can be seen in Fig. 3.13a and 3.13b respectively. From Fig. 3.13, it can be seen that all the frequencies in the operation range are excited with the same amplitude.

The coherence between the different excitations and sensors are shown in Fig. 3.14. It is natural for a hammer test that the coherence in frequency regions away from resonances to be minimum. The reason is due to the low signal-to-noise ratio achieved in impulse hammer excitations compared to chirp excitations [67]. In the first plot Fig. 3.14a, the coherences between the impulse force at unbalance ring 3 and different sensors are shown. It can be seen that the coherence is better for *Sensor-Displ2*, which is the displacement sensor closer to the ring. Also the strain gauge shows a better coherence compared to force sensor at bearings. Hence it can be inferred that the strain gauge is suitable for fault detection. In Fig. 3.14b, the coherence between excitations at different unbalance rings to the strain gauge is shown. As expected, the excitation closer to the bearing (*Ring 4*) shows a better coherence compared to other positions. A drop in coherence values near the frequency range 170 Hz is due to the position of an anti-resonance at the region.

For model updating procedure, the measurements from chirp excitations are used. Because of their better coherence values. The data from hammer excitation was used for validation purposes.

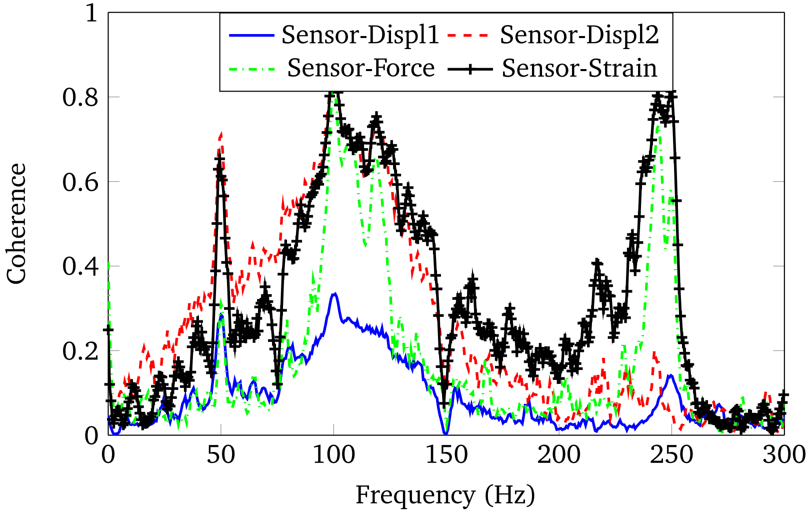

(a) Impulse force at balancing ring3 to different sensors

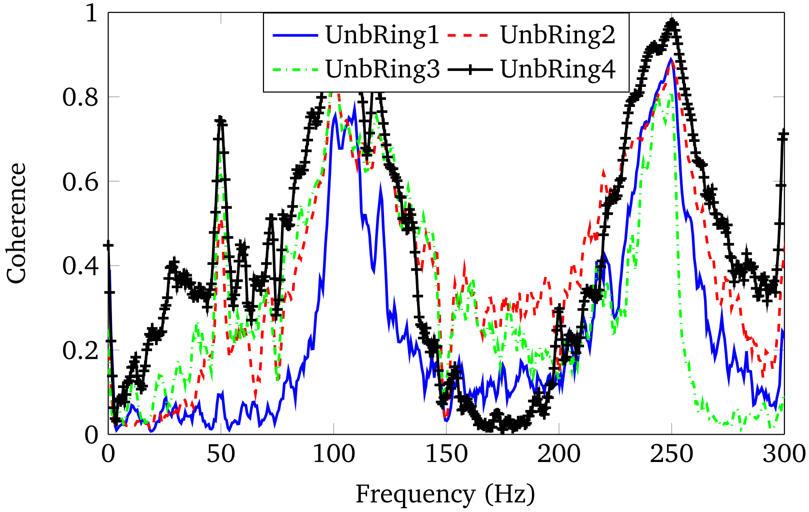

(b) Impulse force at different positions to strain

Figure 3.14: Coherence plots

Table 3.3: Parameters estimated by optimisation algorithm

Number	Parameter
1	Mass of the turbine dummy
2	Moment of inertia of the turbine dummy
3	Mass of the bearing block
4	Moment of inertia of the bearing block
5	Equivalent mass of the piezo stack actuator
6	Proportional constant for Mass Matrix
7	Proportional constant for stiffness matrix
8	Stiffness of ball bearing
9	Stiffness of passive bearing
10	Stiffness of piezo stack actuator
11	Outer stiffness at the active bearing
12	Elasticity module of shaft

3.4.2 Model updating

In a grey-box modelling approach, a set of parameters are identified which needs to be tuned. The tuning is performed by an optimisation algorithm which minimises an objective function by varying the set of parameters subject to certain bounds and constraints. The parameters which are selected based on sensitivity analysis are listed in Tab. 3.3. The developed objective function is described in the following section, after which the algorithm used for optimisation is described.

Optimisation routine

Equation (3.19) defines the objective function to be minimised. It contains two terms weighed by a scalar a. The two terms are described in Eq. (3.20) and (3.21) respectively. The first term V_H defines the deviation of the transfer function of the model with that of the measurement data. The operator $\circ$ refers to a Hadamard-product, which is a quadratic operator. Equation (3.20) considers both the amplitude and phase deviation and shows three different weighting factors. The factors w_o and w_i are the weights for the individual output and input signals respectively. The frequency based weighing factor W_f is derived from coherence C as defined in Eq. (3.22). In this equation, the matrix S is a monotonically increasing weighing factor to avoid low weightage to the high frequency components.

$$V = aV_H + (1-a)V_f \tag{3.19}$$

$$V_H = w_o^T \left(\sum_{i=1}^{k} \sqrt{\left(H_e^i - H_a^i\right) \circ \left(H_e^i - H_a^i\right)} \circ W_f^i \right) w_i \tag{3.20}$$

$$V_f = \frac{1}{2} \sum_{i=1}^{k_{eigen}} \left(\left| \omega_{m,x}^i - \omega_{s,x}^i \right| \right) + \frac{1}{2} \sum_{i=1}^{k_{eigen}} \left(\left| \omega_{m,y}^i - \omega_{s,y}^i \right| \right) \tag{3.21}$$

$$W_f = \frac{H_e}{max\left(H_e\right)} \circ C \circ (S \circ S) \tag{3.22}$$

In Eq. (3.21) the term V_f defines the deviation of the eigenfrequencies between the model and the transfer function in both x- and y-directions.

Genetic Algorithm (GA)

In this thesis, GA is used for achieving an optimal set of parameters. It belongs to a class called *evolutionary algorithm*, inspired from biological systems. Its aim is to achieve an optimum population of individuals by 'developing' an initial population. An individual is a vector of physical parameters. Developing a population means mutation and recombination of individuals to form a new population.

The genetic algorithm begins with an initial population of n individuals, which in our case of a rotor system is listed in Tab. 3.3. In the initial population each parameter is initialised with a value. The initial population (also called the first generation) is evaluated as a first step and the objective function (Eq. (3.19)) calculated. In each step, the parameters are varied and objective is calculated again.

The algorithm proceeds until the minimum of the objective is reached after a defined number of generations or in other words within a defined number of iterations. Because the objective function minimises the error between the transfer functions of model and measurement, its minimum correspond to the optimal values of parameters with which the model matches the measurement.

3.4.3 Complete model of the test bench

The result of the model updating can be seen from FRF plot in Fig. 3.15a and Fig. 3.15b. The initial model before update has also been compared to show the effectiveness of the model updating procedure. In Fig. 3.15a the FRF identified from the model was compared to identified transfer function obtained by chirp excitation of the structure. (FRF of piezoelectric actuator voltage to the force sensor collocated to it). For the sake of comparison, FRF identified from impulse excitations are plotted against the model in Fig. 3.15b. It can be seen that in both magnitude and phase, the model is able to follow the identified FRF closely. Also the resonance frequencies are located very precisely. A good approximation to the real behaviour can be seen.

3.5 Aircraft turbofan engine

The aircraft engine which is being diagnosed for faults is a twin-spool engine used for business jets, a picture of which is presented in Fig. 3.16a. In today's date, jet propulsion is often linked with gas turbine engine. A simple description of mechanical construction of the gas turbine engine is that, it consists of two coaxial rotating shafts with compressor and turbine stages, and stationary combustion chambers between them. The axial flow compressors with multiple stages are assembled in two rotors, the LP and HP shafts, where the air is compressed gradually at each stage. A stage consists of a row of rotating blades followed by a row of stator vanes, which vary the air flow directions depending on the operating point of the compressor. Each compressor rotor is driven by its own turbine. In Fig. 3.16b, the schematic of the twin spool jet engine is shown, where the LP and HP rotor have their own compressor and turbine stages.

The construction of the compressor centres around the rotor assembly and casings. The rotor shafts are supported in rolling element bearings on either side. The LP compressor is supported by one more bearing at the front, as a safety aspect against bird-hit.

The balancing of a compressor rotor is an extremely important operation in its manufacture. Because of the high rotational speeds and the mass of the rotating components high unbalance forces are resulted. These forces would affect the bearings and engine operation. To minimise the effect of dynamic

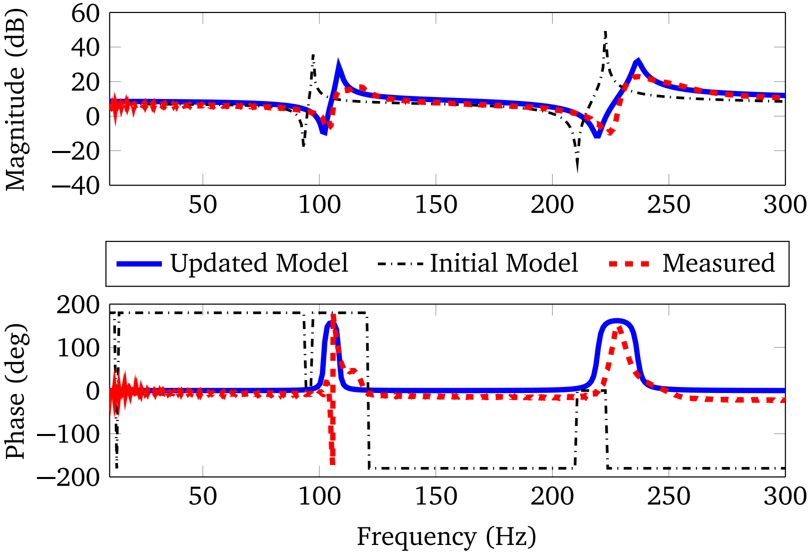

(a) FRF of Chirp excitation of Piezo to force sensor

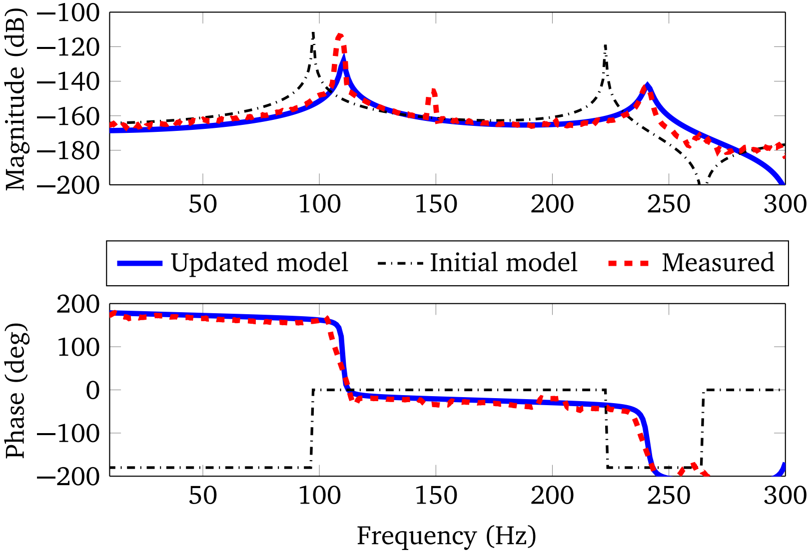

(b) FRF of Impact force in unbalance ring 3 to strain

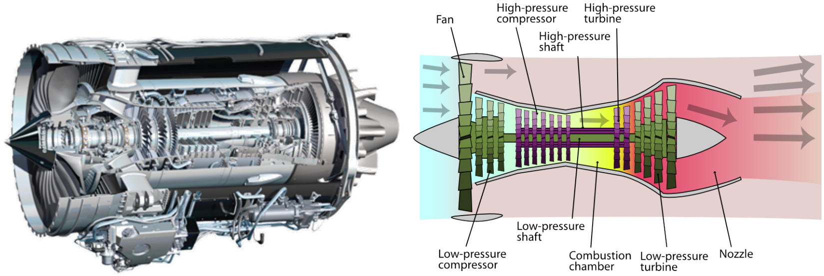

(a) Aircraft turbofan

(b) Schematic of twin spool turbofan [68]

Figure 3.16: Twin spool turbofan

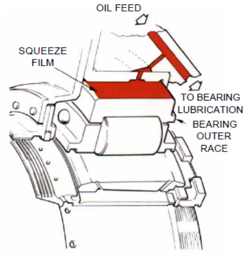

Figure 3.17: Squeeze film damper [69]

loads transmitted from the rotating assemblies to the bearing housings, a SFD around the bearing is used. In Fig. 3.17, a SFD around a bearing is depicted. In these machine elements, the small clearance between the outer race of the bearing and housing is filled with oil. The oil film dampens the radial motion of the rotating assembly and the dynamic loads transmitted to the bearing housing thus reducing the vibration level of the engine and the possibility of damage by fatigue.

3.5.1 Whole Engine Model (WEM)

In the Whole Engine Model (WEM), the complete engine of the aircraft has been modelled by the manufacturers according to finite element theory. Each finite element node has been assigned six DOF, except at the bearings. The

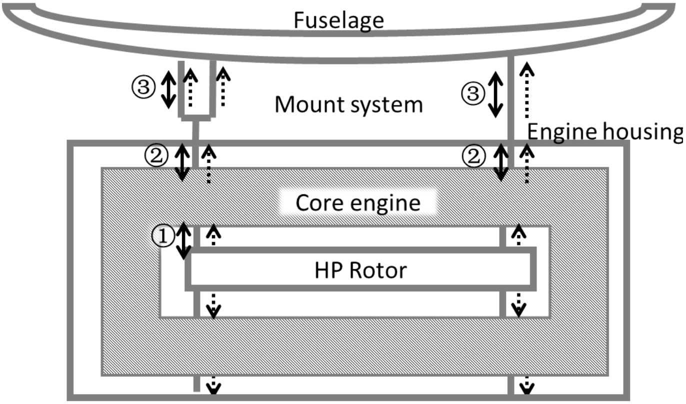

Figure 3.18: Proposed positions of piezoelectric actuators in aircraft engine [71]

six DOF are the three translational degrees of freedom and three rotational degrees of freedom. The model has been reduced according to Component Mode Synthesis (CMS) in [70] and the final model contains 96 nodes and 1881 DOF.

The rotating components include the high-pressure and low-pressure shafts, along with their compressor and turbine stages. The stationary parts include the bearings with SFD, casing and supporting linkages. For further analysis only the HP rotor, the compressor and turbine stages mounted on it, and the corresponding supporting structures are considered. In the HP rotor, ten stages of compressors and two turbine stages are present.

3.5.2 Piezoelectric actuators in aircraft engines

In order to investigate an active vibration control strategy, piezoelectric actuators are included in the WEM, and modelled as elastic springs. In Fig. 3.18 their positions are numbered in schematic of a HP rotor and surroundings. Three different locations for the actuators as mentioned in following sections are conceptualised and investigated, which are numbered ①, ② and ③ in Fig. 3.18. Solid lines with arrows indicate the forces due to the piezoelectric actuators. Apart from positions, the transmission path of vibrations from HP rotor to the fuselage is shown by dotted lines with arrows.

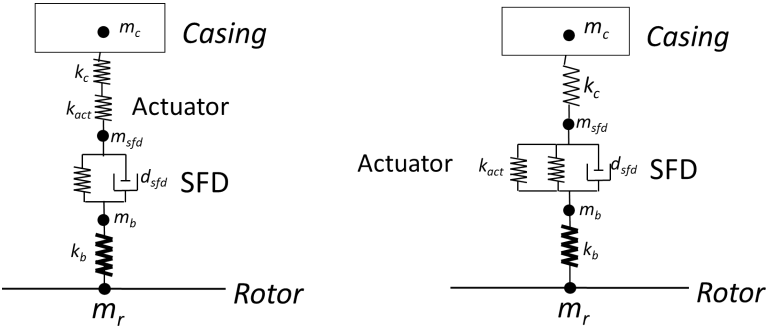

(a) Actuator in series to SFD **(b)** Actuator in parallel to SFD

Figure 3.19: Arrangement of piezoactuators in aircraft engines at HP bearings [72]

Active bearing configurations

The first placement to investigate is when actuators are located at the bearings of HP rotor (labelled ① in Fig. 3.18). The actuators are not investigated with rear bearings, due to high temperature at these locations which is not suitable for actuators. The piezoelectric actuators are mounted in the front end bearings of the HP rotor either in parallel to SFD or in series to them. A diagram of these two arrangements is shown in Fig. 3.19a and Fig. 3.19b. In these figures, the actuators are represented as a spring element (k_{act}), whereas SFDs are represented as a spring-damper system (d_{sfd}).

Active internal suspension configuration

The second placement is labelled ② in Fig. 3.18. Here the actuators are located at the struts which suspend the rotor parts on the engine casing. In this configuration, two actuators are mounted on the front struts and two in rear side linkages. In the front struts, the actuators are placed coaxially as depicted in Fig. 3.20a. The location of the actuators are indicated with double arrowed lines that indicate the forces exerted by them. The front struts are located in the same plane as the front bearing of the HP rotor. Also two actuators are proposed to be mounted in the rear side along the links as shown in Fig. 3.20b.

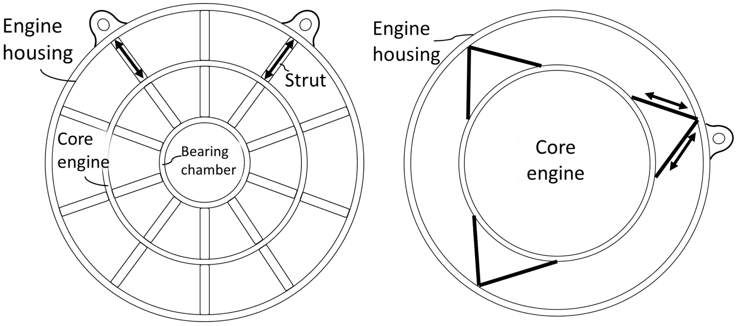

(a) Actuators in the front struts **(b)** Actuators in the rear links

Figure 3.20: Configuration of Active Internal Suspension [72]

It should be mentioned here that the rear links are not in the plane of the rear HP bearings.

Active external suspension

A third location which is the external suspension, where the actuators are mounted along the links which connect the engine to the fuselage was researched in [72]. This configuration is labelled as ③ in Fig. 3.18. But they not be analysed in this thesis, as these locations are only relevant to damp the vibrations from the engine in reaching the fuselage of the aircraft. They are far away from the HP rotor where the vibrations originate and hence are not observable.

4 Self-sensing piezoelectric actuator

4.1 Actuators

An actuator is an element which implements the command given by a controller. The output is usually mechanical power and its input is electrical power and a functional command. In Fig. 4.1, a functional block diagram of a solid-state transducer is given, out of which the right-most block is the actual actuator. It receives the voltage ($U(t)$) as input and gives a displacement ($s(t)$) as output, while acting on a system whose reaction force is ($F(t)$). This voltage is supplied by power electronics based on an actuation command ($U_i(t)$) from a controller. The stimulus for the controller is a desired displacement signal ($s_d(t)$).

The factor Γ_A represents the non-linearities in an actuator. Along with this external influences such as load reactions are responsible for the actual displacement ($s(t)$) not coinciding with the desired signal ($s_d(t)$). This can be overcome if a *feedback* controller instead of a *feedforward* controller depicted in Fig. 4.1 is used. If these controllers are integrated into the electronics of the system, they are called as *intelligent* actuators. Another class of actuators which has the highest degree of integration is called as the *self-sensing* actuators, where the actuators also possess sensing capabilities. Piezoelectric actuators are one such class of actuators and they are explained in the following sections.

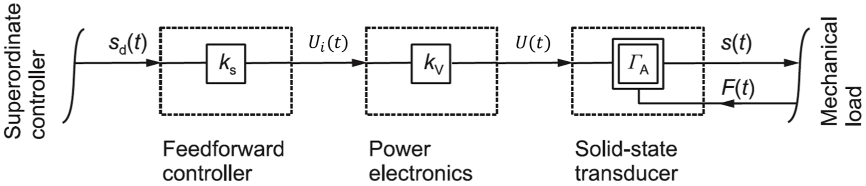

Figure 4.1: Functional diagram of a general actuator [73]

(a) Piezo actuators in different sizes [74] **(b)** Highvoltage actuator (P-025.80P)

Figure 4.2: Piezoelectric actuators

4.2 Piezoelectric actuators

4.2.1 Piezomaterials

Piezoelectric effect was first discovered by Pierre and Jacques Curie in certain class of materials such as Quartz. In such crystalline materials, the displacement of ions of individual crystals due to an external force cause an electrical field. This is called as a direct piezoelectric effect, which forms the basis for sensors working with the piezoelectric principle. On the other hand, when an external electric field is applied, the crystals deform resulting in displacement of the structure. This is the inverse piezoelectric effect or the actuator property of a piezoelectric material. Because natural elements such as Quartz, Rochelt salt exhibit very meagre piezoelectric effects, artificial materials such as Lead-Zirconate-Titanium (PZT) or Barium-Titanate ($BaTiO_3$) are usually used for piezoelectric sensors and actuators. Some of the commercially produced multilayer stack piezoactuators are shown in Fig. 4.2a, along with the actuator used in this research work (P-025.80P)(Fig. 4.2b).

4.2.2 Fundamentals of piezoelectricity

The fundamental equations of the piezoelectric actuators are given in Eq. (4.1). The individual variables and material parameters are defined in Tab. 4.1.

$$\begin{bmatrix} \mathbf{D} \\ \mathbf{S} \end{bmatrix} = \begin{bmatrix} \varepsilon^{\sigma} & \boldsymbol{d} \\ \boldsymbol{d}^{T} & s^{E} \end{bmatrix} \begin{bmatrix} \mathbf{E} \\ \sigma \end{bmatrix} \tag{4.1}$$

The different variables listed in Tab. 4.1 are tensors in generalised cartesian coordinates. The coordinate convention normally used in piezoelectricity is shown pictorially in Fig. 4.3. The diagram in the left shows the transversal directions 1,2,3 and rotational directions 4,5,6. Along with them the direction of polarisation is also shown. The basic equation can be expanded into Eq. (4.2) with respect to the axis convention discussed in [75].

Table 4.1: Variables and Parameters in piezoelectric equation

Variables		Material parameters	
E	Electrical field strength	ε^{σ}	Electrical permittivity (at constant σ)
D	Electrical flux density	$\boldsymbol{d}$	Piezoconstant
σ	Mechanical stress	s^{E}	Elastic compliance (at constant E)
S	Mechanical strain		

$$\left[\begin{array}{c} D_1\\ D_2\\ D_3\\ \hline S_1\\ S_2\\ S_3\\ S_4\\ S_5\\ S_6 \end{array}\right] = \left[\begin{array}{ccc|cccccc} \varepsilon^{\sigma}_{11} & 0 & 0 & 0 & 0 & 0 & 0 & d_{15} & 0\\ 0 & \varepsilon^{\sigma}_{22} & 0 & 0 & 0 & 0 & d_{24} & 0 & 0\\ 0 & 0 & \varepsilon^{\sigma}_{33} & d_{31} & d_{32} & d_{33} & 0 & 0 & 0\\ \hline 0 & 0 & d_{13} & s^{E}_{11} & s^{E}_{12} & s^{E}_{13} & 0 & 0 & 0\\ 0 & 0 & d_{23} & s^{E}_{21} & s^{E}_{22} & s^{E}_{23} & 0 & 0 & 0\\ 0 & 0 & d_{33} & s^{E}_{31} & s^{E}_{32} & s^{E}_{33} & 0 & 0 & 0\\ 0 & d_{42} & 0 & 0 & 0 & 0 & s^{E}_{44} & 0 & 0\\ d_{53} & 0 & 0 & 0 & 0 & 0 & 0 & s^{E}_{55} & 0\\ 0 & 0 & 0 & 0 & 0 & 0 & 0 & 0 & s^{E}_{66} \end{array}\right] \left[\begin{array}{c} E_1\\ E_2\\ E_3\\ \hline \sigma_1\\ \sigma_2\\ \sigma_3\\ \sigma_4\\ \sigma_5\\ \sigma_6 \end{array}\right] \tag{4.2}$$

For the stack actuator used in this research, only the longitudinal axis is relevant, as shown in Fig. 4.3*(b)*. Here the mechanical displacement ($\boldsymbol{S}$) is in the same direction as the electrical field ($\boldsymbol{E}$).

When a simple longitudinal actuator is considered, the tensors in Eq. (4.1) reduce to a single scalar parameter. They are rewritten in Eq. (4.3), where the individual material parameters represent only the axial direction 3 as shown in Fig. 4.3b. For example the material parameter d_{33} signifies the piezoconstant which relates the elongation of piezomaterial in direction 3, when the electric field is applied in direction 3. The operator [.] denotes non-linearity associated with that parameter, which in case of piezo materials is hysteresis.

$$\begin{bmatrix} D\\ S \end{bmatrix} = \begin{bmatrix} \varepsilon^{\sigma}[.] & d_{33}[.]\\ d_{33}[.] & s^{E} \end{bmatrix} \begin{bmatrix} E\\ \sigma \end{bmatrix} \tag{4.3}$$

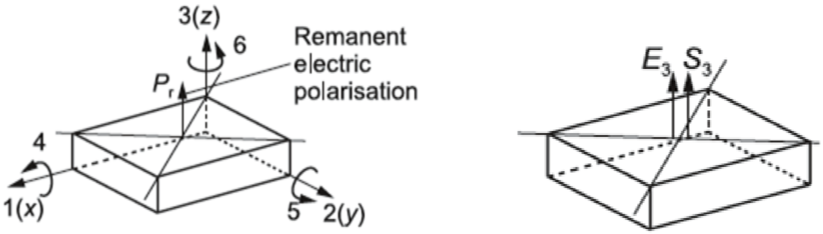

(a) Generalised cartesian coordinates

(b) Longitudinal effect

Figure 4.3: Axes convention in piezo materials [73]

The equations in Eq. (4.4) represent small signal characteristics. The characteristics assume a linear behaviour, which is valid only until 40% of the operating voltage region.

$$\begin{bmatrix} q/A_{act} \\ \Delta l/l_{act} \end{bmatrix} = \begin{bmatrix} \varepsilon^{\sigma} & d_{33} \\ d_{33} & s^{E} \end{bmatrix} \begin{bmatrix} U/l_{act} \\ F/A_{act} \end{bmatrix} \tag{4.4}$$

In Eq. (4.3) the independent variables are E and σ. This equation can be rearranged as given in Eq. (4.5) for independent variables E and S.

$$\begin{bmatrix} D \\ \sigma \end{bmatrix} = \begin{bmatrix} \varepsilon^{S} & e_{33} \\ -e_{33} & c^{E} \end{bmatrix} \begin{bmatrix} E \\ S \end{bmatrix} \tag{4.5}$$

The parameter c^E is the modulus of elasticity at constant electric field, which is the inverse of s^E. The parameter ε^S is permittivity measured at constant strain, also known as *clamped permittivity*. The parameters (ε^S) and (e_{33}) are not usually given in the manufacturer catalogue and hence should be calculated by Eq. (4.6) - (4.7) assuming linearity [55].

$$e_{33} = d_{33}c^{E} \tag{4.6}$$

$$\varepsilon^{S} = \varepsilon^{\sigma} - d_{33}c^{E}d_{33} \tag{4.7}$$

4.3 Signal reconstruction using self-sensing

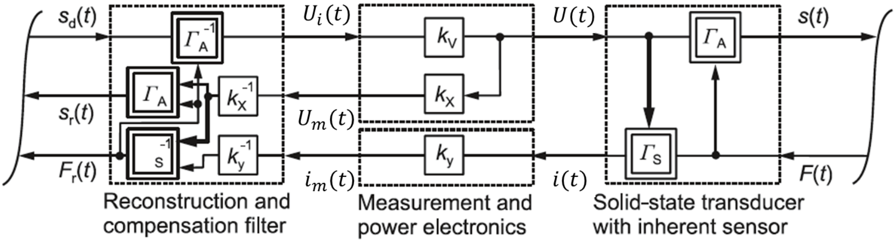

Figure 4.4: Functional diagram of a general self-sensing actuator [73]

4.3.1 Self-sensing

Piezomaterials exhibit a coupling of mechanical and electrical properties. Hence they are used in designing both sensors and actuators. With the help of this electro-mechanical coupling, the sensing property of actuators can be derived. This forms the basis of a self-sensing piezoelectric actuator.

The general principle in a self-sensing actuator can be explained with the help of Fig. 4.4. An actuator with an inherent sensor is shown in its right-most block, with the two operators Γ_A and Γ_S respectively. It also shows the inherent coupling between them. In the left-most block the mechanical properties such as displacement and forces are reconstructed by a set of filters. The sensory information is carried by the current signal ($i(t)$). Apart from it, the actuation signal ($U(t)$) is also essential. Both these quantities can be measured (U_m, i_m) with the help of power electronics block. Because these quantities are influenced by each other, a decoupling of sensory and actuation signals is essential. This process is explained analytically below and demonstrated in a test bench subsequently.

4.3.2 Self-sensing in piezoelectric actuators

In this section a two-step method will be explained, by which the electrical signals of an actuator can be used to calculate mechanical properties such as displacement.

The charge equation of an actuator from Eq. (4.5) can be re-written as given in Eq. (4.8), where it is described as function of mechanical displacement (Δl)

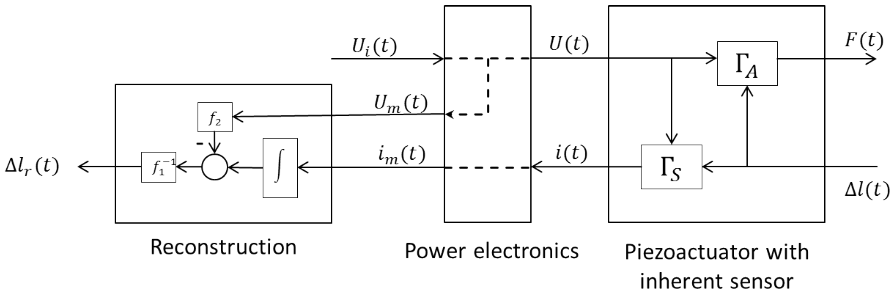

Figure 4.5: Sensor construction process of the actuator

and applied electrical voltage (U), both of the reconstruction functions f_1 and f_2 being non-linear.

$$q = f_1(\Delta l) + f_2(U) \tag{4.8}$$

Equations (4.9)-(4.11) show how the mechanical displacement, which is a physical quantity can be derived from electrical quantities such as current and voltage of the actuator.

$$\int I dt = f_1(\Delta l) + f_2(U) \tag{4.9}$$

$$f_1(\Delta l) = \int I dt - f_2(U) \tag{4.10}$$

$$\Delta l = f_1^{-1}\left(\int I dt - f_2(U)\right) \tag{4.11}$$

The entire reconstruction process can be summarised in Fig. 4.5, which will be described in following sections. The differences from Fig. 4.4 are the change of dependent and independent variables and absence of an integrated compensator.

4.3.3 Identification of actuator permittivity

In the first step towards reconstruction, the clamped permittivity of the actuator is estimated, represented in Eq. (4.11) as f_2. The permittivity of the actuator

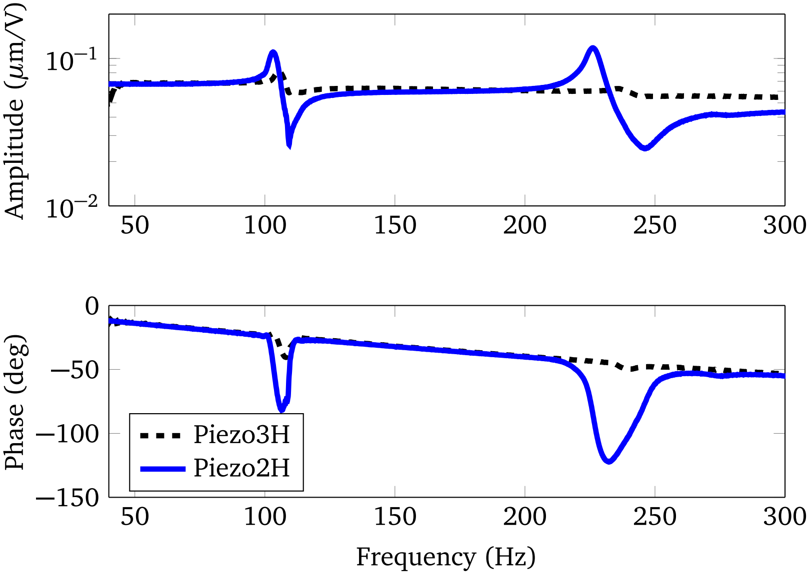

Figure 4.6: FRF of actuators in parallel planes (Actuator to Strain gauge)

exhibits a non-linear hysteresis phenomenon. To estimate it, an experimental method as suggested in [55] has been performed.

The prerequisite for this experiment is the exact knowledge of anti-resonance of the structure at the location of actuator. Two actuators which are horizontally mounted in separate planes (2H and 3H) are excited with a chirp input, when the rotor is standstill. In Fig. 4.6, the FRF between the actuator voltages and strain gauges affixed to them are shown. From Fig. 4.6, it can be observed that the anti-resonances of the actuators are located at 110 Hz. It is also seen from these two functions that the resonance and anti-resonance of actuator *3H* is damped very much compared to *2H*. Its significance is explained in the next paragraph.

Equation (4.8) can be rewritten as Eq. (4.12), where the total charge in an actuator is sum of charge due to electrical voltage (q_{elec}) and charge due to mechanical displacement (q_{mech}).

$$q = q_{mech} + q_{elec} \tag{4.12}$$

Mechanical structures are characterised by resonances and anti-resonances. At the locations of anti-resonances, the mechanical impedance is very high thereby not allowing the system to deform. Hence mechanical displacement (Δl) is very low, which means the quantity q_{mech} is not significant. According to Eq. (4.8), the charge corresponds only to electrical component. Therefore the permittivity of the actuator is determined at this operating point, because of no interference from mechanical displacement. Because the anti-resonance of the actuator 3H is not well pronounced, it leads to conclude that only actuator 2H is useful to identify the permittivity. Because only in actuator 2H at 110 Hz, a complete decoupling of mechanical and electrical signals is possible.

Sinusoidal voltage signals of different amplitudes with frequency equal to the anti-resonance frequency are given to the rotor from the piezoelectric actuator. The voltage and current are measured. The current signal is integrated to give the charge of the actuator. The permittivity is modelled by the data from the voltage and charge signal. The hysteresis have been approximated as ellipses and a curve fitting was performed. The result of hysteresis reconstruction can be seen in Fig. 4.7, where the charge and voltage of the actuator has been presented against that estimated by the model.

Equation (4.10) shows that the current signal should be integrated to derive the charge signal. Low frequency noise might be present in this signal, which distorts the integration. Hence a band-pass filter was implemented digitally to remove the low frequency disturbance in the current signal. This digital Finite Impulse Response (FIR) filter allows the signal in the frequency band 40-1000 Hz. Because our operating range is only upto 300 Hz, this filter can be assumed to be a high-pass filter. It has its corner frequency 20 Hz and constructed with an order of 200. This order was chosen to remove the low frequency noise within a narrow band 0-20 Hz and have a steep rise in amplitude response, so that the operating range 50-300 Hz remains unaffected. This is seen in Fig. 4.8, where the magnitude response of the filter has been plotted. Both the current and voltage are subjected to this high-pass filter during the self-sensing reconstruction before the curve fitting is performed.

At the position of anti-resonance, the phase of the structure shifts by 180°. Hence the precise position of anti-resonance is important, otherwise phase would be distorted during reconstruction. Hence this method is sensitive to identification of the anti-resonance frequency.

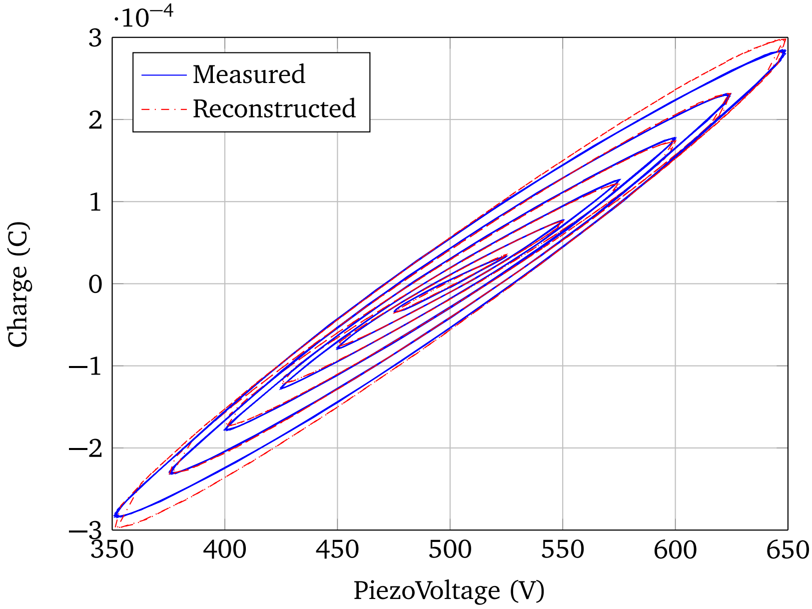

Figure 4.7: Hysteresis estimated from piezoelectric actuators

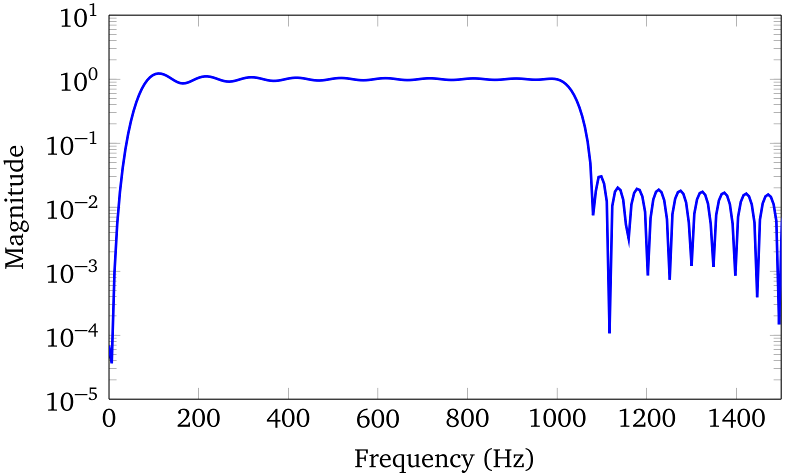

Figure 4.8: Magnitude response of band-pass filter

4.3.4 Construct mechanical displacement

In the second step, mechanical displacement of actuator is constructed from the mechanical equivalent of charge (q_{mech}). The inverse function f_1^{-1} should be estimated. For its estimation, the test bench was run-up so that the actuator is subjected to a wide range of mechanical force and thereby a wide range of displacement.

The relation between mechanical charge derived from previous step and displacement from strain gauge was compared. This comparison which represents the function f_1^{-1} was found to be linear. And hence this function was approximated by a scalar factor.

4.3.5 Validation of virtual sensor signals

The test bench is run at different conditions and signals from real strain gauges are recorded. The reconstructed displacement signals from the two step method are compared with these real signals. The result in time domain is plotted in Fig. 4.9 for a stationary operating speed at 8000 rpm. It shows a good agreement between the two signals. A fine difference can be seen in the amplitude peaks. During reconstruction the displacement is calculated for each sample out of current and voltage signal. However in real structures damping plays a role and reduces the achievable peak in reality. Because of this the real signals are damped compared to the reconstructed virtual signals.

The plot in Fig. 4.10 compares the FRF of piezo voltage to the real and virtual displacement signals. The function was derived by a chirp voltage signal from the piezoelectric actuator. There is a good agreement in the amplitudes in most of the operating range. At the low frequency range ($f<50\,\text{Hz}$) the deviation is because of the high-pass filter. At frequencies ($f>230\,\text{Hz}$), the reconstructed amplitude is not accurate because as the frequency increases the reconstruction algorithm (working at a sampling frequency of 10 000 Hz) is not fast enough in real time.

4.4 Closed loop controller with self-sensing piezoelectric actuator

The virtual sensor signal needs to be validated for its effectiveness as a sensor in a closed control loop. This is needed to prove the ability of the piezoelectric

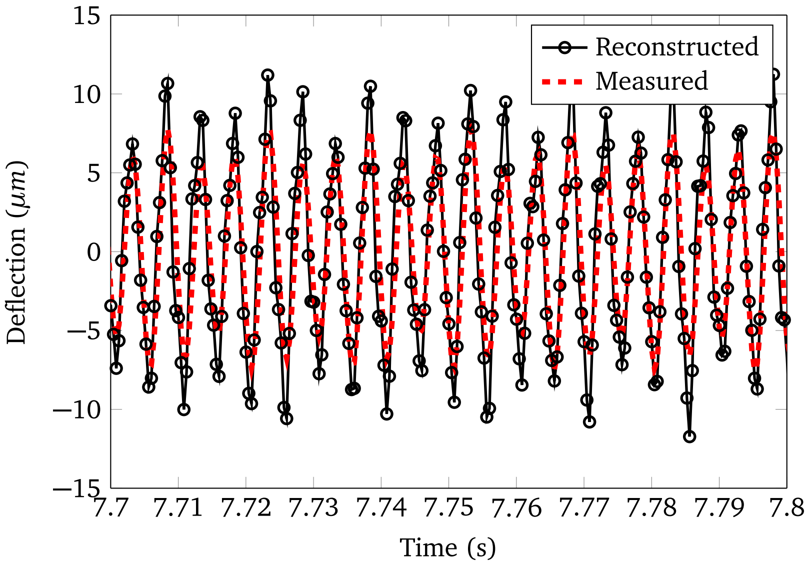

Figure 4.9: Compare displacement signals in time domain

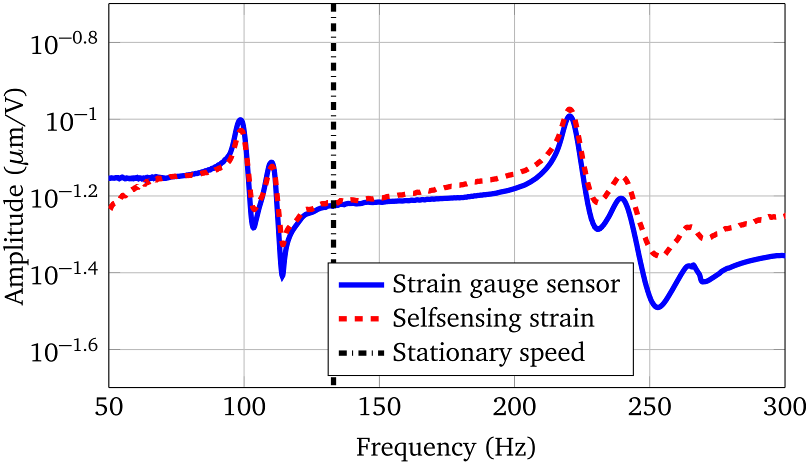

Figure 4.10: Comparison of FRF between the voltage and displacement signal

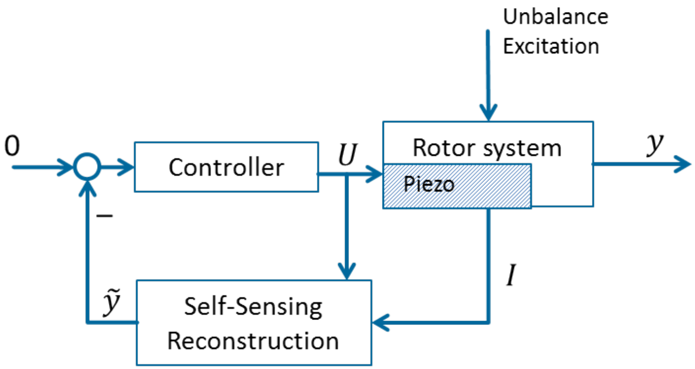

Figure 4.11: Block diagram of self-sensing in a closed loop

actuator to actuate and sense at the same time. In this section, self-sensing piezoelectric actuator is validated with two different controllers in a closed control loop. The block diagram is shown in Fig. 4.11, where the controller accesses the virtual signal from the self-sensing reconstruction block.

Two different controllers are presented in the sections below. The first is a PPF controller (Section 4.4.1) which damps the resonance. The second is an adaptive controller using the FxLMS algorithm (Section 4.4.2).

Because virtual displacement signals are available, both the algorithms attempt to reduce the displacement of the bearings. This means that the bearings become stiff. In vibration control, this is a problem of *vibration minimisation* as opposed to *vibration isolation* problem where the bearing forces are controlled.

4.4.1 Vibration reduction in a narrow frequency band

A Positive Position Feedback (PPF) controller has been implemented to validate the self-sensing reconstruction of the piezoelectric actuator in a closed loop. The controller has been described briefly in Appendix A.

The rotor test bench was accelerated from 4000-8000 rpm in 18 s within which the first resonance occurs at 6500 rpm. The PPF controller was designed to damp this resonance only. It was implemented separately with three different control signals (variable x represented in Fig. A.1). In the first case, the signals from strain gauge affixed to the piezo actuator has been used as control signal. In second case control signal x corresponds to the reconstructed signal through self-sensing. The third case also corresponds to a same reconstructed strain signal, except that the capacitance has been assumed to be linear instead of hysteretic.

The achieved control performance can be seen in Fig. 4.12a. Here the strain signals in one of the actuator in a passive run has been compared with cases with the closed loop PPF controller. It can be observed that the resonance peaks have been damped upto 33%.

The peak of resonances have been damped to the same extent for all the three cases. This shows the ability of the virtual reconstructed signals in vibration reduction to same extent as the control signal from a real sensor. The last line shows the resonance damping by the algorithm, when the capacitance of the actuator was approximated to be linear, instead of hysteretic. In the result, there is no difference to be seen between case of linear or hysteretic capacitances. The reason can be identified from Fig. 4.12b, where the actuator voltage is shown when the three different control signals are considered. The voltages have a maximum amplitude less than 40 V at the resonance, which is still in the range where a linear approximation is sufficient. Another inference from the figure is that the controller is effective only in reducing a narrow frequency band near the resonance peak. The vibration is not reduced at an operating point away from it as can be seen in the area lower than 6000 rpm. The reason is due to the very nature of the PPF transfer function as given in Eq. (A.1), which is designed only for a particular resonance frequency peak ω_f to be attenuated.

4.4.2 Vibration reduction at a stationary operating point

In order to reduce vibrations at an operating point away from the resonance, a feedforward adaptive algorithm such as FxLMS can be implemented. The adaptive algorithm uses the reconstructed displacement signals as the sensor input to attenuate vibration.

An introduction to FxLMS algorithm has been presented in Appendix B. In the present case the algorithm is designed to attenuate disturbances in a narrow frequency band. They have been implemented in two different speeds of the rotor 8000 rpm and 10 000 rpm. Two actuators which are orthogonal to

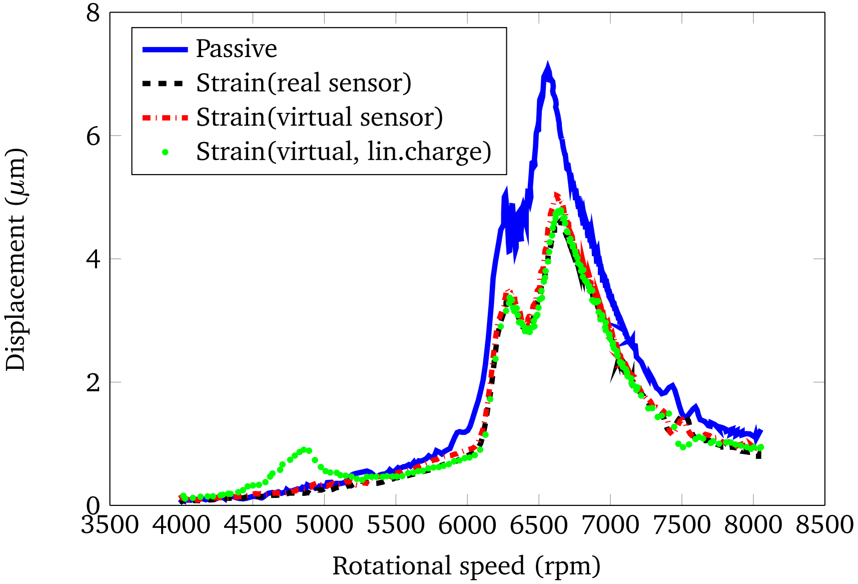

(a) Resonance reduction

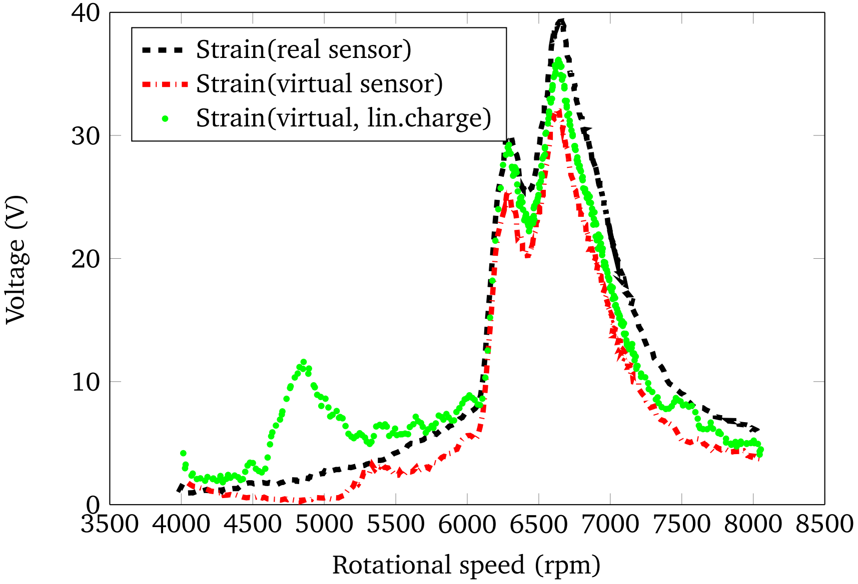

(b) Actuation voltage

Figure 4.12: Performance of PPF Controller

each other in the same plane are chosen to reduce vibration in perpendicular directions.

At a steady-state rotation speed, the controller was switched on for approximately 8 s. The same tuning parameters of the algorithm (γ and μ) were applied to both the actuators. The result can be seen in Fig. 4.13 for the rotor speed 8000 rpm. The two separate plots show that the bearing displacement has been reduced in the both horizontal (2H) and vertical (2V) directions in the same plane.

At the outset, it can be observed that bearing displacements are reduced by around 50% in both the directions. This is reflected from the strain gauge signal and also the reduction in reconstructed signals. The ability of the virtual sensor to replace the strain gauges is evident here as well. Because the extent of reduction and also the individual signals have the same trend.

As seen from Fig. 4.13, they have different dynamics in perpendicular direction when the same algorithm is used. This can be inferred from the transient behaviour of the signals when the controller is switched on at (t=4 s). This shows the inherent difference between the two actuators in perpendicular positions. In [76], the piezoelectric actuators in perpendicular directions were assumed to be same and the same capacitance was used in the reconstruction algorithm. Later, the capacitance in both actuators have been estimated separately. Because the dynamics are still different, the tuning parameters of the FxLMS algorithm should be chosen separately for the actuators. This experiment validates the use of signals from the virtual sensor as controlled signal in a closed control loop. Hence the reconstructed signals were proven to be effective in simultaneous actuation and sensing mode at an operating frequency away from resonance.

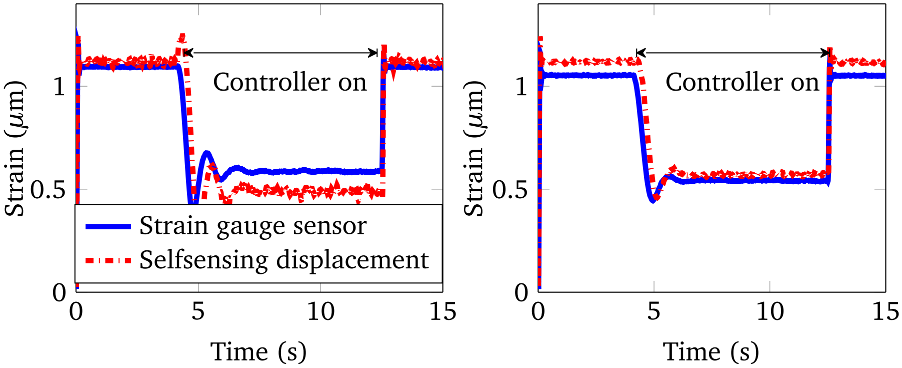

(a) Piezo 2H **(b)** Piezo 2V

Figure 4.13: Performance of FxLMS algorithm

5 Fault detection in rotor systems

Fault detection in machines can be performed either by signal-based or model-based methods. A signal-based method analyses the measured signal for specific characteristics such as frequency, amplitudes and variances of signals, which are known as symptoms of faults. Some of the analysis methods include correlation analysis, fourier analysis and ARMA models. Along with these analytical symptoms, heuristical symptoms such as noise, colour, smell etc. can be included. Altogether error can be diagnosed with the help of error-symptom maps or by classification methods [77].

In a model-based method, the real system should be modelled mathematically with a good degree of accuracy. There are different methods to diagnose faults such as parity equations, parameter estimation techniques. The former method is used for a stationary operating point or for additive faults. The latter method is used for instationary operation or for multiplicative faults. A combination of signal and model-based methods would lead to identification of a larger number of faults in systems [57].

A possibility to extend the fault diagnosis to different fault types should be available. Because of this reason, the model-based method is opted for in this research work. Rotational systems are characterised by gyroscopy which is a rotational speed dependent phenomenon. In other words, rotor systems are LPV systems. Vibration surveys in real aircraft engine tests are carried out in quasi-static conditions, where the engine is accelerated very slowly. Hence parameter estimation techniques are applied to detect unbalance faults in rotor systems.

5.1 Fault detection in time domain

From the basic equation of motion Eq. (3.10) of a mechanical system, the acceleration, velocity and displacements can be rewritten as Eq. (5.1). Here the generalised vectors ($\mathbf{q}, \dot{\mathbf{q}}$ and $\ddot{\mathbf{q}}$) are to replaced by the translational DOF and the rotational DOF are omitted. The symbol Δ denotes the change in the respective signals from the reference signals due to an external force.

$$\mathbf{M}\Delta\ddot{\mathbf{y}}(t) + (\mathbf{D} + \Omega\mathbf{G})\Delta\dot{\mathbf{y}}(t) + \mathbf{K}\Delta\mathbf{y}(t) = \mathbf{F}(t) \tag{5.1}$$

Let the displacements of positions where the sensors are located be denoted by $\Delta\mathbf{y}_m$ and let m DOF be measured. These signals are a subset of the complete displacement vector $\Delta\mathbf{y}$. They can be related to each other by a Boolean matrix C, as given in Eq. (5.2).

$$\Delta\mathbf{y}_m(t) = C \cdot \Delta\mathbf{y}(t) \tag{5.2}$$

Modal expansion method can be used as implemented in [78] to obtain the deflections at all DOF from a few DOF. Equation (5.3) shows how a few displacement vectors could be expanded to displacement of all the DOF of the mechanical system. The eigenvector matrix Φ contains the mode shapes of all DOF, from which a reduced matrix $\hat{\Phi}$ can be derived. This reduced matrix contains k mode shapes such that $k \leq m$ [18].

The advantage of the modal expansion method is proven in [79] in comparison to the basis dynamic expansion method. Matrix $\mathbf{T}$ in Eq. (5.4) transforms few displacements to all DOF. This transformation matrix can be calculated from the finite element model of the system a-priori.

$$\begin{aligned} \Delta\mathbf{y}(t) &= \left\{\hat{\Phi}\left[(C\hat{\Phi})^T(C\hat{\Phi})\right]^{-1}(C\hat{\Phi})^T\right\}\Delta\mathbf{y}_m(t) && (5.3)\\ &= [\mathbf{T}]\Delta\mathbf{y}_m(t) && (5.4) \end{aligned}$$

Fault parameters are then estimated by least squares method as mentioned in expressions (5.5) and (5.6). The former is called as *Equivalent vibration minimisation method* and the latter *Equivalent load minimisation method*.

$$min\left\{\int\left|\Delta\mathbf{y}_{ml}(t) - \Delta\mathbf{y}_m(t)\right|^2 dt\right\} \tag{5.5}$$

$$min\left\{\int|\Delta\mathbf{F}_{ml}(t) - \Delta\mathbf{F}_m(t)|^2 dt\right\} \tag{5.6}$$

The vectors $\Delta\mathbf{y}_{ml}$ and $\Delta\mathbf{F}_{ml}$ represent the displacement and force vectors calculated from the model respectively. According to Eq. (5.5), the difference between displacements calculated from the model and that from measurements are minimised and unbalance parameters (magnitude, phase) are calculated.

Equation (5.6) represents a similar approach, but minimises the forces at all DOF. This indirect method comprises five steps as listed below, and also shown in Fig. 5.1.

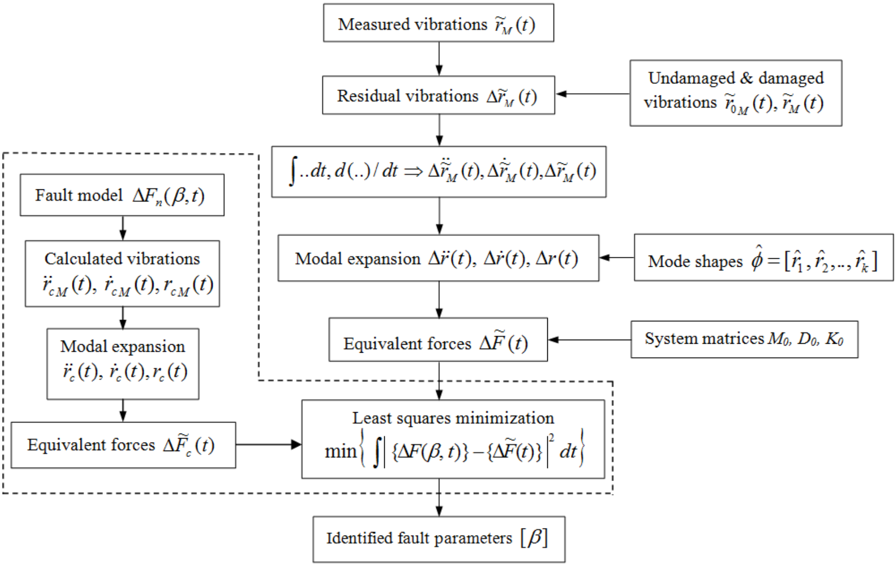

Figure 5.1: Modified equivalent load minimisation method for unbalance detection in time domain [20]

1. The signal from displacement sensor is expanded according to Eq. (5.3) to displacement at all DOF.
2. They are differentiated to calculate velocity and acceleration vectors at the corresponding DOF.
3. Using Eq. (5.1), forces at individual DOF ($\Delta F_m(t)$) are calculated.
4. With an initial assumption of unbalances in model, the forces ($\Delta F_{ml}(t)$) are calculated.
5. The difference of these forces are minimised according to Eq. (5.6), to find the actual unbalance.

Towards identifying the parameters of unbalance in [78], a different approach had been suggested, by which phase and the magnitude could be identified separately. Because the displacement signals are sinusoidal and synchronous with the rotation speed, correlation analysis between the displacement signal

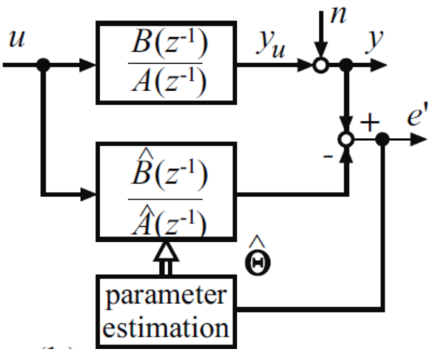

Figure 5.2: Parameter estimation by output-error method [57]

of the model and the measured could directly identify the phase. The amplitude of the signals could be separately substituted in Eq. (5.5), to identify the magnitude of unbalance.

5.2 Fault detection in frequency domain

5.2.1 Introduction to parameter estimation method

A dynamic process when described in a linear time difference equation form can be written as in Eq. (5.7).

$$y(k)+a_1y(k-1)+\cdots+a_my(k-m)=b_1u(k-k_d-1)+\cdots+b_mu(k-k_d-m) \quad (5.7)$$

In this equation k_d is the discrete time delay, k is the discrete sample and a_i and b_j are parameters of this process. The parameters are combined into a parameter vector as given in Eq. (5.8). The signals $y(k)$ and $u(k)$ represent the output and input samples at the instance k. They are combined together as Ψ which is called the data vector as given in Eq. (5.9).

$$\hat{\Theta}=\left[\hat{a}_1\cdots\hat{a}_m,\hat{b}_1\cdots\hat{b}_m\right] \quad (5.8)$$
$$\Psi=\left[-y(k-1)\cdots-y(k-m),u(k-k_d-1)\cdots u(k-k_d-m)\right] \quad (5.9)$$

The problem of parameter estimation involves identification of the parameters in the vector $\hat{\Theta}$ (Eq. (5.8)). In this thesis, the output-error method of parameter estimation is used as it uses the transfer function of the system directly. The time difference equation (Eq. (5.7)) can be transformed into z-domain, where the transfer function $G(z)$ of this process can be derived as given in Eq. (5.10) and (5.11).

$$G(z) = \frac{y(z)}{u(z)} = \frac{B(z^{-1})}{A(z^{-1})} \tag{5.10}$$

$$= \left[\frac{b_1 z^{-1} + \cdots + b_m z^{-m}}{1 + a_1 z^{-m} + \cdots + a_m z^{-m}}\right] z^{-d} \tag{5.11}$$

The output-error method is defined by Eq. (5.12) and (5.13), and its schematic is given in Fig. 5.2.

$$e(k) = y(k) - y_m(\hat{\Theta}, k) \tag{5.12}$$

$$y_m(\hat{\Theta}, z) = \frac{\hat{B}(z^{-1})}{\hat{A}(z^{-1})} u(z) \tag{5.13}$$

Equation (5.12) shows the error $e(k)$ between the output signals of the system and its model, and hence the name of the method. The output signal in Eq. (5.12) can be substituted by parameter and data vectors which transform them to Eq. (5.14). The loss function to be minimised for the parameters is Eq. (5.15) according to least squares sense.

$$e(k) = y(k) - \Psi(k)\hat{\Theta} \tag{5.14}$$

$$\sum_{i=1}^{N} e^2(k) = e^T(k)e(k) \tag{5.15}$$

In order to obtain a minimum, the loss function should be differentiated once (Eq. (5.16)) from which the optimal value of parameter vector (Eq. (5.18)) can be obtained. The condition for minimality (Eq. (5.19)) is obtained by differentiating it once more (Eq. (5.17)).

$$\frac{dV}{d\Theta} = -2\Psi^T[y - \Psi\hat{\Theta}] \tag{5.16}$$

$$\frac{\partial^2 V}{\partial\Theta\partial\Theta^T} = \Psi^T\Psi \tag{5.17}$$

$$\hat{\Theta} = \left[\Psi^T\Psi\right]^{-1} \Psi^T y \tag{5.18}$$

$$\det\left[\Psi^T\Psi\right] > 0 \tag{5.19}$$

The minimality condition in Eq. (5.19) means that the term in the brackets should be positive definite. From Eq. (5.9) this means the input and output vectors should not be zeros. In other words, the system should be persistently excitable by the input.

For our case of rotor system, it means that the rotor should be rotating to detect faults. A standstill rotor cannot yield any result. This is explained more in the following sections.

5.2.2 Rotor system in frequency domain

Let us consider the equations of motion of a system subjected to an external force as given in Eq. (5.1). It can be represented in frequency domain as given in Eq. (5.20). Here the vector $F(s)$ is the external force exciting the structure and $Y(s)$ is the response of the system. When the imaginary part of Laplace operator $s = i\Omega$ is substituted, the equation turns out to Eq. (5.22). The mechanical structure can be represented as the term within the brackets, which is as dynamic stiffness matrix K_{dyn} as given in Eq. (5.23). The frequency domain response of the structure can be calculated as given in Eq. (5.24).

$$\mathbf{M}s^2Y(s) + (\mathbf{D} + \Omega\mathbf{G})sY(s) + \mathbf{K}Y(s) = F(s) \tag{5.20}$$

$$\left[\mathbf{M}s^2 + (\mathbf{D} + \Omega\mathbf{G})s + \mathbf{K}\right]Y(s) = F(s) \tag{5.21}$$

$$\left[-\mathbf{M}\Omega^2 + (\mathbf{D} + \Omega\mathbf{G})i\Omega + \mathbf{K}\right]Y(\Omega) = F(\Omega) \tag{5.22}$$

$$\mathbf{K}_{dyn}Y(\Omega) = F(\Omega) \tag{5.23}$$

$$\underbrace{\mathbf{K}_{dyn}^{-1}}_{\hat{\Theta}}\underbrace{F(\Omega)}_{\Psi} = \underbrace{Y(\Omega)}_{y_m} \tag{5.24}$$

The force vector $F(\Omega)$ denotes the unbalance forces acting at the particular degrees of freedom where the unbalance masses are present. This vector is expanded in Eq. (5.25), where all the nodes except node p, is zero. The unbalance mass m is present at node p at a radius of ϵ from the center of rotation axis. When the rotor is at a speed of Ω, the centrifugal force is $m\epsilon\Omega^2$ which is also the unbalance force acting on the system. From this equation it can be seen that each node has four DOF and that there are two for translational and two rotational DOF per node.

$$F = m\epsilon\Omega^2 e^{i\phi} * \begin{bmatrix} 0\ 0\ 0\ 0\ \cdots \underbrace{1\ 0\ -i\ 0}_{node\ p} \cdots 0\ 0\ 0\ 0 \end{bmatrix} \tag{5.25}$$

5.2.3 Fault detection

Let us differentiate between the degrees of freedom which can be measured $Y_s(\Omega)$ and those which cannot be $Y_n(\Omega)$, as shown by Eq. (5.26).

$$Y(\Omega) = \{Y_s(\Omega) \cup Y_n(\Omega)\} \tag{5.26}$$

The inverted dynamic stiffness matrix can be rearranged to accommodate only the relevant lines according to Y_s and represented as another matrix R as given in Eq. (5.27).

$$Y_s(\Omega) = \mathbf{R} \cdot F(\Omega) \tag{5.27}$$

The measured displacements with the help of a sensor in the structure can be represented as $Y_m(\Omega)$ in frequency domain. For a fault-free system, it should be the same as the signal determined from model Eq. (5.24). In other words, their difference is zero as mentioned by Eq. (5.28).

$$\delta = Y_s(\Omega) - Y_m(\Omega) = 0 \tag{5.28}$$

When information of the structure contained in the dynamic stiffness matrix can be substituted from Eq. (5.27) into Eq. (5.28), the equation turns into Eq. (5.29).

$$\delta = \mathbf{R} \cdot F(\Omega) - Y_m(\Omega) = 0 \tag{5.29}$$

In this equation known information is the measured quantities Y_m and unbalance parameters are the unknowns. The number of elements in vector F can be n, which is also the total DOF of the finite element model. The number of measured DOF is smaller than n. Even if there are multiple faults, there are more equations in Eq. (5.29) than the faults. The parameters of the faults should be computed by solving a system of equations with less unknowns than the number of equations. Hence it is a statistically overdetermined system, which has no solution. A solution is obtained by least-squares solution method. In other words the unbalances are the results for which the L_2 norm as shown in Eq. (5.30) is minimum, but not zero.

$$min \, ||\mathbf{R} \cdot F(\Omega) - Y_m(\Omega)||_2 \tag{5.30}$$

The output error method of parameter estimation (Eq. (5.13)) is non-linear in parameters. In our case the unknown parameter is unbalance. The two unknown variables which can be represented together as a complex value $m\epsilon e^{i\phi}$ appear as a multiple of the tranfer function in the right hand side. Hence in this case, it is a linear parameter estimation method.

5.2.4 Relative residual

The unbalance identification procedure is carried out at all possible finite element nodes in the rotor shaft. In other words, by assuming the unbalance to be at n^{th} node, the equation Eq. (5.30) is solved. Only at the exact position where the real unbalance is located, the objective function is at its minimum. Which means that only at this location, the residual Eq. (5.29), becomes zero or closer to zero. At other locations, only an approximate identification could be possible. This is called as *hypothesis of localisation of faults*. Hence to identify the location of faults, a scalar value called *relative residual* is derived Eq. (5.31).

$$\delta_r = \sqrt{\left(\frac{\delta^{*T}\delta}{Y_m^{*T} Y_m}\right)} \tag{5.31}$$

The value δ_r is zero or minimum at the exact position where the unbalances are located. This can also be visually presented by plotting the relative residual values against all the finite element nodes and identifying the location of minimum.

In order to calculate the relative residual, the unbalance parameters should be identified by running the least squares estimate problem at each finite element node where the unbalances are probable. This certainly increases the computational time. In [21], multiple faults in rotors are analysed, in which case the the computational time increases by the times of number of faults. In case of two faults, the relative residual can be visualised as a plane whose minimum occurs at finite element nodes of the first and second faults.

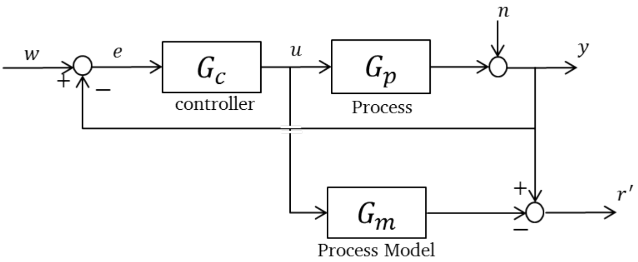

Figure 5.3: Fault detection in a closed loop system [57]

5.3 Fault detection in closed loop

A previous work by [56] describes fault detection of components in a closed control loop. It was concluded that to develop a combined controller and FDI, two different strategies can be employed. The first is a coupled strategy where the controller and FDI system are developed together. The second is a decoupled strategy where they are developed independently of each other and merged. In the present work, the second strategy has been followed. Since the aim of research is only about use of self-sensing actuator, a simple control strategy to minimise vibrations in a collocated system has been implemented (Section 4.4.2).

The block diagram in Fig. 5.3 shows the fault detection in a closed loop system. Here G_p represents the actual process and its model is denoted by G_m. A controller G_c generates a actuation signal which is then applied on the process. The follow-up control algorithm tries to make the signal y follow a reference signal w. To diagnose faults in this loop, the actuation signal is applied to the model of the process. The deviation from the actual behaviour is termed as residue r, on which fault diagnosis is based on.

In a closed control loop, faults are mitigated by a control action of an actuator which acts according to design of a controller. For controllers involved in active vibration control, the set point or a reference signal to be followed is zero. It can be either a vibration isolation problem where the force at bearings are minimised or a vibration minimisation problem where the displacement of the rotor system is minimised. Adaptive algorithms such as the FxLMS are capable of reducing the vibration amplitudes.

In these cases the vibration energy is compensated by the actuation force. With a piezoelectric actuator, the actuation voltage compensates the vibration. This means that the relevant sensors or the displacement signals are reduced to zero or very low amplitude. When such algorithms are used, the quantity Y_m as defined in Eq. (5.29) is zero or has a very low amplitude and leads to wrong estimation of faults. Therefore in this case unbalance detection only from sensors will not lead to correct results. Hence Eq. (5.29) should be extended to include the actuation force as well. Hence the actuating signals are also relevant for fault detection as given in Eq. (5.35).

$$\mathbf{K}_{dyn} Y(\Omega) = F(\Omega) + F_U(\Omega) \tag{5.32}$$

$$Y(\Omega) = \mathbf{K}_{dyn}^{-1}\left[F(\Omega) + F_U(\Omega)\right] \tag{5.33}$$

$$Y(\Omega) = \mathbf{K}_{dyn}^{-1} F(\Omega) + \mathbf{K}_{dyn}^{-1} F_U(\Omega) \tag{5.34}$$

$$Y(\Omega) - \mathbf{K}_{dyn}^{-1} F_U(\Omega) = \mathbf{K}_{dyn}^{-1} F(\Omega) \tag{5.35}$$

In these equations the vector $F_U(\Omega)$ denotes the actuation force due to the voltage of piezoelectric actuators. This force can be calculated with Eq. (3.9) from the actuation voltage, by assuming a linear behaviour of actuators. Equation (5.35) contains measurable quantities such as the displacements and actuation force in the left hand side and the unknown unbalance force in the right hand side of the equation. They can be rewritten for the least square calculation as given in Eq. (5.36).

$$\underbrace{\mathbf{R}}_{\hat{\Theta}} \cdot \underbrace{F(\Omega)}_{\Psi} = \underbrace{Y_m(\Omega) - \mathbf{R} \cdot F_U(\Omega)}_{y_m} \tag{5.36}$$

The unbalance detection due to an active vibration minimisation algorithm such as FxLMS is presented in Section 6.3.4. In Appendix B, a brief introduction to the used algorithm is presented.

5.4 Robust fault detection

Fault detection in frequency domain as discussed in Section 5.2.3, was performed by solving an overdetermined system of linear equations by least squares approach Eq. (5.30). Though the least squares method is certainly a convex optimisation approach, it is sensitive to data corruption. It is because a fundamental assumption in LMS is that the errors have a null mean value. Systematic errors in experimental investigation can cause the estimate to be inaccurate. Hence it is not a robust method because it suffers from problems of outliers in the residual (Eq. (5.14)). An outlier is defined as data point far away from the majority of data.

In order to address this problem, robust fault detection techniques have been investigated in [80]. Weighted least squares (WLS) has been suggested as a good alternative to the conventional least squares approach. Here the weights are derived by knowing the variance of the noise with which the data is corrupted. These weights can be generated automatically by a robust estimate called as *M-estimators*.

5.4.1 Theory of M-estimators

A detailed theory about the derivation of weights from M-estimators is presented in this section. Let us consider a generalised error minimisation problem as given by Eq. (5.37). As inferred from it, the residue (e) is the difference between the estimated and measured variables at the respective DOF. The L_2 norm given in Eq. (5.38) is one of the many functions which could be defined out of it. These are objective functions (ρ) operating on the residue to be minimised.

$$\rho(e) = \rho(\hat{x} - x) \tag{5.37}$$

$$\rho(e) = \frac{e^2}{2} \tag{5.38}$$

Differentiating Eq. (5.37) with respect to the residues and setting it to zero, for point of minimum

$$\sum_{i=1}^{n} \psi(e_i) \frac{\partial e_i}{\partial \theta_j} = 0 \text{ for } j = 1 \cdots m \tag{5.39}$$

where the derivative $\psi(e_i)$ is proportional to the function ρ

$$\psi(e_i) = \frac{d\rho(e_i)}{de_i} \tag{5.40}$$

A weight function as defined in Eq. (5.41) when substituted in Eq. (5.39) gives Eq. (5.42).

$$w(e_i) = \frac{\psi(e_i)}{e_i} \tag{5.41}$$

$$\sum_{i=1}^{n} w(e_i) e_i \frac{\partial e_i}{\partial \theta_j} = 0 \text{ for } j = 1 \cdots m \tag{5.42}$$

As quoted in [81], Eq. (5.42) is similar to solving an iterated re-weighted least squares problem which is solved by the optimisation function Eq. (5.43).

$$\min \sum_{i=1}^{n} w(e_i^{t-1}) e_i^2 \tag{5.43}$$

The function as given in Eq. (5.44) is called as the Huber function which was introduced in [82] and further used in [83]. Further derivations are restricted only to this function. When Eq. (5.44) is considered, the weights can be derived as in Eq. (5.45).

$$\rho(e) = \begin{cases} \frac{e^2}{2} & \text{if} \, |e| \leq c, \\ c\left(|e| - \frac{c}{2}\right) & \text{if} \, |e| > c \end{cases} \tag{5.44}$$

$$w(e) = \begin{cases} 1 & \text{if} \, |e| \leq c, \\ \frac{c}{|e|} & \text{if} \, |e| > c \end{cases} \tag{5.45}$$

In this case, c is called the tuning parameter calculated from $\hat{\sigma}$ (Eq. (5.46)), which is called as the median absolute deviation of the data. The numerical scaling factor is determined by assuming a normally distributed data points having 95% asymptotic effectiveness.

In classical statistics the median absolute deviation is mentioned for real data points. However the residual values are complex numbers which are distributed in a two dimensional plane. With the help of Tukeys median method, the median absolute deviation can be derived (Eq. (5.47)), where $T(.)$ is the Tukey median operator.

$$c = 1.345\hat{\sigma} \tag{5.46}$$

$$\hat{\sigma} = \text{median}\left(|e - T(e)|\right) \tag{5.47}$$

Apart from Huber function, many different weighing functions have been compared in [81]. It was concluded to be the best choice and was also used for fault detection purposes in [80].

5.4.2 Recursive method

In our present problem, the outliers could be in measured data due to measurement errors or in estimate of the model due to uncertainties. When their effects are combined, the differences between these two are affected (Eq. (5.28)). This is reflected in the residues (δ), where one or two points are away from the majority, which is near zero. Therefore weights which should be calculated depend on the residuals. But from Eq. (5.29) the residuals depend on the estimated unbalances. The unbalance estimation is in turn dependent on solution of LS.

To solve this loop, an iterative recursive method is developed in [80] to identify the unbalance in a robust manner. This necessitates another inner loop and thereby increase the computation time. The iterative method is presented below.

1. Calculate the initial estimate for unbalance ($m\epsilon^{(1)}$) using the normal least squares approach (Eq. (5.30)).

   Iteration *(t)*

2. Calculate residues of individual data points (δ_i^t) from Eq. (5.29) and weights ($\mathbf{W}^t$) for each data point used in the previous iteration ($t-1$) from Eq. (5.45).
3. Calculate a new weighted least squares estimate for the unbalances using Eq. (5.48).
4. Repeat the above two steps until a convergence is achieved according to a criteria Eq. (5.49) or when maximum number of iterations are reached.

$$(m\epsilon e^{i\phi})^{(t+1)} = \left[\Psi^T \mathbf{W}^{(t)} \Psi\right]^{-1} \Psi^T \mathbf{W}^{(t)} \mathbf{y} \tag{5.48}$$

$$max \begin{pmatrix} \left|Re(m\epsilon^{(t)}) - Re(m\epsilon^{(t-1)})/Re(m\epsilon^{(t-1)})\right| \\ \left|Im(m\epsilon^{(t)}) - Im(m\epsilon^{(t-1)})/Im(m\epsilon^{(t-1)})\right| \end{pmatrix} < 10^{-4} \tag{5.49}$$

6 Results and discussion

The individual systems presented in the preceding chapters (3-5) are put together in this chapter and results are derived. Faults are detected with the help of bearing displacements at the respective rotor systems. Instead of separate displacement sensors, signals from actuators which are placed in bearings can be used to derive their displacement. Apart from magnitude and phase of unbalances, their position were determined with the help of relative residual presented in 5.2.4.

This chapter is ordered in the following way. In Sections 6.1, 6.2 results from simulations using model of the rotor system at IMS are presented. This is followed by unbalances diagnosed with data measured from the test bench in Section 6.3. Unbalance detected from virtual strain signals are compared from those obtained from real strain gauge signals. Apart from stationary tests, quasi-static and simultaneous actuation and sensing cases are also tested.

Subsequently in Section 6.4, the high pressure rotor model of an aircraft engine is analysed with its three different actuator configurations.

At the end, all the results are discussed and conclusions derived. Out of all the results, a good unbalance detection is considered when the relative error in magnitude is within ±25% and when the absolute phase deviation is within ±45°.

6.1 Fault detection in time domain

Fault detection was simulated with a model of the test bench rotor in MATLAB. In this simulation, the model of the system is compared against the same model for faults. The signals representing those measured from sensors are corrupted with band limited noise to emulate conditions of disturbances in real measurements.

As seen in Tab. 6.1, unbalances were detected in stationary operating points both in simulation and in test bench. In simulations, the unbalance magnitude

Table 6.1: Unbalance detected from time domain FDI

Rot.Speed	Test unbalance		Detected unbalance		Error
	Magnitude	Phase	Magnitude	Phase	rel
rpm	[gmm]	[deg]	[gmm]	[deg]	[%]
			Simulated		
8000	90	200	83.91	201.2	-6.8
8000	100	200	93.9	201.2	-6.1
8000	150	200	143.9	201.2	-4.06
8000	150	100	143.9	100.8	-4.06
8000	150	75	143.9	79.2	-4.06
8000	150	45	143.9	43.2	-4.06
			Measured		
6000	74	225	41.64	273.6	-43.7
8000	74	225	44.9	256.1	-40.6
9000	74	225	63.1	201.6	-14.8

was varied in three experiments with a constant phase. In the next three, phase was varied with constant magnitude. The magnitude and phase were detected with good accuracy as seen from the relative error in magnitude detection.

When unbalances were detected from signals acquired from test bench, there were higher errors. The errors are lower for higher rotating speeds, due to larger centrifugal forces in higher speeds.

As it could be inferred from the theory presented in Section 5.1, this method is computationally intensive because a signal time interval of just 0.5 s has 1250 samples, assuming a sampling frequency of 2500 Hz. If according to modal expansion theory, the signals are expanded to the displacements of all DOFs, there are huge number of data points to be evaluated.

The matrices of equations of motion are handled multiple times. A small error gets multiplied and affect the results. So a high degree accuracy of model of the system is needed. Due to these drawbacks, the time domain method is not recommended and also not proceeded with in further course of the thesis.

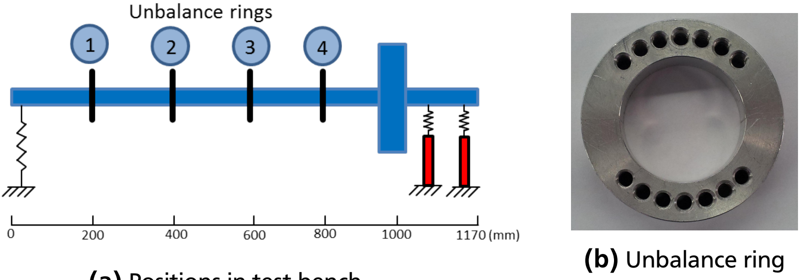

(a) Positions in test bench

(b) Unbalance ring

Figure 6.1: Unbalance rings

6.2 Fault detection in scaled rotor model in frequency domain

The rotor was driven in a series of five stationary operating points and they are assembled together to account for the quasi-static condition. For all the analyses, operating range between the first two resonances (133 Hz-200 Hz) is chosen. The operating range is restricted in the lower range due to low centrifugal forces out of added unbalances. The upper limit in the range is chosen due to loud noise when the second resonance is neared.

It has been assumed that the virtual signals from the piezos will correspond to the actual displacement. The displacement at the degrees of freedom of piezo actuator were taken as sensor signals. There are four positions where unbalances can be placed. These four positions are shown in Fig. 6.1 along with the actual ring. In all simulations, a test unbalance of 100 gmm was placed at 0°.

The simulations were carried out in three different conditions.

- Model compared with itself (assuming an ideal model).
- Outliers introduced in data, considered to be measured from real system.
- Method of M-estimators applied with data containing outliers.

To introduce outliers, errors are introduced in two of the five measured values. In one of them, the magnitude is reduced by 50% and angle distorted by 45°. In the other data point, the magnitude is increased by 100% and angle distorted by 135°.

Table 6.2: Detected unbalances from Test bench (simulation)

Unbalance Location Ring Nr.	Detected unbalance Magnitude (gmm)	Phase (deg)	Error Magnitude (rel) (%)	Phase (abs) (deg)
without any outlier				
1	98.1	0	-1.9	0
2	98.1	-0.1	-1.9	0
3	98.9	-0.1	-1.1	0
4	98.0	-0.2	-2.0	0
with outliers				
1	59.2	26.3	-40.8	26
2	58.0	28.2	-42.0	28
3	55.1	33.5	-44.9	33
4	81.8	6.9	-18.2	7
with robust estimators				
1	98.1	0	-1.9	0
2	98.1	0	-1.9	0
3	98.2	0	-1.8	0
4	98.3	0	-1.7	0

The results in all the three cases mentioned above are illustrated in Tab. 6.2. As it can be observed, an ideal model in the first case could identify the unbalances with negligible error. However when outliers are introduced, the error is considerably high. In both magnitude and phase, the error is significant in rings 1-3, which are farther from the actuator. However in the third case, the robust algorithm could detect the correct unbalances.

The relative residual plots are also compared for the three different cases in Fig. 6.2, where the three individual figures Fig. 6.2a-Fig. 6.2c correspond to the three cases as mentioned above. In all the three cases the unbalance in the fourth ring could be identified better than the others. It is due to its proximity to the sensor location. The unbalance could not be differentiated very well between rings 1 and 2 as observed from Fig. 6.2a, in all cases. Unbalance in ring 3 could only be identified correctly in the ideal case and when a robust estimator is used.

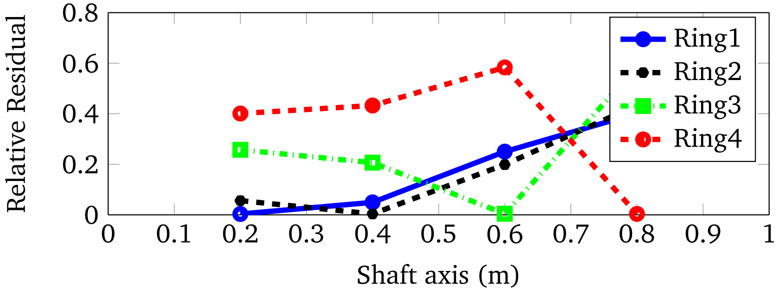

(a) Ideal model

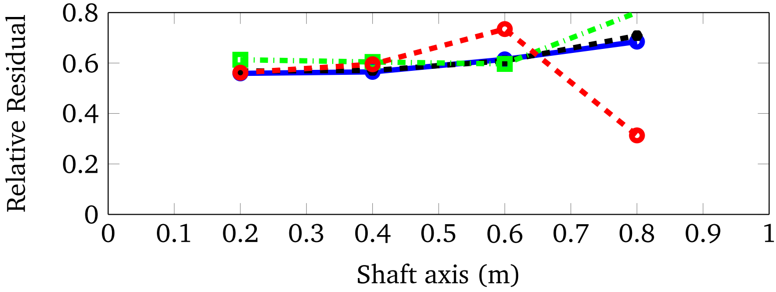

(b) with outliers

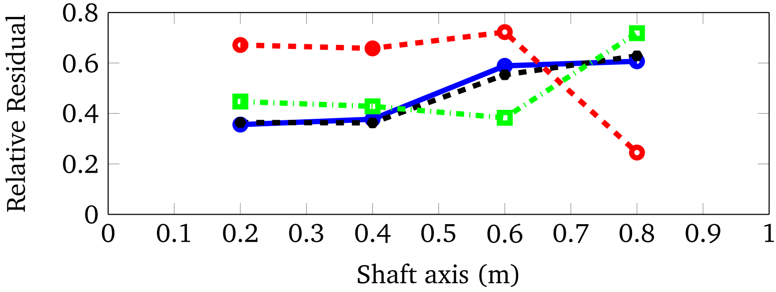

(c) with robust estimators

Figure 6.2: Relative residuals from simulations with test bench model

6.3 Fault detection using measured signals from test bench

Unbalance detection method was also tested on the available test bench. Unbalances of three different magnitudes 57 gmm, 74 gmm and 103 gmm are placed alternatively in each unbalance ring at different angular positions. They were mounted in subsequent tests, with all the test cases mentioned in Tab. 6.3.

A reference measurement was initially made after which test unbalances were screwed to the unbalance rings according to individual test cases. The measured sensor signals are subtracted from the respective reference signals at the corresponding operating points. Because the unbalance is sensitive to phases as well, it is necessary to measure the angular position of the shaft with the help of an encoder. The measured signals were processed before used for unbalance detection. They were windowed (rectangular window) whose sample length was 1250 samples or in other words 0.5 s in a sampling frequency of 2500 Hz. The windows always start at the sample where the encoder value is 0°.

There were test cases where the vibrations were too high to cross the first resonance at 109 Hz. In such cases, PPF controller presented in Section 4.4.1 was switched on, to damp the resonance peak and then turned off while acquiring the data after crossing the resonance.

Various tests were performed such as running at series of stationary operating points, quasi-static run, simultaneous actuation and sensing in a closed loop. The results of individual tests are presented below.

6.3.1 Analysis at stationary operating points

As a first test, the rotor was driven in five operating points in a stationary condition (8000 rpm-12 000 rpm in steps of 1000 rpm). Sensor signals were recorded at steady state conditions in each operating point for each of the test cases mentioned in Tab. 6.3. Unbalance detection was carried out by accumulating the sensor signals for all the operating points driven in a particular test case.

Because they are real measurements, no separate model disturbances or noise superposition or signal distortion were included. The results obtained

Table 6.3: Unbalance test cases

Case	Unbalance Ring	Magnitude (gmm)	Phase (deg)
1.	1	57	-45
2.	1	74	-45
3.	1	103	-45
4.	2	57	0
5.	2	74	0
6.	3	57	-45
7.	3	74	-45
8.	3	103	-45
9.	4	57	0
10.	4	74	0
11.	4	103	0

from weighted least squares method with robust estimators are presented in Tab. 6.4.

When the test cases with unbalance in first two rings are observed, the magnitude could be detected better only in three cases (cases 2,3,5) out of five. In these cases, the test unbalances are equal to or greater than 74 gmm. To explain this phenomenon the strain signals from real sensors in perpendicular directions are compared in Fig. 6.3a. Here signals recorded from case 5 is compared with those from cases 1 and 4, which could not detect the faults. The values show the relative deviation of the magnitudes in virtual sensors from the reference measurement. The relative deviation δ_z is calculated according to Eq. (6.1), where z and z_0 are the signals measured with and without the test unbalances respectively. The subtraction in the numerator is between two complex numbers, hence the value δ_z does not correspond to the magnitude deviation only.

$$\delta_z = \frac{|z - z_0|}{|z_0|} \tag{6.1}$$

It can be observed from the plot that the signals corresponding to case 5 is more distinguishable from reference than the signals in cases 1 and 4. This means that a test unbalance of magnitude 57 gmm could not create much forces in the test bench to make a better distinction in the measured signals.

Table 6.4: Unbalance identified from stationary operating points

Case	Test unbalance			Detected unbalance			Error	
	Ring	(gmm)	(deg)	Ring	(gmm)	(deg)	rel.(%)	abs.(deg)
1.	1	57	-45	3	17.2	41	-69	86
2.	1	74	-45	1	82.5	-136	11	-91
3.	1	103	-45	1	123.6	-2	20	43
4.	2	57	0	4	11.7	33.8	-79	34
5.	2	74	0	1,2	86.1	-9	16	-9
6.	3	57	-45	1,2	52.9	-13	-7	32
7.	3	74	-45	1,2	84.3	-34	13.5	11
8.	3	103	-45	1	89.3	-56	-13	-11
9.	4	57	0	4	311.9	-9	446	-9
10.	4	74	0	3,4	430.5	57.7	482	58
11.	4	103	0	3,4	341.4	82.2	231	82

Unbalances could also be detected with the method when placed in ring 3. The relative error in unbalance magnitude shows an acceptable detection. But when the actual detected values are seen, the influence of the highest unbalance seems less significant. This can also be observed from Fig. 6.3b where the relative deviation in magnitude of the strain is plotted for these three cases. Also in this figure the signals between case 7 and 8 could not be differentiated well.

The test unbalances in ring number 4 are not at all possible to detect. This could be explained with Fig. 6.4. The FRF of an impulse force in unbalance ring 4 to strain gauge is plotted in Fig. 6.4, along with its coherence. The model clearly shows an anti-resonance in this frequency region of interest. Though the measured FRF shows that the strain gauge records some signals, the coherence plot in the region 150-220 Hz, shows a very low correlation. This confirms the presence of an anti-resonance in the frequency region of interest. Due to this phenomenon, test cases with unbalances placed in ring 4 will not be presented or discussed in forthcoming sections.

Phases of unbalance could also be detected precisely only when higher unbalances were placed. The trend also follows for locating the faults, where only in cases of higher unbalances in rings 1 and 2 could be detected the locations precisely. As it was observed from simulations in the previous section also, the locations 1 and 2 could not be differentiated much.

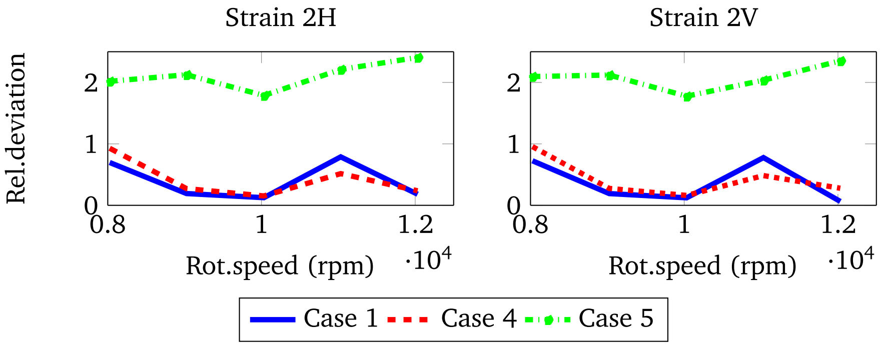

(a) Cases with weak signals compared with Case 5

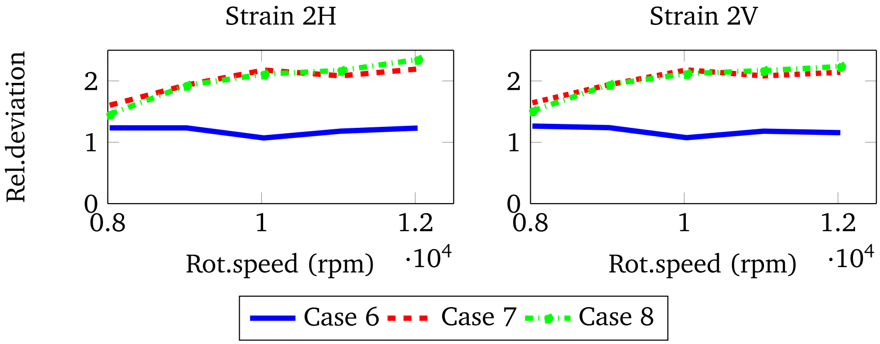

(b) Cases with unbalance in ring 3

Figure 6.3: Relative deviation in magnitude of strain signals

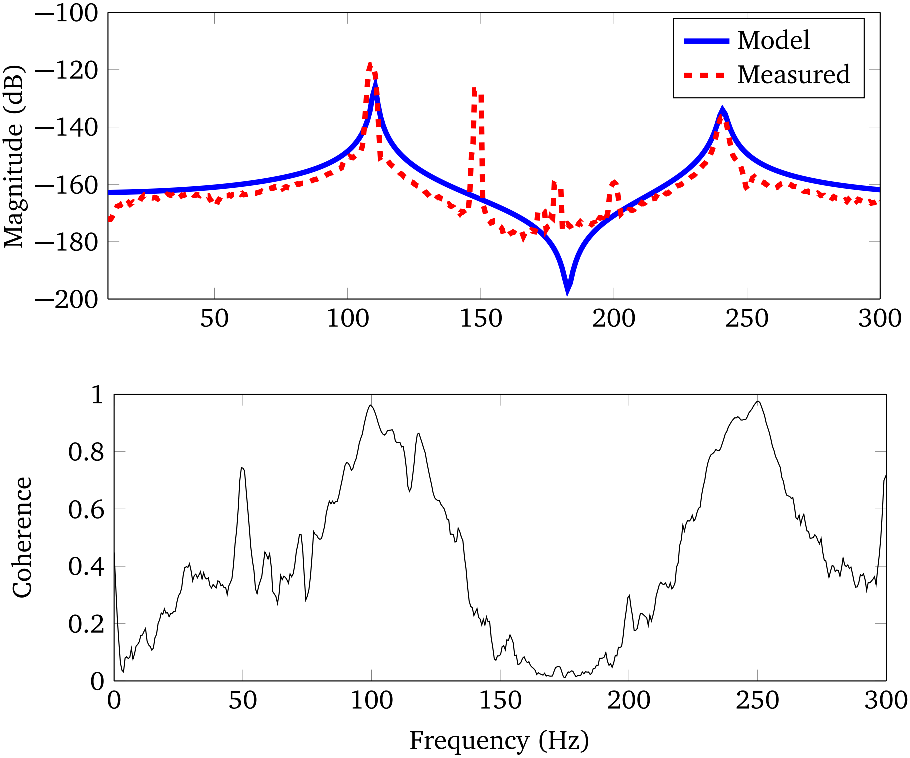

Figure 6.4: FRF and Coherence of Impulse in Ring 4 to Strain

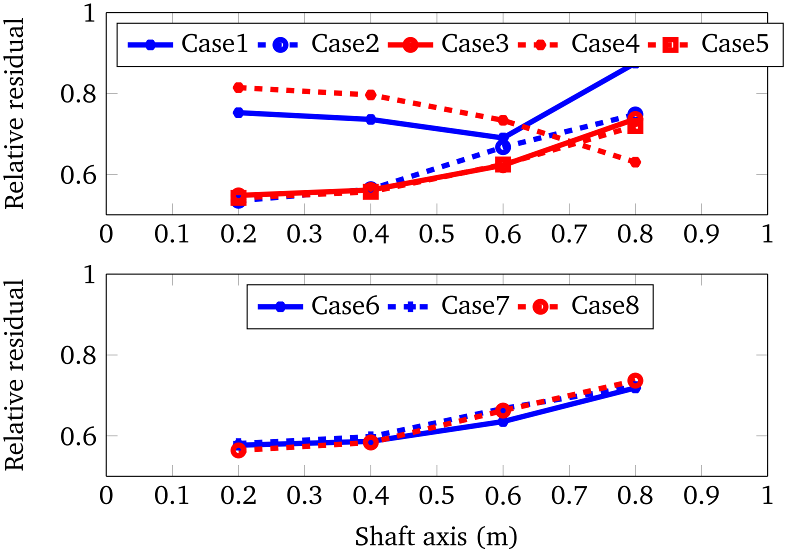

Figure 6.5: Relative residual with measurements from stationary points

The detailed relative residual plots are given in Fig. 6.5 based on which the predicted locations are also listed in the table.

6.3.2 Comparison of unbalance detection with other available sensors

In this section, the unbalance which was detected from strain signals from virtual sensors are compared to other available physical sensors in the test bench. The other sensors which are considered are

- Signals from real strain gauges and
- Force sensors collocated to the actuators

For better visualisation two tables are presented, one (Tab. 6.5) compares the unbalance magnitude detected from all sensors and their corresponding relative errors. The other table (Tab. 6.6) compares the phase detected from all sensors with their absolute errors. Because the unbalances in fourth ring could not be detected at all as discussed in the previous section, it is being neglected in further discussions.

Table 6.5: Comparison of unbalance magnitude identified from different sensors

			Virtual strain		Real strain		Force sensors	
Case	Position Ring Nr.	Unb. (gmm)	Unb. (gmm)	Error (%)	Unb. (gmm)	Error (%)	Unb. (gmm)	Error (%)
1.	1	57	17.2	-69	11.3	-80	9.8	-82
2.	1	74	82.5	11	86	16	81	9.3
3.	1	103	123.6	20	117.6	14	122.1	18.5
4.	2	57	11.7	-79	22.4	-61	21.9	-62
5.	2	74	86.1	16	71.6	-4	75.6	2
6.	3	57	52.9	-7	56.6	0	61.8	8.4
7.	3	74	84.3	13.5	87.9	17.6	96.2	29
8.	3	103	89.3	-13	92.4	-10	101.7	-1.3

Table 6.6: Comparison of unbalance phase identified from different sensors

			Virtual strain		Real strain		Force sensors	
Case	Position Ring Nr.	Unb. (deg)	Unb. (deg)	Error (deg)	Unb. (deg)	Error (deg)	Unb. (deg)	Error (deg)
1.	1	-45	41	86	36	81	67	112
2.	1	-45	-136	-91	-146	-101	-122	-77
3.	1	-45	-2	43	-28	17	-4	41
4.	2	0	34	34	76	76	114	114
5.	2	0	-9	-9	-18	-18	0	0
6.	3	-45	-13	32	-10	35	13	58
7.	3	-45	-34	11	-53	-8	-31	14
8.	3	-45	-56	-11	-68	-23	-44	-1

The following observations could be noted from Tab. 6.5 where the detected magnitude of unbalances are listed. The detected unbalance magnitude from virtual sensors coincide with real strain sensors and force sensors in most of the cases. In cases 7 and 8 the same trend (Fig. 6.3b) is observed in all the sensors as in the virtual sensor case described above. The signals between these two cases could not be differentiated much. This results in detection of unbalances which are close to each other though the test unbalances are not the same. The detected magnitudes from force sensors are smaller than those detected by the real strain gauges. However such a clear trend could not be observed between virtual and real sensor signals.

In this paragraph the observations from Tab. 6.6 are discussed regarding the unbalance phases. The phase detected due to virtual and real strain sensors do not coincide exactly. Only in case 4 the difference between the real and virtual sensors is unacceptable. Otherwise the difference between the phases detected out of these sensors is only 11° on an average. This indicates the ability of the virtual sensor to detect the unbalance phase as good as the real strain gauge.

When the phases detected by virtual sensors are compared to the force sensors, a similar trend is observed. Except for case 4, the phases detected by virtual strain sensor differ only by 12° from those detected by the force sensors.

6.3.3 Transient measurements

The rotor was run-up slowly with the same acceleration (22.5 rpm/s) as in a vibration survey of real aircraft engine test. Due to the slow acceleration, it can be considered as a quasi-static measurement. From the recorded data, signals within a time interval of 0.5 s near the five operating points of interest are extracted. They are then analysed together for fault detection in a transient case. The results are seen in Tab. 6.7. Unlike the previous experiment, only selected test unbalance cases are analysed for measuring the transient signals.

The unbalance magnitude could be found in the case of unbalance in rings 1 and 2 only, with acceptable error. The magnitudes detected with unbalance in ring 3 are smaller than the actual test unbalances. But the detected results show a positive trend as the test unbalance magnitude is increased. When the resulting values are compared to those detected in stationary case, the magnitudes do not match. Except for case 5, the unbalances detected are smaller

Table 6.7: Unbalance identified from operating points in transient run

Case	Test unbalance			Detected unbalance			Error	
	Ring	(gmm)	(deg)	Ring	(gmm)	(deg)	rel.(%)	abs.(deg)
2.	1	74	-45	1,2	69.4	70	-6	115
5.	2	74	0	1,2	92.1	161.2	24	161
6.	3	57	-45	1,2	18.3	-143	-67	-98
7.	3	74	-45	1,2	46.1	-118	-37	-73
8.	3	103	-45	1,2	63.6	-145	-38	-100

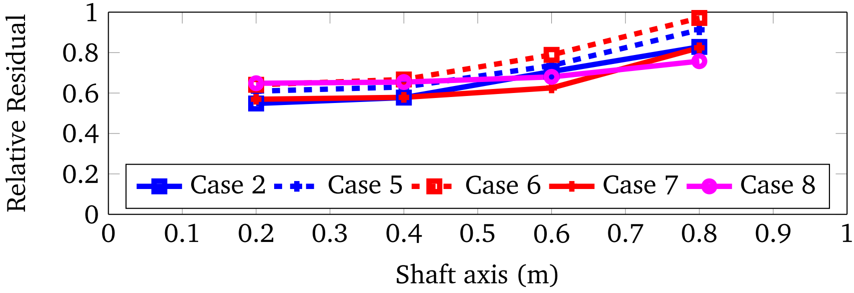

Figure 6.6: Relative residual with transient measurements

as observed from Tab. 6.4. This means that the transients cause a significant influence on the unbalance detection.

In the table, identified phase of unbalances show a drastic error, from which it can be said that the phase could not be found at all. The slowly accelerating rotor does not have an uniform time period of signals in the small window. A shortcoming of even half a time period will cause an error upto 180°. This should be overcome by reducing the window size so that effect of transients could be minimised. But this should be done at the expense of number of samples which will be collected for identifying the amplitude and phase.

The location of unbalances also could not be identified. This can be seen in Fig. 6.6. The reason is due to accumulated errors in magnitude and phase.

Table 6.8: Unbalance identified from simultaneous actuation and sensing

Case	Test unbalance			Detected unbalance			Error	
	Ring	(gmm)	(deg)	Ring	(gmm)	(deg)	rel.(%)	abs.(deg)
with virtual sensor								
2.	1	74	-45	1	30	-18	-59	27
5.	2	74	0	1,2	68	148	-8	148
7.	3	74	-45	1,2	72	52	-2	97
with real strain gauge								
2.	1	74	-45	3,4	32	29	-57	74
5.	2	74	0	1,2,3	92	76	24	76
7.	3	74	-45	1,2,3	96	5	30	50

6.3.4 Unbalance detection with simultaneous actuation

Measurements in test bench were conducted in closed loop with FxLMS algorithm. A brief introduction about the algorithm is given in Appendix B. The adaptive algorithm uses the virtual displacement as the sensor signal and minimizes it. In the present case, the chosen operating points were 8000 rpm and 10 000 rpm only. The secondary path model for the algorithm is constructed by sine sweep excitations at the same operating points where the tests were made. At each point the parameters μ and α of the algorithm were tuned experimentally by trial and error. Only three test cases were investigated, in which unbalance with magnitude 74 gmm was screwed at the four different unbalance rings to measure the vibration signals due to unbalance. A reference measurement was also done at the operating points to record the vibration without the unbalance fault.

According to the theory explained in Section 5.3, unbalances were determined with the help of least squares method and they are listed in Tab. 6.8. Because there are only two operating points available, the robust estimation method using M-estimators could not be used here.

The unbalance detected from this case are presented in Tab. 6.8. Except for case 2, the magnitude could be detected better. In all these cases, the vibrations are compensated by the voltages of piezoelectric actuators, and hence the virtual sensors could record bare minimum vibration. Since the unbalances are

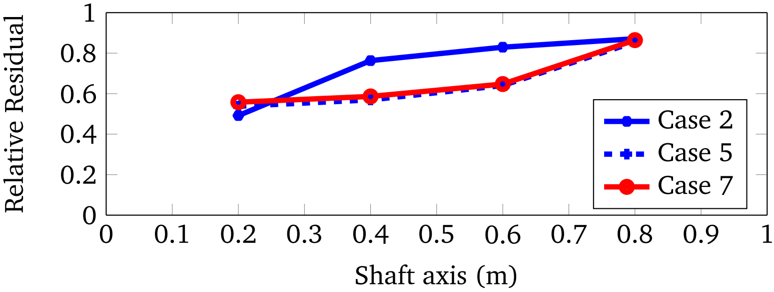

Figure 6.7: Relative residual with simultaneous actuation and sensing

detected from actuation force predominantly, the magnitude could be detected better.

Phase could not be detected because the measured voltage signals are not subjected to the high pass filter, through which the displacement signals are reconstructed. Hence there is a phase mismatch between the reconstructed signal and actuation voltage. Hence phase should be compensated for a better detection.

To validate the effectiveness of this new method, signals from real strain gauge was used for fault detection. Table 6.8 shows that unbalance could be detected both from real and virtual sensor. Except for case 2, the unbalances could be detected from both the sensors in active and their corresponding passive case which was presented in Tab. 6.5, though the accuracy is different. Here the phase could not be reproduced exactly but its difference is consistent across the cases.

The values of relative residuals are plotted in Fig. 6.7. As it is shown in the plot and also from Tab. 6.8, the unbalances could not be assigned a distinct position in a closed control loop.

6.4 Fault diagnosis in aircraft engine model

In this section, the Whole Engine Model (WEM) which was presented in Section 3.5.1 is analysed. In this rotor system there are ten stages of compressor and two stages of turbine blades where unbalances could show up. One of the possible ways is when the blades come in contact with static parts and gets eroded. This loss of mass due to erosion is also a case of unbalance where material is removed from a balanced system.

In real test environment of an aircraft engine, a quasi-static run is used for vibration surveys with an aim to obtain the vibration responses at all rotational frequencies. A quasi-static condition is a transient run from idle state to maximum take-off speed in a longer time frame. In the engine being investigated, this acceleration corresponds 22.5 rpm/s. The analysis in this thesis is also performed in the same quasi-static acceleration of the engine. Due to this slow acceleration, the rotor can be assumed as stationary in a small time interval of 1 s. The speed interval within this 1 s corresponds to 0.16% of the maximum take-off speed, and hence the stationary speed assumption can be justified. Therefore in this investigation several stationary runs are superposed to represent the transient simulation. The vibration response at four different speeds in frequency domain are collected together.

In all cases, an unbalance of magnitude 1000 gmm is placed in different compressor stages one after the other. Since it is a simulation study, it is being attempted if unbalance can be located with the help of scalar relative residual in each case than determining its magnitude and phase. It is assumed that the piezoelectric actuator is able to reconstruct its displacement. Hence displacement obtained from the WEM at that DOF is assumed to be that of self-sensing piezo actuator.

Due to the simulative nature of this work, where the responses from WEM is compared to that of the same model, a band-limited white noise (of noise power 1% relative to the power of the signal) is superimposed to the signals to simulate the noise from a real measurement. Out of the displacements measured at four stationary points, two are corrupted manually to account for measurement errors and model mismatch. One of them is reduced by 25% in magnitude and phase shifted by 22° and the other displacement is magnified by 10% and phase shifted by 135°. They represent the outliers for the optimisation problem. Later with the theory of M-estimators, unbalances are detected again in the presence of this error and measurement noise. On the whole, the three actuator positions are analysed for three separate cases.

For better visualisation, the results presented in this section contain only unbalances placed in three compressor stages (namely stages 3, 6 and 10). Because the centre of gravity of the HP rotor is at compressor stage 6, these selected

Table 6.9: Detected unbalances from WEM (Active bearing - Piezo and SFD in series)

Unbalance Location Stage Nr.	Detected unbalance Magnitude (gmm)	Phase (deg)	Error Magnitude (rel) (%)	Phase (abs) (deg)
without any outlier				
3	972.1	0.06	-2.69	0
6	973.4	-0.6	-2.66	-0.6
10	971.9	-0.5	-2.81	-0.5
with outliers				
3	748.0	9.0	-24.2	9
6	722.5	9.8	-27.7	10
10	690.8	11.5	-31	11
with robust estimators				
3	970.2	0.18	-3	0
6	971.8	-0.08	-2.8	0
10	969.7	0.03	-3	0

stages represent locations before, at and after the centre of gravity respectively. The complete results with unbalances in all ten compressor stages are presented in Appendix C.

6.4.1 Active bearing in aircraft HP rotor

In this section, unbalances were detected in two different active bearing concepts which was presented in Section 3.5.2.

Piezo actuator in series with SFD

Concise list of results is presented in Tab. 6.9, where the unbalances were placed at one compressor stage per experiment. The ability of the model-based method to detect it has been examined. It can be observed that magnitude and phase could be detected very well. However when the disturbances are included in the measured signals, the unbalances could not be detected with acceptable accuracy, as the error in magnitude is more than 25% and phase could be detected only with a deflection. This shows the need for an accurate model for unbalance detection. Observing the detailed unbalance detection results from Tab. C.2, the unbalance when closer to the bearing position could be detected better. However the location of unbalances could not be determined at all, when the values of relative residuals are observed.

The relative residual plot from a transient run with the piezo actuators in a active bearing with series in SFD is presented in Fig. 6.8. The three separate plots correspond to the three different cases as listed in Tab. 6.9. Each curve denote the values of scalar relative residual when the test unbalance is placed at a known position in the simulation. For example the red dashed line with square markers in Fig. 6.8a shows the case when test unbalance is placed at compressor stage 6. The individual points in the line shows the relative residuals when the unbalance is calculated assuming a particular stage.

In Fig. 6.8a the points where the relative residuals are minimum coincides with the positions where the test unbalances are placed. This applies to all the three stages. However when the measurements are disturbed, a line does not point to a distinct minimum (Fig. 6.8b). This can be improved with the robust estimators as seen in Fig. 6.8c. The lines show that the relative residual can exactly find out where the unbalances are located. The complete picture can be observed from Fig. C.1 which shows the relative residuals for test unbalances at all the compressor stages.

Piezos and SFD in parallel

In the case of active bearings when Piezos and SFD are in parallel, an unbalance of 1000 gmm was placed at 100° at each compressor stage similar to the previous analysis. The concise results from this case are presented in Tab. 6.10 and detailed results in Tab. C.4-C.6. As it is seen, the simulation could detect the unbalance with good accuracy. However when the outliers are introduced, the results are not accurate as reflected in the values of error. The method of M-estimators is useful, because the errors could be reduced considerably.

The relative residuals for the analysis in this case are plotted in Fig. 6.9. Also in this case, the unbalances could be detected better only with the help of robust estimators. Detailed plots are presented in Fig. C.2.

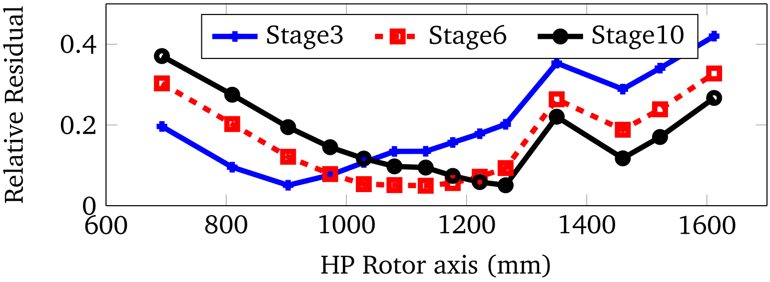

(a) without any outlier

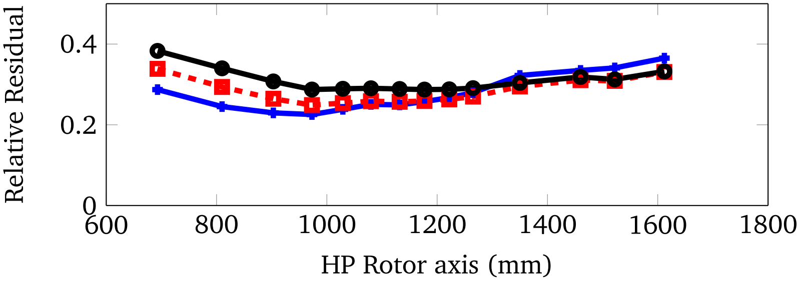

(b) with outliers

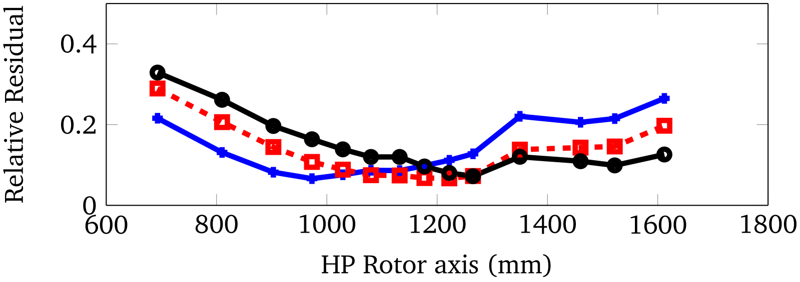

(c) with robust estimators

Figure 6.8: Relative residual plot from quasi-static run in active bearings (Piezos and SFD in series)

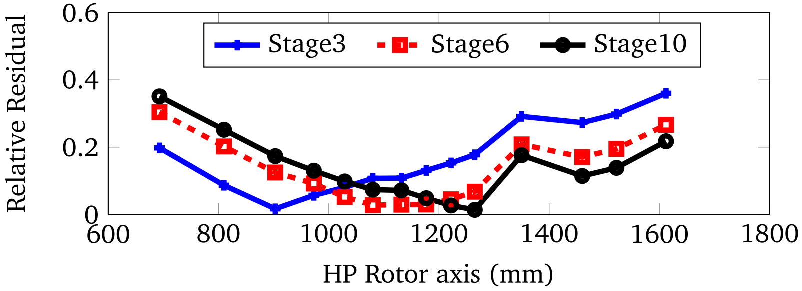

(a) without any outlier

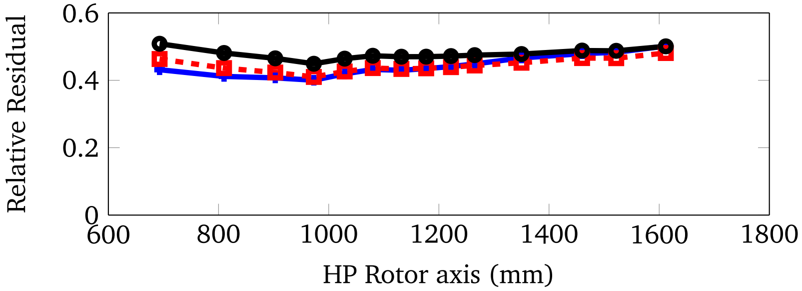

(b) with outliers

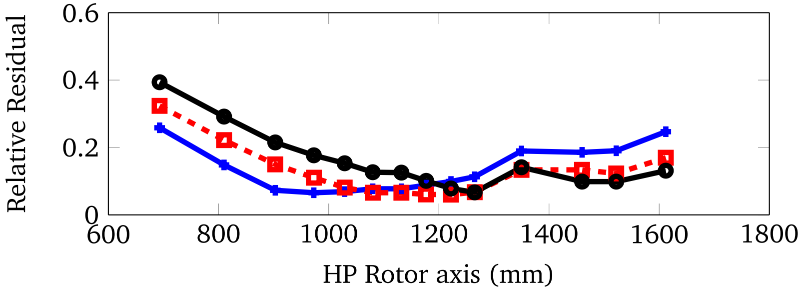

(c) with robust estimators

Figure 6.9: Relative residual plot from quasi-static run in active bearings (Piezos and SFD in parallel)

Table 6.10: Detected unbalances from WEM (Active bearing - Piezo and SFD in parallel)

Unbalance Location Stage Nr.	Detected unbalance Magnitude (gmm)	Phase (deg)	Error Magnitude (rel) (%)	Phase (abs) (deg)
without any outlier				
3	984.3	100.3	-1.6	0.3
6	974.6	99.8	-2.6	-0.2
10	975.5	99.8	-2.5	-0.2
with outliers				
3	580.9	119.7	-42	19.7
6	556.6	122.4	-43.4	22.4
10	512.5	125.7	-48.8	25.7
with robust estimators				
3	958.9	100.6	-4.2	0.6
6	975.6	100.5	-2.5	0.5
10	967.5	100.6	-3.3	0.6

6.4.2 Active internal suspension of aircraft engine

With respect to active internal suspension, four actuators are placed as mentioned in Section 3.5.2. In this analysis the unbalance of magnitude 1000 gmm are placed at 120° in the stages. The four actuators are investigated in three different perspectives for fault diagnosis as listed below.

- All four actuators in internal suspension configuration
- Only the (front) actuators near the bearing
- One actuator in front and one in rear side

In the first perspective, all the actuators in front side and rear side are considered. The displacement at those degrees of freedom are used to detect the fault and its location. The results from selected compressor stages are presented in Tab. 6.11. From Fig. 6.10, it can be seen that relative residual does not show a minimum. This means that actuators which are at active internal suspension are unable to locate the faults. The reason is because these actuators are not in proximity of the high pressure rotor, where the unbalance source is present.

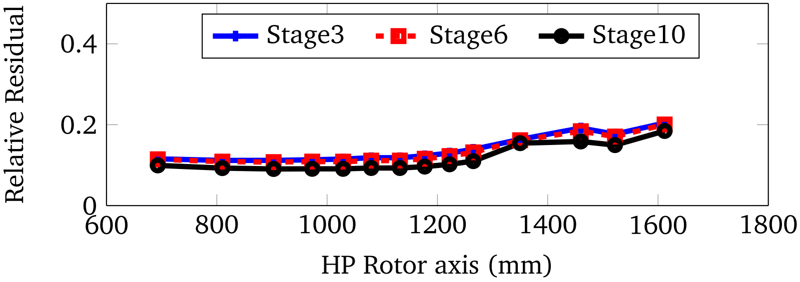

(a) without any outlier

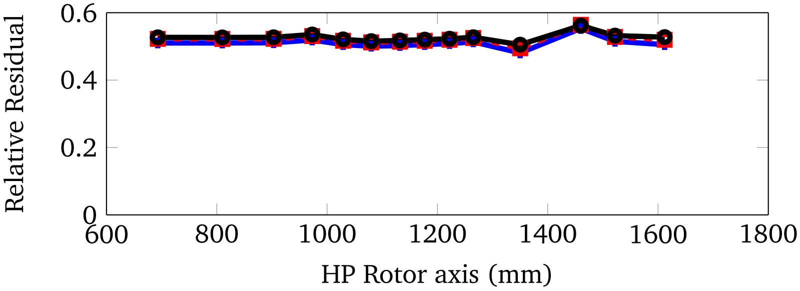

(b) with outliers

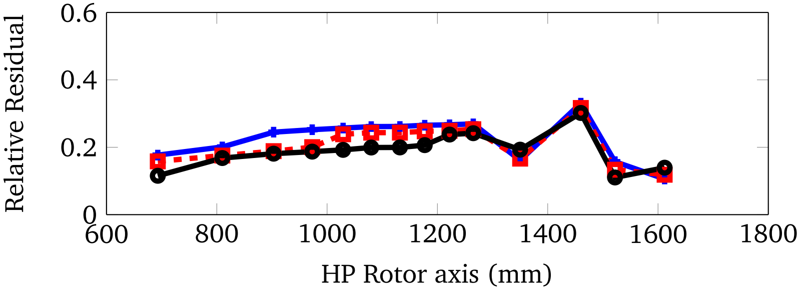

(c) with robust estimators

Figure 6.10: Relative residual plot from quasi-static run in active internal suspension when all four actuators are considered

The plots in Fig. C.3 also show the same trend with test unbalances placed at all compressor stages. The exact values of the magnitude and phases are given in Tab. C.7-Tab. C.9.

Table 6.11: Detected unbalances from WEM (Active internal suspension - All four actuators)

Unbalance Location Stage Nr.	Detected unbalance Magnitude (gmm)	Phase (deg)	Error Magnitude (rel) (%)	Phase (abs) (deg)
without any outlier				
3	977.8	120	-2.3	0
6	977.8	120	-2.3	0
10	978.5	119.9	-2.2	-0.1
with outliers				
3	469.7	158.8	-53.1	38.8
6	468.5	159.8	-53.2	39.8
10	453.1	163.9	-54.7	43.9
with robust estimators				
3	737.3	141.3	-26.3	21.3
6	738.5	141.0	-26.1	21.0
10	740.9	140.5	-26.0	20.5

In Fig. 6.11, the relative residuals of the other two cases mentioned above are presented. For reasons of brevity, only the relative residuals obtained through robust optimisation has been presented. When the individual plots are observed, only in Fig. 6.11a the relative residuals approach a minimum in the respective stages. But the unbalance locations could not be differentiated very well (seen from values in ordinate). These are the actuators at the front part of internal suspension. In case of one forward and a rear actuator in Fig. 6.11b, values of relative residuals are the same in all the ten compressor stages. Also with this configuration, the location could not be identified.

But as observed from Tab. 6.12, the magnitude and phase of the unbalances could be detected with the help of robust estimation.

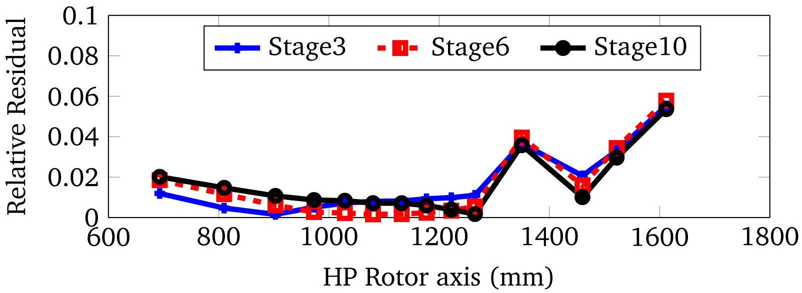

(a) Only actuators near bearings

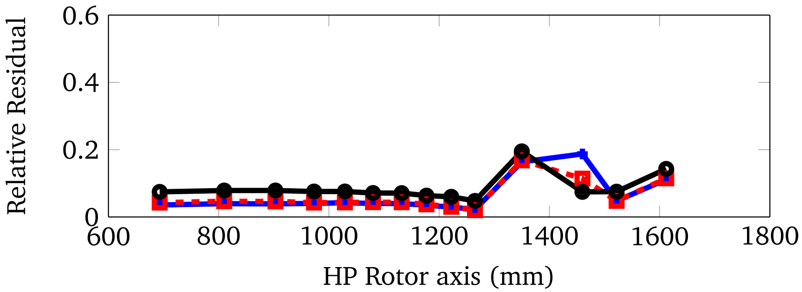

(b) One forward and one rear sensor

Figure 6.11: Relative residual - Active Internal suspension special cases

Table 6.12: Detected unbalances from WEM using robust estimators (Active internal suspension)

Unbalance Location Stage Nr.	Detected unbalance Magnitude (gmm)	Phase (deg)	Error Magnitude (rel) (%)	Phase (abs) (deg)
Front actuators				
3	973.0	119.9	-2.7	0
6	973.3	119.9	-2.7	0
10	973.8	119.9	-2.7	9
1-Front and 1-rear actuator				
3	973.3	120.3	-2.6	0
6	966.5	120.0	-3.3	0
10	963.9	120.5	-3.7	0

6.5 Discussion

Important observations from fault detection in both the rotor systems are presented in this section.

6.5.1 Observations from fault diagnosis in test bench

The time domain fault diagnosis method is computationally expensive method. The information of the model is used multiple times within the same execution which magnifies the error in the model. Hence the frequency domain method using parameter estimation techniques was preferred in this thesis.

The bearing displacements are used for fault detection. The least squares method could detect unbalance faults with respect to their magnitude, phase and location very good. However when real measured data was analysed, the WLS method is used which is more robust against outliers in the data. Three different experiments were carried out. The first is at stationary operating points between the first two resonances. The second is a transient measurement at a specified acceleration. The third experiment in closed loop measurement with simultaneous actuation and sensing.

In the stationary experiments, 11 cases of test unbalances were examined. It was observed that a relative deviation of at least one unit is necessary between the balanced and unbalanced signals for a detection to be possible. This condition was matched by all the test cases except for two. These two cases correspond to low test masses at rings farther from the active bearing. Unbalances in ring 4 could not be detected due to the presence of an anti-resonance at the operating range of this experiment. Because the unbalance from the estimation method is determined as a complex number, the same condition applies to detect the phase also. The detected unbalances from other sensors also yielded comparable results, thus proving the ability of piezoelectric actuator to be used as a sensor.

For transient analysis five test cases were selected. The detected magnitudes are lesser than those detected in stationary experiments, though the relative errors are acceptable. This is due to the effect of transients affecting the signals. Detecting phase is difficult in this case as the transient sinus signals from sensors are only approximately useful in determining the phase. The accumulated error in detecting magnitude and phase reflects on location identification also, which makes it ambiguous.

Another important contribution of this thesis is the unbalance detection with an adaptive control algorithm in closed loop. This method which is extended from the existing parameter estimation method uses both the actuation voltage and reconstructed signals for fault detection. Though magnitude of unbalances could be determined, the phases need to be compensated for a mismatch due to filtering. This extended method was also validated with real strain gauges. The unbalances could also be detected from them similar to the virtual sensors. Hence the virtual sensors are capable of detecting unbalances in passive case and in a closed control loop.

6.5.2 Observations from fault diagnosis in WEM

In the HP rotor of the WEM, unbalances arising from one of its compressor stages is diagnosed. Mainly two actuator placement positions are analysed. The actuators at the bearings of the HP rotor is the first position. Out of two different configurations theoretically investigated, both are able to diagnose unbalance faults. The diagnosis method needs a robust estimator such as WLS analysed in this thesis. Only due to them a better detection of unbalance magnitude and phase could be possible.

The second actuator position which was examined is the active internal suspension. Because the actuators are not near the source of vibrations, this constellation of actuators could not locate the unbalances. The four actuators employed in this configuration could not locate the unbalance precisely. Two special cases were formulated and analysed separately. The first case considered only two actuators near the HP rotor bearing. The second case considered one actuator in the front and one at the rear. Though the former case could locate the unbalance, it is very insignificant.

An interesting phenomenon could be observed in the active internal suspension configuration. Though there is more information available when signals from four actuators are measured, results from them are not better than with less actuators. This could be observed from Tab. 6.11 and Tab. 6.12. The reason is due to positioning of the actuators in the rear links (Fig. 3.20b). The vibration is transmitted radially from the HP rotor towards the casing. But the rear links are not arranged radially when compared with the front links (Fig. 3.20a). Also the plane of the rear links is away from the HP rotor. Due to these reasons, the actuators mounted in rear links worsen the estimation of unbalance.

Hence it can be concluded that only actuators if placed in the active bearing could diagnose unbalances. From a fault diagnosis perspective both the concepts namely actuators in parallel or in series with SFD could be implemented.

6.5.3 Final remarks

There is however a difference between the experiments carried out in WEM and the scaled rotor test bench. In WEM the unbalances were added at different compressor stages. Each individual compressor stage is comparable to each other in terms of mass and stiffness. They are also more or less symmetrically distributed along the length of the HP rotor.

But in the scaled rotor test bench this is not the case. The individual balancing rings are situated in the same rotor shaft with a turbine dummy. The mass and stiffness of the rotating disc are higher than those of the rings. Hence only test unbalances in balancing rings away from the disc could be detected. This is also evident from the values of relative residuals which indicate the presence of faults in the first two rings only. When the method would be transferred to the real aircraft engine, this problem would already get addressed.

On the other hand, measurements in real test bench were performed considering the temperature of the actuator as well. The experiments were only done when the temperature of the actuator was less than 35 °C. The intention behind it is to avoid any temperature dependent non-linearities affecting the fault detection. However this is very significant in real aircraft engine. Though its location would be away from the hot gases from the combustion chamber, the model should be extended to include these effects.

7 Conclusion and Outlook

The main objective of this thesis is to use self-sensing piezoelectric actuators for a model based fault diagnosis problem in rotor systems. In order to achieve this, the problem has been broken down into modules. The individual modules are presented in this chapter and the complete picture described. In the end, indicators towards future works are presented.

7.1 Summary of the thesis

Two rotor systems were investigated in this thesis, one is an aircraft engine and other a simple rotor test bench. A finite element model of the former was developed by its manufacturer in which piezoelectric actuators were included as spring elements. The FE model of test bench has been improved from previous works with the help of grey-box modelling techniques. Frequency response function from real test bench was obtained by chirp excitations from piezoelectric actuators. The tuned model was validated with measurements from impulse hammer excitation, as they better represent the transmission of forces at the unbalance rings to all the sensors available in the test bench.

There are four piezoelectric actuators in the test bench, to actively control vibration arising out of unbalance excitation. Self-sensing techniques were applied to reconstruct the displacement in two of the actuators. Here the electrical signals of the actuators such as voltage and current are used to derive the mechanical displacement. The reconstruction is achieved in a two step process. For capacitance identification, anti-resonance frequencies were identified from the frequency response function. The ability of the actuator to act as a sensor was proven in both at a stationary operating point in time-domain and across the operating frequency range in frequency domain. The reconstructed displacement signals are used in closed loop with a PPF controller. This controller could reduce the resonance peak by approximately 33%. The actuation voltage needed was only 30-40 V, which is well within the linear range of actuator operation. At a point away from the resonance, the reconstructed signals were used in closed loop with an adaptive algorithm. This proves the effectiveness of actuators in simultaneous actuation and sensing.

Faults in the rotor system were diagnosed in frequency domain using parameter estimation techniques. As a precursor towards future works, only unbalance fault was investigated. Least squares approach was used to detect the magnitude and faults of unbalance, which inturn uses an L_2 norm to find an optimal value. Robustness of LS approach was improved by Weighted least squares (WLS), with weights derived from method of M-estimators. To identify the location of faults, a scalar relative residual was calculated. The algorithm has been extended to be used in a closed control loop by including the actuation force due to actuator voltage.

Initially simulations were performed with the model of rotor test bench. The problem of outliers in signals were effectively handled with WLS. Unbalance magnitude, phase and location could be identified with the help of weighted least squares better. The same was identified with the help of measured signals from test bench. The identified results from reconstructed displacement signals due to self-sensing are compared against those measured from real strain gauges and a good agreement can be seen. Apart from stationary speeds, the ability to diagnose faults in a transient condition was shown. As a final and important step, fault was detected under simultaneous actuation and sensing in a closed loop. In these last two experiments, only unbalance magnitude could be determined.

Fault diagnosis was also carried out using model of high pressure rotor of an aircraft engine. It has been assumed that mechanical displacement could be extracted from piezos mounted at three different locations. In simulations, outliers were introduced into the data and performance evaluated. Unbalance magnitude, phase and location could be detected only in those locations when the actuators are placed in the bearings, because they are closer to the rotor.

7.2 Inference

It can be concluded from this thesis that bearing displacement signals could be used in estimation of faults. These displacement signals could be reconstructed from electrical signals of the piezoelectric actuator at the bearings. For the detection to be possible, a relative deviation of sensor signals of value one unit is a threshold. Mass in the test bench is asymmetrically distributed due to the rotating disc at a farther end. Because of this unbalances only away from it could be detected. However in a real HP rotor of an aircraft engine, the mass is symmetrically distributed in its shaft and faults could be detected in all the stages.

The virtual sensors due to reconstruction in piezoelectric actuators indicate a good potential to replace the real sensors. Though not in its present form, unbalances could be detected also from virtual sensors in a closed loop with simultaneous actuation of piezoelectric actuators.

7.3 Future works

In a nutshell it can be said that this research work has taken on the unbalance detection problem using conventional detection methods using a newly developed virtual sensor. In future, there could be works to investigate the relevance of this sensor in detecting other faults. Apart from rotation synchronous vibrations, faults such as misalignment, gear defects create super-synchronous vibrations. However their analysis with available test bench needs some constructional modification. Considering the weight of the rotating components, shaft cracks could make experimental investigations dangerous. Nevertheless bearing faults are relatively easier to be realised.

Before the multiples of synchronous speed vibrations could be analysed, there is a need to develop virtual sensor. With reference to Fig.4.10, the high pass filter restricts the operating range between 50-230 Hz. A third possible extension is to include temperature dependent effects of the actuator into the system model.

Bibliography

[1] J. Vance, F. Zeidan, and B. Murphy, *Machinery Vibration and Rotordynamics*. John Wiley & Sons Inc., 2010.

[2] A. Preumont, *Vibration Control of Active Structures- An Introduction*, 3rd ed. Springer, 2011.

[3] *Mechanical vibration - Rotor balancing - Part 14: Procedures for assessing balance errors*, International Standards Organisation Std. ISO 21 940-14:2012.

[4] F. Lebo, "Theoretische und experimentelle Analysen von Flugtriebwerksrotoren zur aktiven Schwingungsminderung mit Piezostapelaktoren," Ph.D. dissertation, Technische Universität Darmstadt, 2011.

[5] S. Ding, *Model-based Fault diagnosis techniques- Design schemes, Algorithms and tools*. Springer, 2008.

[6] R. Isermann, "Model-based fault-detection and diagnosis - status and applications," *Annual Reviews in Control*, vol. 29, pp. 71–85, 2005.

[7] Z. Wang, R. S. Schittenhelm, and S. Rinderknecht, "Observer design for unbalance excited rotor systems with gyroscopic effect," in *Proceedings of 2012 IEEE International Conference on Mechatronics and Automation*, August 5-8 2012, pp. 7–12.

[8] R. Ambur, Z. Wang, R. S. Schittenhelm, and S. Rinderknecht, "Model-based fault detection on a non-linear rotor system," in *Proceedings of the 9th IFToMM International Conference on Rotor Dynamics*, 2015.

[9] M. Witczak, *Modelling and Estimation strategies for Fault Diagnosis of Non-Linear Systems. From Analytical to Soft Computing Approaches. Lecture Notes in Control and Information Sciences*. Springer Verlag, 2007.

[10] R. Walker, S. Perinpanayagam, and I. K. Jennions, "Rotordynamic faults: Recent advances in diagnosis and prognosis," *International Journal of Rotating Machinery*, vol. 2013, pp. 1–12, 2013.

[11] J. M. Corres, J. Bravo, and F. J. Arregui, "Unbalance and harmonics detection in induction motors using an optical fiber sensor," *IEEE Sensors Journal*, vol. 6, no. 3, pp. 605–612, 2006.

[12] Q. Han, Z. Zhang, and B. Wen, “Periodic motions of a dual-disc rotor system with rub-impact at fixed limiter,” *Proceedings of the Institution of Mechanical Engineers, Part C: Journal of Mechanical Engineering Science*, vol. 222, no. 10, pp. 1935–1946, 2008.

[13] S. Ganeriwala, B. Schwarz, and M. H. Richardson, “Operating deflection shapes detect unbalance in rotating equipment,” *Journal of Sound and Vibration*, vol. 43, no. 5, pp. 11–13, 2009.

[14] R. Ambur, R. S. Vadamalu, and S. Rinderknecht, “Identification of unbalance faults in rotors with unknown input observers using classical and LMI based approaches,” in *European Control Conference 2016*, 2016.

[15] H. Wang, J. Wang, and J. Lam, “Robust fault detection observer design: Iterative LMI approaches,” *Journal of Dynamic Systems, Measurement and Control*, vol. 129, no. 1, pp. 77–82, 2007.

[16] Z. Wang, A. Wahrburg, and S. Rinderknecht, “Consideration of gyroscopic effect in fault detection and isolation for unbalance excited rotor systems,” *International Journal of Rotating Machinery*, vol. 2012, pp. 1–14, 2012.

[17] C. Zang, A. W. Lees, and M. I. Friswell, *Multi plane balancing of a rotating machine using a single transducer*, 2002, pp. 130 – 136.

[18] R. Markert, R. Platz, and M. Seidler, “Model based fault identification in rotor systems by least squares fitting,” *International Journal of Rotating Machinery*, vol. 7, no. 5, pp. 311–321, 2001.

[19] R. Platz, “Untersuchungen zur modellgestützten Diagnose von Unwuchten und Wellenrissen in Rotorsystemen,” Ph.D. dissertation, Technische Universität Darmstadt, Düsseldorf, 2004.

[20] G. N. D. S. Sudhakar and A. S. Sekhar, “Identification of unbalance in a rotor bearing system,” *Journal of Sound and Vibration*, vol. 330, no. 10, pp. 2299–2313, 2011.

[21] N. Bachschmid, P. Pennacchi, and A. Vania, “Identification of multiple faults in rotor systems,” *Journal of Sound and Vibration*, vol. 254, no. 2, pp. 327 – 366, 2002.

[22] N. Bachschmid, P. Pennacchi, A. Vania, G. Zanetta, and L. Gregori, “Case studies of fault identification in power plant large rotating machinery,” in *Proceedings of the IFToMM-6th International Conference on Rotor Dynamics*, 2002, pp. 191–200.

[23] A. Lees, J. K. Sinha, and M. I. Friswell, “Model-based identification of rotating machines,” *Mechanical Systems and Signal Processing*, vol. 23, no. 6, pp. 1884 – 1893, 2009.

[24] S. Hawibowo, “Sicherheitstechnische abschätzung des betriebszustandes von pumpen zur schadensfrüherkennung,” Ph.D. dissertation, Technische Universität Berlin, 1997.

[25] M. Atalla and D. Inman, “On model updating using neural networks,” *Mechanical Systems and Signal Processing*, vol. 12, no. 1, pp. 135 – 161, 1998.

[26] J. Mottershead and M. Friswell, “Model updating in structural dynamics: A survey,” *Journal of Sound and Vibration*, vol. 167, no. 2, pp. 347 – 375, 1993.

[27] A. Younan and A. El-Shafei, “Model calibration of anisotropic rotordynamic systems with speed-dependent parameters,” *Journal of Engineering for Gas Turbines and Power*, vol. 130, 2008.

[28] T. Marwala, *Finite-element-model Updating Using Computational Intelligence Techniques, Applications to Structural Dynamics*. Springer London, 2010.

[29] D. Ewins, *Modal Testing: Theory and Practice*. Brüel & Kjær, 1986.

[30] H. Irretier, “Mathematical foundations of experimental modal analysis in rotor dynamics,” *Mechanical Systems and Signal Processing*, vol. 13, no. 2, pp. 183 – 191, 1999.

[31] M. Aenis, “Einsatz aktiver Magnetlager zur modellbasierten Fehlerdiagnose in einer Kreiselpumpe,” Ph.D. dissertation, Technische Universität Darmstadt, Darmstadt, 2002.

[32] N. Butzek, “Modellbasierte Verfahren zur online Fehlerdiagnose an einer Kreiselpumpe in aktiven Magnetlagern,” Ph.D. dissertation, Technische Universität Darmstadt, 2009.

[33] B. Hasch, “Modellbasierte Fehlererkennung an einem elastischen Rotor mit Hilfe aktiver Lagerung,” Ph.D. dissertation, Technische Universität Darmstadt, 2010.

[34] Z. Wang, “Robuste modellbasierte Fehlerdiagnose an elastischen Rotoren unter Berücksichtigung der Gyroskopie,” Ph.D. dissertation, Technische Universität Darmstadt, 2013.

[35] K. Mühlenfeld, A. Rienäcker, C. Streller, and L. Padva, “Vibration reduction in aero-engine- a case study,” in *Schwingungen in Rotierenden Maschinen*, 2001, pp. 261–268.

[36] J. M. Barragán, “Engine vibration monitoring and diagnosis based on on-board captured data,” in *RTO AVT Symposium on "Ageing Mechanisms and Control: Part B- Monitoring and Management of Gas Turbine Fleets for Extended Life and Reduced Costs"*, 2001.

[37] B. Domes, “Vibration phenomena in aero-engines,” in *9th Internation Conference on Vibrations in Rotating Machinery IMechE*, 2008.

[38] G. P. Whiteford and P. T. Herbst, “Vibration isolation system including a passive tuned vibration absorber,” USA Patent US5 687 948, November 18, 1997.

[39] A. El-Shafei, “Unbalance response of a jeffcott rotor incorporating long squeeze film dampers,” *ASME Journal of Vibration and Acoustics*, vol. 113, pp. 85–94, 1991.

[40] A. El-Shafei, “Experimental and analytical investigation of hybrid squeeze film dampers,” *ASME Journal of Eng Gas Turbines Power*, vol. 115, no. 2, pp. 353–359, 1993.

[41] D. Hodgson and T. Duclos, “Mount with adjustable length inertia track,” USA Patent 4 969 632, November 13, 2000.

[42] M. H. Taha, “Power electronics application for more electric aircraft,” *Recent Advances in Aircraft Technology*, vol. 14, pp. 289–308, 2012.

[43] A. Palazzolo, R. Lin, R. Alexander, A. Kascak, and J. Montague, “Piezoelectric pushers for active vibration control of rotating machinery,” *ASME Journal of Vibration and Acoustics, Stress and Reliability*, vol. 111, no. 3, pp. 298–305, 1989.

[44] A. Palazzolo, R. Lin, R. Alexander, A. Kascak, and J. Montague, "Test and theory for piezoelectric actuator- active vibration control of rotating machinery," *ASME Journal of Vibration and Acoustics*, vol. 113, no. 2, pp. 167–175, 1991.

[45] M. Borsdorf, "Aktive Schwingungsminderung elastischer Flugtriebwerksrotoren mit Piezostapelaktoren unter Berücksichtigung der Dynamik des Triebwerkgehäuses," Ph.D. dissertation, Technische Universität Darmstadt, 2014.

[46] R. S. Schittenhelm, "Regelungstechnische Verfahren zur aktiven Minderung von Rotorschwingungen," Ph.D. dissertation, Technische Universität Darmstadt, 2015.

[47] F. Becker, "Active vibration isolation of a flexible rotor being subject to unbalance excitation and gyroscopic effect using H_∞ optimal control." in *Proceedings of the 9th IFToMM International Conference on Rotor Dynamics*, 2015.

[48] F. Becker, M. A. Sehr, and S. Rinderknecht, "Gain-scheduled h_∞-control for active vibration isolation of a gyroscopic rotor." in *ASME 2015 Conference on Smart Materials, Adaptive Structures and Intelligent Systems*, 2015.

[49] S. Heindel, F. B. Becker, and S. Rinderknecht, "Unbalance and resonance elimination with active bearings on a jeffcott rotor," *Mechanical Systems and Signal Processing*, vol. 85, pp. 339–353, 2016.

[50] E. Anderson and N. Hagood, "Simultaneous piezoelectric sensing/actuation: Analysis and application to controlled structures," *Journal of Sound and Vibration*, vol. 174, no. 5, pp. 617 – 639, 1994.

[51] D. G. Cole and R. L. Clark, "Adaptive compensation of piezoelectric sensoriactuators," *Journal of Intelligent Material Systems and Structures*, vol. 5, pp. 665–672, 1994.

[52] E. Grasso, N. Totaro, H. Janocha, and D. Naso, "Piezoelectric self sensing actuators for high voltage excitation," *Smart Materials and Structures*, vol. 22, no. 6, 2013.

[53] R. Köhler, "Phänomenologische Modellierung des temperaturabhängigen Verhaltens piezoelektrischer Stapelaktoren," Ph.D. dissertation, Technische Universität Darmstadt, 2013.

[54] H. Janocha, *Unkonventionelle Aktoren- Eine Einführung*. Oldenbourg Verlag, 2010.

[55] E. Grasso, "Self sensing techniques for piezoelectric vibration applications," Ph.D. dissertation, Universität Saarlandes, Saarbrücken, 2013.

[56] R. Deibert, "Methoden zur Fehlererkennung an Komponenten im geschlossenen Regelkreis," Ph.D. dissertation, Technische Universität Darmstadt, Düsseldorf, Januar 1997.

[57] R. Isermann, *Fault-Diagnosis Systems, An Introduction from Fault Detection to Fault Tolerance*. Springer, 2006.

[58] M. Steinberg, "Historical overview of research in reconfigurable flight control," *Proceedings of IMechE, Part G: Journal of Aerospace Engineering*, vol. 219, pp. 263–275, 2005.

[59] Y. Zhang and J. Jiang, "Bibliographical review on reconfigurable fault-tolerant control systems," *Annual Reviews in Control*, vol. 32, no. 2, pp. 229 – 252, 2008.

[60] Z. Wang and J. Fan, "Fault early recognition and health monitoring on aero-engine rotor system," *Journal of Aerospace Engineering*, vol. 28, no. 2, 2013.

[61] R. Gasch, R. Nordmann, and H. Pfützner, *Rotordynamik*. Springer, 2002.

[62] G. Genta, *Dynamics of Rotating Systems*, F. F. Ling, Ed. Springer, 2005.

[63] R. Isermann, *Identification of dynamic Systems, An Introduction with applications*. Springer, 2011.

[64] P. Li, N. Steinberg, K. Shatri, M. Thomas, and T. Gebler, "Experimentelle und numerische Untersuchung und Modellerweiterung eines aktiven Rotorlagers," Advanced Research Project, Technische Universität Darmstadt, March 2016.

[65] M. U. Thomas, "Modellerweiterung und Parametrierung an einem Rotorprüfstand," Bachelor Thesis, Technische Universität Darmstadt, 2014.

[66] T. Hoffmann, "Modellabgleich und Regelung zur Schwingungsisolation eines skalierten Triebwerksrotorprüfstandes," Master Thesis, Technische Universität Darmstadt, April 2015.

[67] R. Markert, *Schwingungsmesstechnik*. Technische Universität Darmstadt, 2005, Lecture Notes.

[68] K. Aainsqatsi. (2016, 10) Schematic diagram of a high-bypass turbofan engine. Own work. [Online]. Available: https://commons.wikimedia.org/w/index.php?curid=4005530

[69] Rolls Royce, *The Jet Engine*, 5th ed. Wiley & sons, 2015.

[70] X. Zhao, "Transmission of vibration caused by unbalance in an aircraft engine with active control strategies," Ph.D. dissertation, Technische Universität Darmstadt, 2016.

[71] X. Zhao and S. Rinderknecht, "Investigation of active damping strategies applied on the aircraft engine with comparison to the passively damped system," in *Proceedings of the 22nd International Symposium on Air Breathing Engines ISABE*, 2015.

[72] X. Zhao and S. Rinderknecht, "Investigation of actuator placement approaches for active vibration control in the aircraft engine," in *2015 IEEE Aerospace Conference*, 2015.

[73] H. Janocha, Ed., *Adaptronics and Smart structures: Basics, Materials, Design and Applications*, 2nd ed. Springer, 2007.

[74] *Piezo Nano Positioning, Inspirationen 2009*, Physik Instrumente (PI) GmbH & Co. KG, 2009, Product catalogue.

[75] S. R. Moheimani and A. J. Fleming, *Piezoelectric Transducers for Vibration Control and Damping*. Springer, 2006.

[76] R. Ambur, P. Zech, and S. Rinderknecht, "Vibration minimization on a rotor system with adaptive algorithms using self-sensing piezoelectric actuators," in *Vibrations in Rotating Machinery IMechE*, 2016.

[77] R. Isermann, "Modellbasierte Überwachung und Fehlerdiagnose von kontinuierlichen technischen Prozessen," *Automatisierungstechnik*, vol. 58, pp. 291–305, 2010.

[78] R. Ambur and S. Rinderknecht, "Self-sensing techniques of piezoelectric actuators in detecting unbalance faults in a rotating machine," *Procedia Engineering*, vol. 144, pp. 833 – 840, 2016.

[79] A. Sekhar, “Identification of unbalance and crack acting simultaneously in a rotor system: Modal expansion versus basis dynamic expansion,” *Journal of Vibration and Control*, vol. 11, no. 9, pp. 1125–1145, 2005.

[80] P. Pennacchi, A. Vania, and N. Bachschmid, “Fault identification in industrial rotating machinery: Theory and applications,” in *IUTAM Symposium on Emerging Trends in Rotor Dynamics*, ser. IUTAM Bookseries. Springer Netherlands, 2011, vol. 1011, pp. 455–467.

[81] P. Pennacchi, “Robust estimate of excitations in mechanical systems using M-estimators-theoretical background and numerical applications,” *Journal of Sound and Vibration*, vol. 310, no. 4-5, pp. 923 – 946, 2008.

[82] P. J. Huber and E. M. Ronchetti, *Robust statistics*, 2nd ed. Wiley, 2009.

[83] H. Chen and P. Meer, “Robust regression with projection based m-estimators,” in *Proceedings of the ninth IEEE International Conference on Computer Vision (ICCV-03)*, 2003, pp. 1–8.

[84] C. Goh and T. Caughey, “On the stability problem caused by finite actuator dynamics in the control of large space structures,” *International Journal of Control*, vol. 41, no. 3, pp. 787–802, 1985.

[85] S. M. Kuo and D. R. Morgan, “Active noise control: A tutorial review,” *Proceedings of the IEEE*, vol. 87, no. 6, pp. 943–973, 1999.

[86] M. Kauba and J. Millitzer, “Multi-channel narrowband Filtered-x-Least-Mean-Square algorithm with reduced calculation complexity,” in *5th ECCOMAS Thematic Conference on Smart Structures and Materials SMART’11*, 2011.

[87] Y. Kajikawa, W.-S. Gan, and S. M. Kuo, “Recent advances on active noise control: open issues and innovative applications,” *APSIPA Transactions on Signal and Information Processing*, vol. 1, 2012.

Appendices

A Positive Position Feedback (PPF) controller

For a self-sensing piezoelectric actuator, two controllers were recommended by [55] to attenuate the resonance peaks. One is a Positive Position Feedback (PPF) and the other is a Resonant controller (RC). The PPF controller behaves as a second-order lag element and it should be tuned separately for each resonance. Several PPF controllers can be operated in parallel to target different modes in the operating frequency range. A disadvantage of this method is the operation in multi-mode attenuation. The cross coupling effects between the gains tuned for each mode makes the tuning very difficult for the multi-mode case, which can be overcome by RC. In this thesis, this controller has been used to attenuate only the first resonance in the rotor operating range.

The PPF controller was proposed originally by Goh and Caughey [84]. A second order PPF controller consists of a second order filter as given in Eq. (A.1), where the damping factor is ξ_f and filter frequency is ω_f. The negative sign in the transfer function creates a positive feedback which gives the name to this type of controller. Its block diagram is depicted in Fig. A.1. Each filter is targeted at a specific mode, by adjusting ω_f to be approximately between $1.1-1.4$ times the resonance frequency to be attenuated. Hence it is necessary to know the locations of the resonance in the structure a-priori. The PPF controller can be regarded as unconditionally stable, except for very high gains g which is not used in practice [2]. The gains g can be chosen by trial-and-error in the test bench.

$$G_{ppf}(s) = \frac{-g}{s^2 + 2\xi_f \omega_f s + \omega_f^2} \tag{A.1}$$

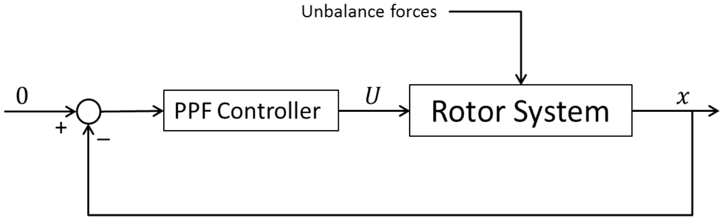

Figure A.1: Block diagram of rotorsystem with PPF

B Introduction to FxLMS algorithm

The Filtered x-Least mean squares (FxLMS) is an adaptive feedforward control algorithm, for a single frequency anti-noise system [85]. The algorithm has been developed and implemented for a multi-input-multi-output (MIMO) system, used commonly in active vibration control. Figure B.1 describes the block diagram of the algorithm. It shows a single-input-single-output (SISO) implementation for m actuators and n sensors. The basic principle of the algorithm is to compute a signal $y(k)$ which cancels out the disturbance ($d(k)$) acting on the system. This means that the signals $y(k)$ and $d(k)$ have the same amplitude but differ by 180° in phase.

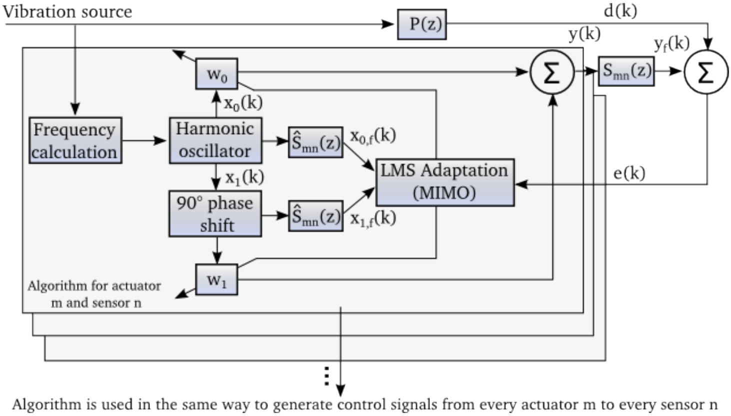

Figure B.1: Block diagram of a FxLMS algorithm [76]

A reference signal as an input is needed to calculate the frequency f of the operating point. Two orthogonal sinusoidal signals ($x_0(k)$, $x_1(k)$) are computed for this frequency as given in Eq. (B.1) and (B.2) in discrete time domain. In these equations t_s is the sampling time and k the samples.

$$x_0(k) = \sin(2\pi.f.k.t_s) \tag{B.1}$$

$$x_1(k) = \sin(2\pi.f.k.t_s + \frac{\pi}{2}) \tag{B.2}$$

The output of the algorithm $y(k)$ is given by the weighted sum of these two signals (Eq. (B.3)). The output of the algorithm which is given to one actuator is the sum of all outputs to that actuator from all sensors.

$$y(k) = w_0(k)x_0(k) + w_1(k)x_1(k) \tag{B.3}$$

The main section of the algorithm deals with the computation of the weights $w_0(k)$ and $w_1(k)$ at each sample. The weights are calculated recursively in each sample as given by Eq. (B.5) and (B.6) considering the error signal $e(k)$.

$$e(k) = y_f(k) + d(k) \tag{B.4}$$

$$w_0(k+1) = (1-\gamma)w_0(k) + \mu x_{0,f}(k)e(k) \tag{B.5}$$

$$w_1(k+1) = (1-\gamma)w_1(k) + \mu x_{1,f}(k)e(k) \tag{B.6}$$

The main tuning parameters of the algorithm are γ and μ. They are the forgetting factor and step size of algorithm respectively. With the help of these parameters the convergence speed and the residual error of the algorithm are influenced. These factors can be experimentally determined.

It should be noted that a transfer function $\hat{S}_{mn}$ transforms the signal x_0 to $x_{0,f}$. This is called as a secondary path model, which is the transfer function between the m^{th} actuator and n^{th} sensor. It is part of the model of the real system on which the active vibration control should be implemented. This secondary path model can be either derived analytically or with identification techniques. In the present work, they have been identified with sine sweep signals.

This basic principle of the algorithm is computationally intensive and hence in this thesis, an alternative filtering technique according to [86] is implemented. A frequency dependent look-up table is created with complex values of the secondary path model, in which the phase and amplitudes are stored. The filtered signal $y_f(k)$ is calculated by complex multiplication with these stored values. Novel research in the field of adaptive algorithms are those which does not consider secondary path model at all as suggested by [87].

C Simulation results from WEM unbalance detection

Case 1: Active bearing - Piezo and SFD in series

Table C.1: Detected unbalances from WEM (Active bearing - Piezo and SFD in series) - without any outlier

Unbalance Location Stage Nr.	Detected unbalance Magnitude (gmm)	Phase (deg)	Error Magnitude(rel) (%)	Phase(abs) (deg)
1	979.7	-0.6	-2.09	-0.6
2	969.9	0.03	-3.09	0
3	972.1	0.06	-2.69	0
4	969.6	-0.62	-3.04	-0.6
5	973.8	-0.22	-2.62	-0.2
6	973.4	-0.6	-2.66	-0.6
7	983.1	-0.46	-1.69	-0.4
8	974.9	0.26	-2.51	0.2
9	978.9	0.08	-2.11	0
10	971.9	-0.5	-2.81	-0.5

Table C.2: Detected unbalances from WEM (Active bearing - Piezo and SFD in series) - with outliers

Unbalance Location Stage Nr.	Detected unbalance Magnitude (gmm)	Phase (deg)	Error Magnitude(rel) (%)	Phase(abs) (deg)
1	766.9	8.5	-23.3	8.5
2	764.2	8.6	-25.8	8.6
3	748.0	9.0	-25.2	9.0
4	737.9	9.1	-26.2	9.1
5	730.3	9.5	-27	9.5
6	722.5	9.8	-27.8	9.8
7	724.1	9.8	-27.6	9.8
8	716.4	10.3	-28.4	10.3
9	704.7	10.8	-29.6	10.8
10	690.8	11.5	-31	11.5

Table C.3: Detected unbalances from WEM (Active bearing - Piezo and SFD in series) - with robust estimators

Unbalance Location Stage Nr.	Detected unbalance Magnitude (gmm)	Phase (deg)	Error Magnitude(rel) (%)	Phase(abs) (deg)
1	901.4	3.6	9.9	3.6
2	947.5	1.7	5.3	1.7
3	970.2	0.18	3.0	0.2
4	964.6	0.12	3.6	0.1
5	966.9	0.02	3.4	0
6	971.8	-0.08	2.9	0
7	973.1	-0.07	2.7	0
8	974.4	0.0	2.6	0
9	971.4	0.0	2.9	0
10	969.7	0.0	3.1	0

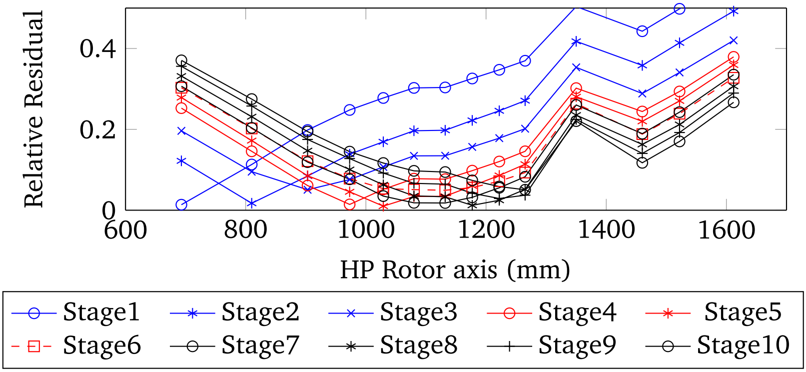

(a) without any outlier

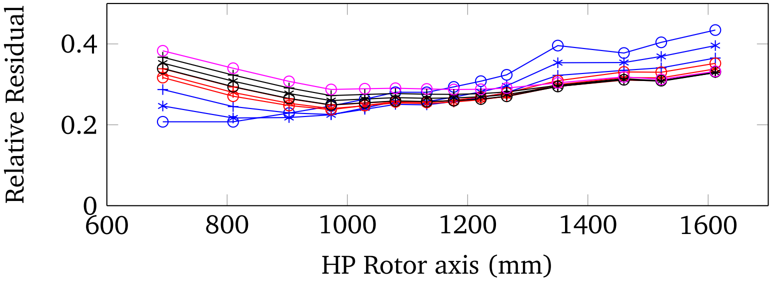

(b) with outliers

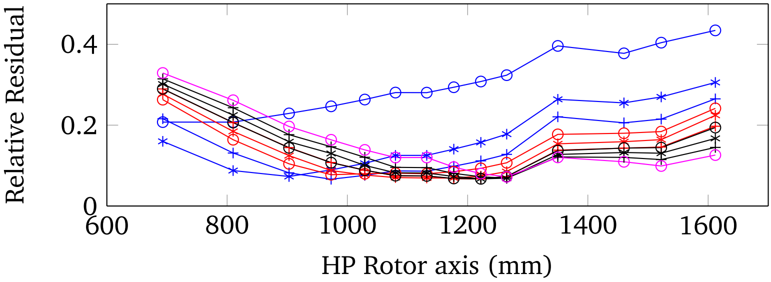

(c) with robust estimators

Figure C.1: Relative residual of unbalance detection at all stages - Active bearing (Piezo,SFD series)

Case 2: Active bearing- Piezo and SFD in parallel

Table C.4: Detected unbalances from WEM (Active bearing - Piezo and SFD in parallel) - without any outlier

Unbalance Location Stage Nr.	Detected unbalance Magnitude (gmm)	Phase (deg)	Error Magnitude(rel) (%)	Phase(abs) (deg)
1	970.7	99.9	-2.9	-0.1
2	966.6	100.1	-3.3	0.1
3	984.3	100.3	-1.6	0.3
4	977.7	99.18	-2.3	-0.8
5	981.7	99.5	-1.9	-0.5
6	974.6	99.8	-2.6	-0.2
7	972	99.1	-2.8	-0.9
8	979.9	100.6	-2.1	0.6
9	980	99.8	-2.0	-0.2
10	975.5	99.8	-2.5	-0.2

Table C.5: Detected unbalances from WEM (Active bearing - Piezo and SFD in parallel) - with outliers

Unbalance Location Stage Nr.	Detected unbalance Magnitude (gmm)	Phase (deg)	Error Magnitude(rel) (%)	Phase(abs) (deg)
1	616.3	116.6	-38.4	16.6
2	603.6	117.1	-39.7	17.1
3	580.9	119.7	-42	19.7
4	567.5	119.9	-43.3	19.9
5	563.9	122.0	-43.7	22.0
6	556.6	122.4	-43.4	22.4
7	555.7	123.0	-44.5	23.0
8	558.5	122.4	-44.2	22.4
9	534.9	125.3	-46.6	25.3
10	512.5	125.7	-48.8	25.7

Table C.6: Detected unbalances from WEM (Active bearing - Piezo and SFD in parallel) - with robust estimators

Unbalance Location	Detected unbalance		Error	
Stage Nr.	Magnitude (gmm)	Phase (deg)	Magnitude(rel) (%)	Phase(abs) (deg)
1	918.3	102.6	-8.2	2.6
2	942.6	101.5	-5.8	1.5
3	958.9	100.6	-4.2	0.6
4	967.5	99.7	-3.3	-0.3
5	958.9	101.4	-4.2	1.4
6	975.6	100.5	-2.5	0.5
7	968.7	101.9	-3.2	1.9
8	997.5	100.2	-0.3	0.2
9	949.9	101.8	-5.1	1.8
10	967.5	100.6	-3.3	0.6

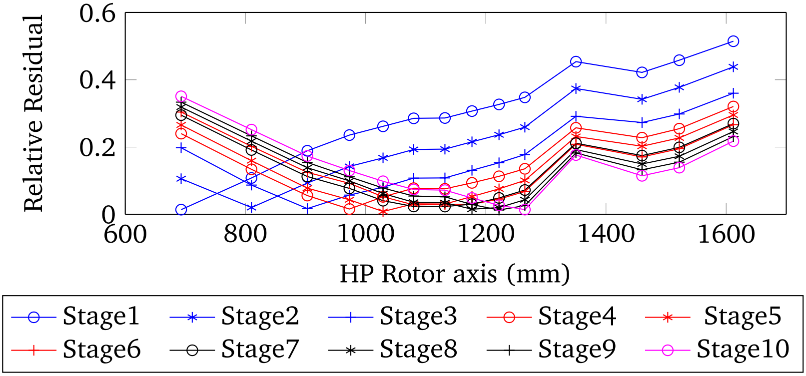

(a) without any outlier

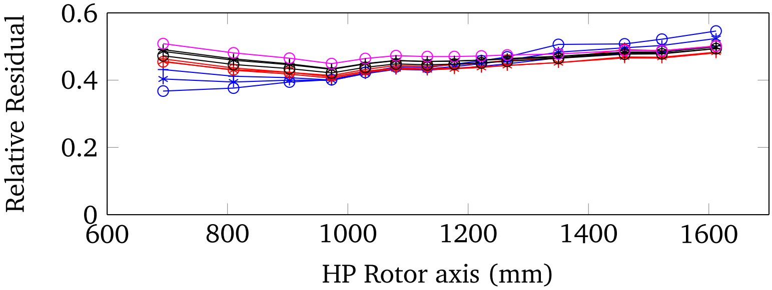

(b) with outliers

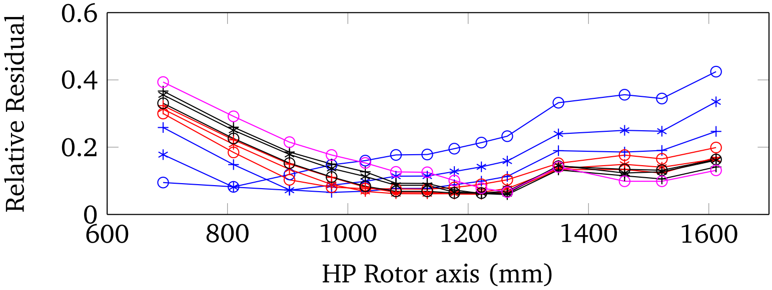

(c) with robust estimators

Figure C.2: Relative residual of unbalance detection at all stages - Active bearing (Piezo,SFD parallel)

Table C.7: Detected unbalances from WEM (Active internal suspension) - without any outlier

Unbalance Location Stage Nr.	Detected unbalance Magnitude (gmm)	Phase (deg)	Error Magnitude(rel) (%)	Phase(abs) (deg)
1	977.8	120	-2.3	0
2	978.0	119.9	-2.2	-0.1
3	977.8	120	-2.3	0
4	977.7	119.9	-2.3	-0.1
5	977.9	119.9	-2.3	-0.1
6	977.8	120	-2.3	0
7	978.0	120	-2.2	0
8	978.0	120	-2.2	0
9	978.0	119.9	-2.2	-0.1
10	978.5	119.9	-2.2	-0.1

Table C.8: Detected unbalances from WEM (Active internal suspension) - with outliers

Unbalance Location Stage Nr.	Detected unbalance Magnitude (gmm)	Phase (deg)	Error Magnitude(rel) (%)	Phase(abs) (deg)
1	464.1	159.4	-53.6	39.4
2	468.3	158.9	-53.2	38.9
3	469.7	158.8	-53.1	38.8
4	469.7	158.1	-53.1	38.1
5	469.4	158.5	-53.1	38.5
6	468.5	159.8	-53.2	39.8
7	468.4	159.8	-53.2	39.8
8	464.9	160.3	-53.6	40.3
9	459.9	161.6	-54.1	41.6
10	453.1	163.9	-54.7	43.9

Table C.9: Detected unbalances from WEM (Active internal suspension) - with robust estimators

Unbalance Location Stage Nr.	Detected unbalance Magnitude (gmm)	Phase (deg)	Error Magnitude(rel) (%)	Phase(abs) (deg)
1	736.2	141.6	-26.4	21.6
2	736.3	141.5	-26.4	21.5
3	737.3	141.3	-26.3	21.3
4	738.7	141.2	-26.1	21.2
5	738.5	141.2	-26.1	21.2
6	738.5	141.0	-26.1	21.0
7	738.1	141.1	-26.1	21.1
8	738.8	140.9	-26.1	20.9
9	739.3	140.7	-26.1	20.7
10	740.9	140.5	-25.9	20.5

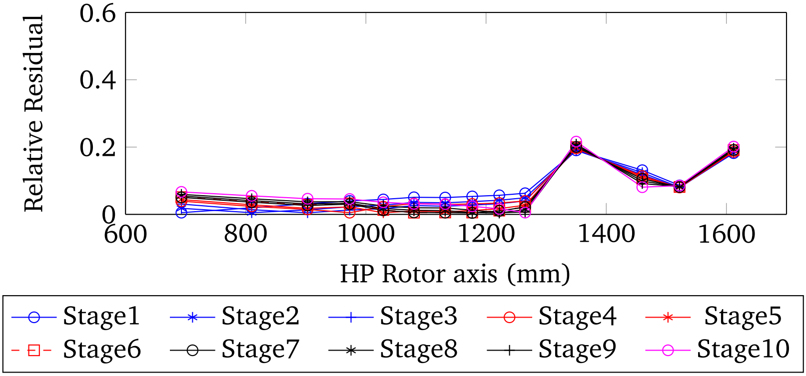

(a) without any outlier

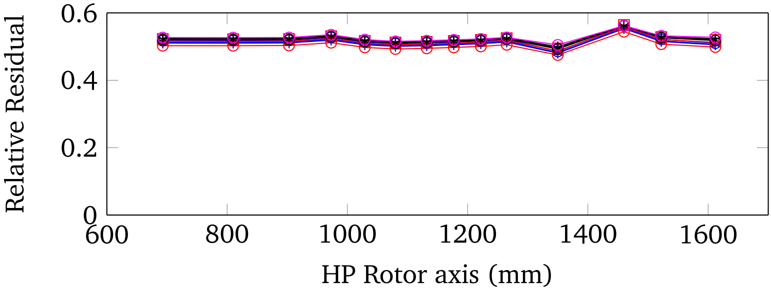

(b) with outliers

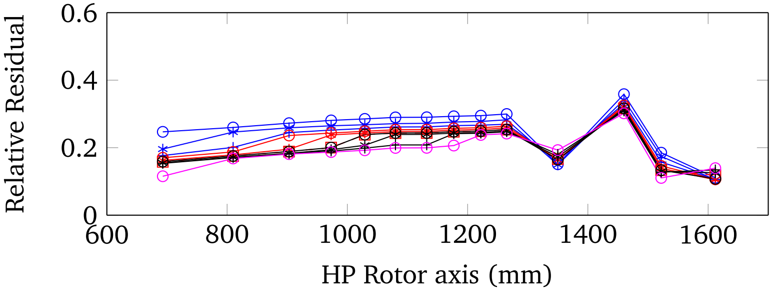

(c) with robust estimators

Figure C.3: Relative residual of unbalance detection at all stages - Active internal suspension

Curriculum Vitae

Personal	Ramakrishnan Ambur Sankaranarayanan born on 16. July 1987 in Tirunelveli, India.
Studies	
1991 - 2004	School education A.V.Rm.V Matriculation Higher Secondary School, Ambasamudram, India.
2004 - 2008	B.E.(Hons.) Mechanical Engineering Birla Institute of Technology and Science, Pilani Goa campus, India.
2009 - 2012	M.Sc. Automotive Engineering RWTH Aachen University, Germany.
2013 - 2016	PhD at Institute for Mechatronic Systems in Mechanical Engineering, Technische Universität Darmstadt, Germany.
Job	
2008 - 2009	Trainee Engineer Mercedes-Benz Research and Development India, Bengaluru, India.